

HU ISSN 1586–2070

# JOURNAL OF COMPUTATIONAL AND APPLIED MECHANICS

An Open Access International Journal

Published by the University of Miskolc

VOLUME 14, NUMBER 1-2 (2019)



MISKOLC UNIVERSITY PRESS



HU ISSN 1586–2070

# **JOURNAL OF COMPUTATIONAL AND APPLIED MECHANICS**

An Open Access International Journal

Published by the University of Miskolc

VOLUME 14 NUMBER 1-2 (2019)



**MISKOLC UNIVERSITY PRESS**



## EDITORS

**László BARANYI**, Institute of Energy Engineering and Chemical Machinery, University of Miskolc, H-3515 MISKOLC, Hungary, e-mail: [arambl@uni-miskolc.hu](mailto:arambl@uni-miskolc.hu)

**István PÁCZELT**, Institute of Applied Mechanics, University of Miskolc, H-3515 MISKOLC, Hungary e-mail: [mechpacz@uni-miskolc.hu](mailto:mechpacz@uni-miskolc.hu)

**György SZEIDL**, Institute of Applied Mechanics, University of Miskolc, H-3515 MISKOLC, Hungary e-mail: [Gyorgy.SZEIDL@uni-miskolc.hu](mailto:Gyorgy.SZEIDL@uni-miskolc.hu)

## EDITORIAL BOARD

Edgár BERTÓTI, Institute of Applied Mechanics, University of Miskolc, H-3515 MISKOLC, Hungary, e-mail: [edgar.bertoti@uni-miskolc.hu](mailto:edgar.bertoti@uni-miskolc.hu)

Attila BAKSA, Institute of Applied Mechanics, University of Miskolc, H-3515 MISKOLC, Hungary, [attila.baksa@uni-miskolc.hu](mailto:attila.baksa@uni-miskolc.hu)

István ECSEDI, Institute of Applied Mechanics, University of Miskolc, H-3515 MISKOLC, Hungary, [mechecs@uni-miskolc.hu](mailto:mechecs@uni-miskolc.hu)

Ulrich GABBERT, Institut für Mechanik, Otto-von-Guericke-Universität Magdeburg, Universitätsplatz 2, 39106 MAGDEBURG, Germany, [ulrich.gabbert@mb.uni-magdeburg.de](mailto:ulrich.gabbert@mb.uni-magdeburg.de)

Zsolt GÁSPÁR, Department of Structural Mechanics, Budapest University of Technology and Economics, Műegyetem rkp. 3, 1111 BUDAPEST, Hungary, [gaspar@ep-mech.me.bme.hu](mailto:gaspar@ep-mech.me.bme.hu)

Robert HABER, Department of Theoretical and Applied Mechanics, University of Illinois at Urbana-Champaign, 216 Talbot Lab., 104 S. Wright St., URBANA, IL 61801, USA, [r-haber@uiuc.edu](mailto:r-haber@uiuc.edu)

Csaba HŐS, Department of Hydraulic Machines, Budapest University of Technology and Economics, Műegyetem rkp. 3, 1111 BUDAPEST, Hungary, [hoscsaba@vizgep.bme.hu](mailto:hoscsaba@vizgep.bme.hu)

Károly JÁRMAI, Institute of Energy Engineering and Chemical Industry, University of Miskolc, H-3515 MISKOLC, Hungary, [altjar@uni-miskolc.hu](mailto:altjar@uni-miskolc.hu)

László KOLLÁR, Department of Structural Engineering, Budapest University of Technology and Economics, Műegyetem rkp. 3. K.II.42., 1521 BUDAPEST, Hungary, [lkollar@eik.bme.hu](mailto:lkollar@eik.bme.hu)

József KÖVECSES, Mechanical Engineering Department 817 Sherbrooke Street West, MD163 MONTREAL, Quebec H3A 2K6 [jozsef.kovecses@mcgill.ca](mailto:jozsef.kovecses@mcgill.ca)

Márta KURUTZ, Department of Structural Mechanics, Budapest University of Technology and Economics, Műegyetem rkp. 3, 1111 BUDAPEST, Hungary, [kurutzm@eik.bme.hu](mailto:kurutzm@eik.bme.hu)

Lin LU, Center for Deepwater Engineering, Dalian University of Technology, Dalian, China [lulin@dlut.edu.cn](mailto:lulin@dlut.edu.cn)

Herbert MANG, Institute for Strength of Materials, University of Technology, Karlsplatz 13, 1040 VIENNA, Austria, [Herbert.Mang@tuwien.ac.at](mailto:Herbert.Mang@tuwien.ac.at)

Sanjay MITTAL, Department of Aerospace Engineering, Indian Institute of Technology, KANPUR, UP 208 016, India, [smittal@iitk.ac.in](mailto:smittal@iitk.ac.in)

Zenon MRÓZ, Polish Academy of Sciences, Institute of Fundamental Technological Research, Swietokrzyska 21, WARSAW, Poland [zmroz@ippt.gov.pl](mailto:zmroz@ippt.gov.pl)

Gyula PATKÓ, Institute of Machine Tools and Mechatronics, University of Miskolc, H-3515 MISKOLC, Hungary, [patko@uni-miskolc.hu](mailto:patko@uni-miskolc.hu)

Jan SLADEK, Ústav stavbenictva a architektúry, Slovenskej akadémie vied, Dubróvska cesta 9, 842 20 BRATISLAVA, Slovakia, [usarslad@savba.sk](mailto:usarslad@savba.sk)

Gábor STÉPÁN, Department of Applied Mechanics, Budapest University of Technology and Economics, Műegyetem rkp. 3, 1111 BUDAPEST, Hungary, [stepan@mm.bme.hu](mailto:stepan@mm.bme.hu)

Barna SZABÓ, Department of Mechanical Engineering and Materials Science, Washington University, Campus Box 1185, ST. LOUIS, MO 63130, USA, [szabo@wustl.edu](mailto:szabo@wustl.edu)

Balázs TÓTH, Institute of Applied Mechanics, University of Miskolc, 3515 MISKOLC, Hungary, [balazs.toth@uni-miskolc.hu](mailto:balazs.toth@uni-miskolc.hu)

## HONORARY EDITORIAL BOARD MEMBERS

Tibor CZIBERE, Department of Fluid and Heat Engineering, University of Miskolc, H-3515 Miskolc-Egyetemváros, Hungary

R. Ivan LEWIS, Room 2-16 Bruce Building, Newcastle University, NEWCASTLE UPON TYNE, NE1 7RU, UK

Gábor HALÁSZ, Department of Hydraulic Machines, Budapest University of Technology and Economics, Műegyetem rkp. 3, 1111 BUDAPEST, Hungary,



## ANALYTICAL INVESTIGATIONS OF TEMPERATURE EFFECTS ON CREEP STRAIN RELAXATION OF BIOMATERIALS USING HOMOTOPY PERTURBATION AND DIFFERENTIAL TRANSFORM METHODS

OLUROTIMI ADELEYE, OLAKANLA ABDULKAREEM

Department of Systems Engineering, University of Lagos  
Akoka, Lagos, Nigeria

[rotimiadeleye1711@gmail.com](mailto:rotimiadeleye1711@gmail.com), [olaks1@live.com](mailto:olaks1@live.com)

AHMED YINUSA AND GBEMINIYI SOBAMOWO

Department of Mechanical Engineering, University of Lagos,  
Akoka, Lagos, Nigeria

[mynotebook2010@yahoo.com](mailto:mynotebook2010@yahoo.com), [mikegbeminiyi@gmail.com](mailto:mikegbeminiyi@gmail.com)

[Received: February 14, 2019; Accepted: August 22, 2019]

**Abstract.** In this paper, the effect of temperature on relaxation of creep strain in biomaterials is modeled and analyzed with homotopy perturbation and differential transform methods. Polymeric biomaterials used as implants undergo both geometric and material nonlinear deformation when subjected to different loading conditions. The present study is concerned with the effects of temperature on the geometric nonlinear deformation of the relaxation of creep strain in these materials. Polymeric biomaterials exhibit time dependent response as observed in viscoelastic materials and this is represented by a one-dimensional rheological material model with constant material parameters. This model is then extended to capture the effects of temperature and the resulting final governing model is a nonlinear differential equation which cannot be easily solved by the standard analytic techniques. Here, two efficient special nonlinear analytic techniques, the homotopy perturbation and differential transform methods, are applied to obtain the solution of the developed nonlinear differential equation. The obtained analytical solutions are validated with the fourth-order Runge-Kutta numerical method. An error analysis shows that good agreement exists between the solutions obtained with these methods. The effects of some parameters on the model were investigated. As observed from the study, it can be shown that an increase in thermal conductivity and viscosity resulted in an increase in resistance to deformation of the material, while an increase in the material stiffness resulted in an increase in the rate of deformation and relaxation.

*Mathematical Subject Classification:* 80A20, 80M25

*Keywords:* Creep, relaxation, temperature, alginate hydrogel biomaterials, homotopy perturbation method, differential transform method

### 1. INTRODUCTION

Polymers have a wide range of applications such as: automobile, aviation, electronics, and packaging industries. But in the past few decades, polymers have been extended

to biomedical applications. The polymers used for biomedical applications as a result of their biocompatibility, controllable biodegradation rate and their biofunctional properties, include natural polymers, which are polysaccharides (i.e. starch, glyco-gen) and synthetic polymers, which are: poly(glycolic acid) (PGA) and poly(hydroxyl butyrate) (PHB) [1]. Several devices and implants have been studied and observed throughout the medical field, and they have been developed for various applications in the human body (Figure 1). These ranges from artificial support, such as synthetic blood vessel, hip replacement and knee/joint implants, to applications that alleviate the human organ functions, e.g. pacemaker. These applications also tend to vary according to their positions and placement within the body. The areas of application of these devices include regions with high chemical, electrical and mechanical activity, such as when they are used in regions of high mechanical stress for the replacement of bone. Biomaterials tend to undergo deformation over time especially when temperature around the material increases beyond the normal temperature, hence there is a need to investigate the effects of this increase in temperature on relaxation of creep strain in order to avoid failure of these materials before replacement.

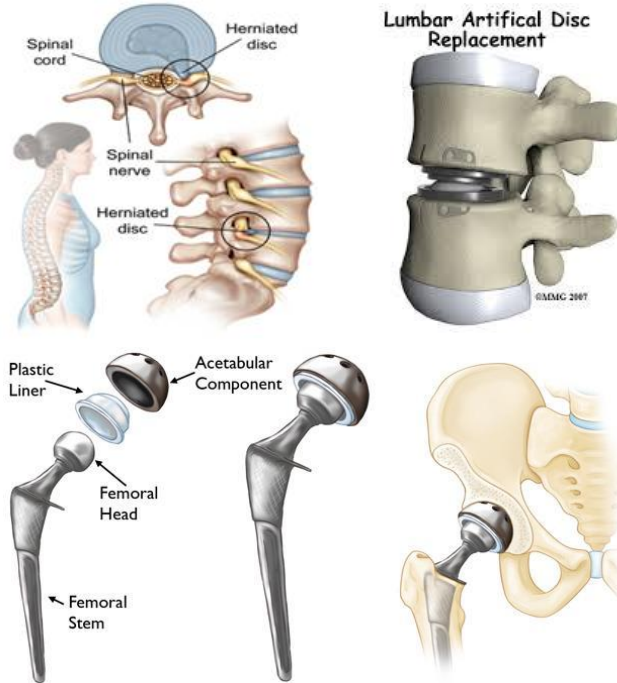


Figure 1. Biomedical applications: Lumbar artificial disc replacement, Hip liner replacement

Nonlinear behaviors have been observed in the deformation of the biomaterials as shown in the stress-strain curve of an alginate hydrogels [2] which are extremely dependent on the strain rate. This is also noticed in tensile tests of ligaments and tendons [3, 4]. Notable successes have been obtained in the use of nonlinear models



for the behavior of biomaterials [5, 6]. It has also been observed that most polymeric biomaterials exhibit viscous tendencies and these behaviors are nonlinear in nature [5]. There are different requirements for the device and implant which are important for the continued existence of the implants and the comfort of the user, which are chemical, electrical, thermal and mechanical characteristics of the substrate for implants and packaging for devices [7]. Stress relaxation tests have often been used as a convenient technique for determining the rheological behaviors of several viscoelastic materials. As a result of differences in material characteristics, several linear and nonlinear viscoelastic models exist which represent the relationship between the time and the stress modulus [8–10].

In the present study, a nonlinear viscoelastic model has been developed by using the stress decomposition theory to analyze the effects of temperature in the relaxation of creep strain in biomaterials. The model is represented by a nonlinear differential equation whose solutions cannot be easily obtained with the standard analytical techniques. There are special analytical techniques for solving nonlinear differential equations. Two among them have been used to obtain the solution of the developed nonlinear differential equation; the homotopy perturbation and the differential transform methods. The homotopy perturbation method (HPM) was first proposed by Ji-Huan He [11] for solving integral and differential equations for both linear and nonlinear models. It is a powerful analytical method which does not require any approximation. A number of studies have been carried out to establish the strength of HPM by comparing the results obtained to other methods such as Adomian Decomposition Method (ADM)[12]. Remarkably, these studies have concluded that the method is more accurate and effective than ADM. Other studies carried out with the homotopy perturbation method (HPM) include its use for the analysis of heat transfer in longitudinal fins [13], the use of HPM and collocation method (CM) for analysis of thermal performances of porous fin with temperature-dependent heat generation [14] and heat transfer analysis of non-Newtonian natural convective fluid flow using homotopy perturbation and Daftardar-Gejiji and Jafari methods [15].

Another efficient method for determining exact solution in nonlinear phenomena is the differential transform method (DTM). The differential transform method is an approximate analytical method for solving linear and nonlinear differential equations. The differential transformation method (DTM) was developed by Zhou in 1986 [16, 17]. It is also used in providing solutions to both linear and nonlinear partial differential equations [18]. It has a lower computational intensity than other approximate methods and the accuracy is higher than those methods [19, 20]. The distinguishing features of DTM have been emphasized in quite a number of studies [21]. Comparisons have been made between the results of DTM and results obtained with other methods such as adomian decomposition method (ADM) [22] and finite element method (FEM) [19]. In order to achieve better results, the efficiency of DTM has been combined with other methods [20]. These methods include the Laplace transform, which was used to overcome the deficiency that emanated from unsatisfied conditions [23]. DTM was used to solve the problems of phagocyte transmigration for foreign body

responses to subcutaneous biomaterial implantations [24] and creep strain relaxations in biomaterials [25].

Hence, the aim of this study is to investigate the problem of temperature effects on relaxation of creep strain in polymeric biomaterials. This problem, which is governed by a developed nonlinear differential equation, is solved using two efficient methods; the homotopy perturbation method and differential transform method. The fourth-order Runge-Kutta numerical method is then applied to validate the obtained solution from the two methods. The effects of thermal conductivity, viscosity and material stiffness on the deformation of these biomaterials are then considered.

## 2. PROBLEM DESCRIPTION

A nonlinear material model has been adopted due to the viscous nature of the polymeric biomaterials. This non-linear material has elastic, inertial nonlinearities and viscous parameters as presented by Monsia [5]. A logarithm spring force law is used in this model which describes the unloading response of a viscoelastic material perfectly when subjected to constant loading.

$$\varphi(\varepsilon) = \ln \left( \varepsilon_0 - \frac{\varepsilon(t)}{\varepsilon_0} \right) \quad (1)$$

$\varepsilon_0 \neq 0$  is a material constant. As expressed by Monsia [5] the function exists if and only if  $\varepsilon_0 > \sqrt{\varepsilon(t)}$ . The function  $\varphi(\varepsilon)$  has a vertical asymptote at  $\varepsilon(t) = \varepsilon_0^2$ , which implies  $\varphi(\varepsilon)$  is not defined for  $\varepsilon > \varepsilon_0^2$ . Therefore the nonlinear ordinary differential equation from Bauer's theory [26], by superposing inertial stresses, pure elastic, and viscosity, for a nonlinear spring force function  $\varphi(\varepsilon)$  can be rewritten in the form

$$\frac{a\varphi(\varepsilon)}{c} + \frac{b\dot{\varepsilon}\varphi'(\varepsilon)}{c} + \dot{\varepsilon}^2\varphi''(\varepsilon) + \ddot{\varepsilon}\varphi'(\varepsilon) = \frac{\sigma_t}{c} \quad (2)$$

$$\varepsilon(0) = \varepsilon_i \quad \dot{\varepsilon}(0) = 0$$

where  $a$  and  $b$  are the viscosity and stiffness time independent coefficients respectively,  $c$  is the time independent inertia module,  $\varepsilon(t)$  denotes the time dependent strain,  $\varepsilon_i$  is the initial strain, and  $\sigma_t$  denotes the total exciting stress acting on the material. The relationship between the deformation temperature parameter, the flow stress (i.e. exciting stress) and strain rate can be represented by hyperbolic sine Arrhenius type equation [27].

$$|\dot{\varepsilon}| = AF(|\sigma|) \exp[-Q/RT] \quad (3)$$

where  $F(\sigma)$  is a parameter function of stress,  $A$  is a material constant,  $\dot{\varepsilon}$  is the strain rate,  $Q$  is the activation energy,  $R$  is the universal gas constant, and  $T$  is the absolute temperature. The effects of the temperature and strain rate on the deformation can be denoted by the Zener-Hollomon parameter  $Z$  [28]:

$$Z = |\dot{\varepsilon}| \exp[-Q/RT] \quad (4)$$

Using equation (4), and substituting the exponential law into equation (3), the strain rate is obtained as

$$|\dot{\varepsilon}| = A|\sigma|^n \exp[-Q/RT] \quad (5)$$

where  $n$  is a material constant.

### 3. SOLUTION FOR TEMPERATURE EFFECTS ON STRAIN-RATE

Utilizing equation (1) and (5) equation (2) can be rewritten as

$$\frac{a \ln(\varepsilon_0 - \varepsilon/\varepsilon_0)}{b} - \frac{b\dot{\varepsilon}}{c\varepsilon_0(\varepsilon_0 - \varepsilon/\varepsilon_0)} - \frac{\ddot{\varepsilon}}{\varepsilon_0(\varepsilon_0 - \varepsilon/\varepsilon_0)} - \frac{\dot{\varepsilon}^2}{\varepsilon_0^2(\varepsilon_0 - \varepsilon/\varepsilon_0)} = \frac{\dot{\varepsilon}}{Ac} \exp[Q/RT]. \quad (6)$$

The exponential function  $\exp Q/RT$  in equation (5) can be expanded as

$$e^{Q/RT} \simeq 1 + \frac{Q}{RT} + \frac{(Q/RT)^2}{2!} \dots \quad (7)$$

Substituting equation (7) into (6) the evolution equation of deformation becomes

$$\frac{c(\varepsilon_0^2 - \varepsilon)\ddot{\varepsilon} + b(\varepsilon_0^2 - \varepsilon)\dot{\varepsilon} + c\dot{\varepsilon}^2}{c(\varepsilon_0^2 - \varepsilon)^2} - \frac{\dot{\varepsilon}}{Ac} - \frac{\dot{\varepsilon}Q}{AcRT} - \frac{a \ln(\varepsilon_0 - \varepsilon/\varepsilon_0)}{c} = 0 \quad (8)$$

$\varepsilon(0) = \varepsilon_i \quad \dot{\varepsilon}(0) = 0$

Equation (8) is the nonlinear evolution equation of deformation for material under the effects of temperature.

### 4. DETERMINING THE TIME-DEFORMATION EQUATION

In order to resolve (8), a change of variables is considered. By utilizing the transformation

$$\varepsilon_0 e^x = \varepsilon_0^2 - \varepsilon, \quad x = \ln \left( \frac{\varepsilon_0^2 - \varepsilon}{\varepsilon_0} \right) \quad (9)$$

for  $\dot{\varepsilon}$  and  $\ddot{\varepsilon}$  we have  $\dot{\varepsilon} = -\dot{x}\varepsilon_0 e^x$  and  $\ddot{\varepsilon} = -\ddot{x}\varepsilon_0 e^x - \dot{x}^2 \varepsilon_0 e^x$ . After substituting them into (8) the nonlinear evolution equation of deformation has the form

$$\frac{e^{-2x}(b\varepsilon_0 e^x(-\dot{x}\varepsilon_0 e^x) + c(-\dot{x}\varepsilon_0 e^x)^2 + c\varepsilon_0 e^x(-\ddot{x}\varepsilon_0 e^x - \dot{x}^2 \varepsilon_0 e^x))}{c(\varepsilon_0^2 - \varepsilon)^2} - \frac{ax}{c} + \frac{\dot{x}\varepsilon_0 e^x}{Ac} + \frac{\dot{x}\varepsilon_0 e^x Q}{AcRT} = 0 \quad (10)$$

which can be simplified further to

$$\frac{-b\dot{x}}{c} + \dot{x}^2 - \ddot{x} - \dot{x}^2 - \frac{ax}{c} + \frac{\dot{x}\varepsilon_0 e^x}{Ac} \left(1 + \frac{Q}{RT}\right) = 0. \quad (11)$$

Introducing the notations  $b/c = \alpha$ ,  $a/c = \beta$  and  $1/(Ac) = \gamma$  equation (11) becomes

$$\ddot{x} + \alpha\dot{x} + \beta x - \gamma\dot{x}\varepsilon_0 e^x \left(1 + \frac{Q}{RT}\right) = 0. \quad (12)$$

Here  $\alpha$  is the viscosity coefficient,  $\beta$  is the stiffness coefficient and  $\gamma$  is the thermal coefficients, respectively.

Substituting the first four terms of the series  $e^x \simeq 1 + x + \frac{x^2}{2!} + \frac{x^3}{3!} + \dots$  into (12) yields

$$\ddot{x} + \alpha\dot{x} + \beta x - \gamma\dot{x}\varepsilon_0 \left(1 + x + \frac{x^2}{3} + \frac{x^3}{6}\right) \left(1 + \frac{Q}{RT}\right) = 0. \quad (13)$$

Equation (13) can also be expanded and expressed as

$$\ddot{x} + \alpha\dot{x} + \beta x - \gamma\dot{x}\varepsilon_0 - \frac{Q\gamma\dot{x}\varepsilon_0}{RT} - x\gamma\dot{x}\varepsilon_0 - \frac{Qx\gamma\dot{x}\varepsilon_0}{RT} - \frac{1}{3}x^2\gamma\dot{x}\varepsilon_0 - \frac{Qx^2\gamma\dot{x}\varepsilon_0}{3RT} - \frac{1}{6}x^3\gamma\dot{x}\varepsilon_0 - \frac{Qx^3\gamma\dot{x}\varepsilon_0}{6RT} = 0. \quad (14)$$

## 5. METHOD OF SOLUTION 1

**5.1. Homotopy perturbation method.** Equation (13) is a nonlinear differential equation which can be solved using HPM. To apply HPM consider the equation

$$L(u) + N(u) = f(r) \quad r \in \Omega \quad (15)$$

associated with the boundary conditions

$$B\left(u, \frac{\partial u}{\partial n}\right) = 0, \quad r \in \Gamma. \quad (16)$$

Here  $u(r)$  is the unknown,  $L(u)$  and  $N(u)$  are linear and nonlinear operators respectively,  $f(r)$  is a known analytical function.  $\Gamma$  is the boundary of the domain  $\Omega$  with outward normal  $n$ .

The homotopy perturbation method proposed by Ji-Huan-He [11] can be expressed as

$$H(u, p) = (1 - p)[L(u) - L(u_0)] + p[L(u) + N(u) - f(r)] = 0 \quad (17)$$

where  $p$  is an embedding parameter and  $u_0$  is an initial approximation of  $u$ . The solution is sought in the form

$$u = u_0 + pu_1 + p^2u_2 + p^3u_3 + p^4u_4 + p^5u_5 \dots \quad (18)$$

In our case  $t$  corresponds to  $r$ ,  $x$  to  $u$  and the left side of (13) corresponds to  $L(u) + N(u)$  while  $f(t) = 0$ . Hence

$$H(x, p) = (1 - p)\left(\frac{d^2x}{dt^2} - \frac{d^2x_0}{dt^2}\right) + p\left(\frac{d^2x}{dt^2} + \alpha\frac{dx}{dt} + \beta x - \gamma\varepsilon_0\frac{dx}{dt}\left(1 + x + \frac{x^2}{3} + \frac{x^3}{6}\right)\left(1 + \frac{Q}{RT}\right)\right) = 0 \quad (19)$$

where

$$x \simeq x_0 + px_1 + p^2x_2 + p^3x_3 + p^4x_4 + p^5x_5 = \sum_{\ell=0}^6 p^\ell x_\ell. \quad (20)$$

Consequently

$$H(x, p) = (1 - p)\frac{d^2}{dt^2} \sum_{\ell=0}^6 p^\ell x_\ell + p\left\{\frac{d^2}{dt^2} \sum_{\ell=0}^6 p^\ell x_\ell + \alpha\frac{d}{dt} \sum_{\ell=0}^6 p^\ell x_\ell + \beta \sum_{\ell=0}^6 p^\ell x_\ell - \gamma\varepsilon_0\left(\frac{d}{dt} \sum_{\ell=0}^6 p^\ell x_\ell\right)\left[1 + \sum_{\ell=0}^6 p^\ell x_\ell + \frac{1}{3}\left(\sum_{\ell=0}^6 p^\ell x_\ell\right)^2 + \frac{1}{6}\left(\sum_{\ell=0}^6 p^\ell x_\ell\right)^3\right]\left(1 + \frac{Q}{RT}\right)\right\} = 0. \quad (21)$$

By making the coefficients of  $p^\ell$  ( $\ell = 0, 1, \dots, 5$ ) equal to zero we can obtain the solutions for  $x_\ell$ . Expanding and resolving equation (21) the coefficients of  $p^\ell$  are as follows:

$$p^0; \quad \frac{d^2 x_0}{dt^2} = 0, \quad (22)$$

$$p^1; \quad \beta x_0 + \alpha \frac{dx_0}{dt} - \left(1 + \frac{Q}{RT}\right) \gamma \varepsilon_0 \left[ \frac{dx_0}{dt} + x_0 \frac{dx_0}{dt} + \frac{1}{2} x_0^2 x_1 \frac{dx_0}{dt} + \frac{1}{6} x_0^3 \frac{dx_0}{dt} \right] + \frac{d^2 x_0}{dt^2} + \frac{d^2 x_1}{dt^2} = 0, \quad (23)$$

$$p^2; \quad \beta x_1 + \alpha \frac{dx_1}{dt} + \frac{d^2 x_2}{dt^2} - \left(1 + \frac{Q}{RT}\right) \gamma \varepsilon_0 \left( x_1 \frac{dx_0}{dt} + x_0 x_1 \frac{dx_0}{dt} + \frac{1}{2} x_0^2 x_1 \frac{dx_0}{dt} + \frac{dx_1}{dt} + x_0 \frac{dx_1}{dt} + \frac{1}{2} x_0^2 \frac{dx_1}{dt} + \frac{1}{6} x_0^3 \frac{dx_1}{dt} \right) = 0, \quad (24)$$

$$p^3; \quad \beta x_2 + \alpha \frac{dx_2}{dt} + \frac{d^2 x_3}{dt^2} + \alpha \frac{dx_3}{dt} - \left(1 + \frac{Q}{RT}\right) \gamma \varepsilon_0 \left( \frac{1}{2} x_1^2 \frac{dx_0}{dt} + \frac{1}{2} x_0 x_1^2 \frac{dx_0}{dt} + x_2 \frac{dx_0}{dt} + x_0 x_2 \frac{dx_0}{dt} + \frac{1}{2} x_0^2 x_2 \frac{dx_0}{dt} + x_1 \frac{dx_1}{dt} + x_0 x_1 \frac{dx_1}{dt} + \frac{1}{2} x_0^2 x_1 \frac{dx_1}{dt} + \frac{dx_2}{dt} + x_0 \frac{dx_2}{dt} + \frac{1}{2} x_0^2 \frac{dx_2}{dt} + \frac{1}{6} x_0^3 \frac{dx_2}{dt} \right) = 0, \quad (25)$$

$$p^4; \quad \beta x_3 + \frac{d^2 x_4}{dt^2} - \left(1 + \frac{Q}{RT}\right) \gamma \varepsilon_0 \left( \frac{1}{6} x_1^3 \frac{dx_0}{dt} + x_1 x_2 \frac{dx_0}{dt} + x_0 x_1 x_2 \frac{dx_0}{dt} + x_3 \frac{dx_0}{dt} + x_0 x_3 \frac{dx_0}{dt} + \frac{1}{2} x_0^2 x_3 \frac{dx_0}{dt} + \frac{1}{2} x_1^2 \frac{dx_1}{dt} + \frac{1}{2} x_0 x_1^2 \frac{dx_1}{dt} + x_2 \frac{dx_1}{dt} + x_0 x_2 \frac{dx_1}{dt} + \frac{1}{2} x_0^2 x_2 \frac{dx_1}{dt} + x_1 \frac{dx_2}{dt} + x_0 x_1 \frac{dx_2}{dt} + \frac{1}{2} x_0^2 x_1 \frac{dx_2}{dt} + \frac{dx_3}{dt} + x_0 \frac{dx_3}{dt} + \frac{1}{2} x_0^2 \frac{d^2 x_3}{dt^2} + \frac{1}{6} x_0^3 \frac{dx_3}{dt} \right) = 0. \quad (26)$$

The boundary conditions associated with the solution are as follows:

$$x_0(0) = x_1(0) = \dots = x_4(0) = 0. \quad (27)$$

Making use of equations (22)-(26) and the initial conditions (27) the following solutions are obtained for  $x_\ell$  ( $\ell = 1, \dots, 4$ ):

$$x_0 = \lg \left( \varepsilon_0 - \frac{\varepsilon_i}{\varepsilon_0} \right), \quad (28)$$

$$x_1 = -t^2 \beta x_0 / 2, \quad (29)$$

$$x_2 = \frac{1}{72RT} t^3 \beta x_0 [3RT(4\alpha + t\beta) - 2\gamma \varepsilon_0 (Q + RT) (6 + 6x_0 + 3x_0^2 + x_0^3)], \quad (30)$$

$$x_3 = \frac{1}{4320R^2T^2} t^4 \beta x_0 \times$$

$$\left\{ 6R^2t^2T^2\beta^2 + 5[-6RT\alpha + (Q + RT)\gamma(6 + 6x_0 + 3x_0^2 + x_0^3)\varepsilon_0]^2 + \right. \\ \left. + 6RtT\beta[12RT\alpha - (Q + RT)\gamma(12 + 30x_0 + 24x_0^2 + 11x_0^3)\varepsilon_0] \right\}, \quad (31)$$

$$x_4 = \frac{t^5\beta x_0}{362880} \left\{ 9R^3t^3T^3\beta^3 + 14(6RT\alpha - (Q + RT)\gamma\varepsilon_0(6 + 6x_0 + 3x_0^2 + x_0^3))^3 + \right. \\ \left. + 36R^2t^2T^2\beta^2[6RT\alpha - (Q + RT)\gamma\varepsilon_0(6 + 42x_0 + 69x_0^2 + 49x_0^3)] + \right. \\ \left. + 42RtT\beta[36R^2T^2\alpha^2 - 6RT(Q + RT)\alpha\gamma\varepsilon_0(12 + 38x_0 + 32x_0^2 + 15x_0^3)] + \right. \\ \left. + (Q + RT)^2\gamma^2\varepsilon_0^2(36 + 228x_0 + 384x_0^2 + 360x_0^3 + 203x_0^4 + 71x_0^5 + 14x_0^6) \right\} \quad (32)$$

With  $x_0, x_1, x_3, x_4$  and  $x_5 - x_5$  is not presented here – the solution for  $x$  is

$$x(t) \simeq \sum_{\ell=0}^5 x_{\ell}(t) \quad (33)$$

It follows on the basis of the strain equation (8) that

$$\varepsilon(t) \simeq \varepsilon_0^2 - \varepsilon_0 e^x. \quad (34)$$

If  $\varepsilon_0 = 1$  we have

$$\varepsilon(t) \simeq 1 - e^x \quad (35)$$

or

$$\varepsilon(t) \simeq 1 - e^{\sum_{\ell=0}^5 x_{\ell}(t)}. \quad (36)$$

## 6. METHOD OF SOLUTION 2

**6.1. Differential transforms method.** The second method applied to solving the nonlinear differential equation (13) is called DTM. The fundamental definitions and the operational characteristics of the method developed by Zhou in 1986 [16, 17] are given below.

Let  $u(t)$  be an analytic function differentiable continuously in the domain  $T$ . Then  $u(t)$  is differentiable continuously with respect to time  $t$ :

$$\frac{d^p u(t)}{dt^p} = \varphi(t, p) \quad \forall t \in T \quad (37)$$

For  $t = t_i$  it holds that  $\varphi(t, k) = \varphi(t_i, k)$ , where  $k$  is a non-negative integer. Equation (37) can, therefore, be rewritten as

$$U(k) = \varphi(t_i, k) = \left. \frac{d^k u(t)}{dt^k} \right|_{t=t_i} \quad (38)$$

where  $U(k)$  is called the spectrum of  $u(t)$  at  $t = t_i$ . Using Taylor series  $u(t)$  can be expressed as

$$u(t) = \sum_{k=0}^{\infty} \frac{(t - t_i)^k}{k!} U(k) \quad (39)$$

Equation (39) is called the inverse of  $U(k)$ . The differential transform of  $u(t)$  is defined by the equation

$$U(k) = \frac{H^k}{k!} \left. \frac{d^k u(t)}{dt^k} \right|_{t=0} \quad k = 0, 1, 2, \dots \quad (40a)$$

in which  $U(k)$  represents the transformed function and  $u(t)$  is the original function. The function  $U(k)$  is confined in the interval  $t \in [0, H]$  where  $H$  is a given constant number. The differential inverse transformation of  $U(k)$  is defined as

$$u(t) = \sum_{k=0}^{\infty} \left( \frac{t}{H} \right)^k U(k). \quad (40b)$$

### 6.2. The operational properties of the differential transformation method.

Let  $u(t)$  and  $v(t)$  be the functions of  $t$ . The transformed functions are denoted by  $U(k)$  and  $V(k)$ . It can be shown by using the fundamental mathematical operations of DTM that for instance

- i. If  $z(t) = \frac{du(t)}{dt}$  then  $Z(k) = (k-1) U(k+1)$ ;
- ii. If  $z(t) = u(t)v(t)$  then  $Z(k) = \sum_{r=0}^k U(r)V(k-r) \quad r = 0, 1, 2, \dots$ ;
- iii. If  $z(t) = u^m(t)$  then  $Z(k) = \sum_{r=0}^k U^{m-1}(r)U(k-r) \quad m = 1, 2, 3, \dots$ .

**6.3. DTM Solution Procedures.** Hence, the differential transformation of equations (8) and (13) yields the following recursive equation:

$$\begin{aligned} x_{k+2} = & -\frac{1}{(k+1)(k+2)} \left\{ \alpha(k+1)x_{k+1} + \beta x_k - \right. \\ & - y\varepsilon_o \left( 1 + \frac{Q}{RT} \right) \left[ (k+1)x_{k+1} + \sum_{l=0}^k (l+1)x_{l+1}x_{k-l} + \right. \\ & + \frac{1}{3} \sum_{p=0}^k \left( \sum_{l=0}^p (l+1)x_{l+1}x_{p-l}x_{k-p} \right) + \\ & \left. \left. + \frac{1}{6} \sum_{m=0}^k \left( \sum_{p=0}^m \left( \sum_{l=0}^p (l+1)x_{l+1}x_{p-l}x_{m-p}x_{k-m} \right) \right) \right] \right\} \quad (41) \end{aligned}$$

The initial conditions are of the form:

$$x_0 = \ln \left( \frac{\varepsilon_o^2 - \varepsilon}{\varepsilon_o} \right) \quad x_1 = 0.$$

Assuming that  $k = 2, 3, 4, 5$  we have solved equation (41) for  $x_2, x_3, x_4$  and  $x_5$  – here the results are presented for  $x_2, x_3$  and  $x_4$  only:

$$x_2 = -\beta x_0 / 2, \quad (42)$$

$$x_3 = \frac{1}{6} \alpha \beta x_0 + \frac{1}{6} y \varepsilon_o \beta \left( 1 + \frac{Q}{RT} \right) \left( x_0 + x_0^2 + \frac{1}{3} x_0^3 + \frac{1}{d6} x_0^4 \right), \quad (43)$$

$$\begin{aligned}
x_4 = & -\frac{1}{4}\alpha \left[ \frac{1}{6}\alpha\beta x_0 + \frac{1}{6}y\varepsilon_o\beta \left(1 - \frac{Q}{RT}\right) \left(x_0 + x_0^2 + \frac{1}{3}x_0^3 + \frac{1}{6}x_0^4\right) \right] + \\
& + \frac{1}{24}\beta^2 x_0 + \frac{1}{12}y\varepsilon_o \left(1 + \frac{Q}{RT}\right) - \frac{1}{2}y\varepsilon_o\beta \left(1 + \frac{Q}{RT}\right) \left(x_0 + x_0^2 + \frac{1}{3}x_0^3 + \frac{1}{6}x_0^4\right) + \\
& + 3 \left( \frac{1}{6}\alpha\beta x_0 - \frac{1}{6}y\varepsilon_o\beta x_0 \left(1 + \frac{Q}{RT}\right) \left(x_0 + x_0^2 + \frac{1}{3}x_0^3 + \frac{1}{6}x_0^4\right) \right) + \\
& + \left( \frac{1}{6}\alpha\beta x_0 - \frac{1}{6}y\varepsilon_o\beta x_0^2 \left(1 + \frac{Q}{RT}\right) \left(x_0 + x_0^2 + \frac{1}{3}x_0^3 + \frac{1}{6}x_0^4\right) \right) + \\
& + \frac{1}{2} \left( \frac{1}{6}\alpha\beta x_0 - \frac{1}{6}y\varepsilon_o\beta x_0^3 \left(1 + \frac{Q}{RT}\right) \left(x_0 + x_0^2 + \frac{1}{3}x_0^3 + \frac{1}{6}x_0^4\right) \right) \quad (44)
\end{aligned}$$

With  $x_\ell$  the solution is of the form

$$x(t) \simeq \sum_{\ell=0}^5 x_\ell t^\ell \quad (45)$$

while the strain function is given by

$$\varepsilon(t) = \varepsilon_o^2 - \varepsilon_o e^{x(t)} \quad (46)$$

from where by substituting (45) we have

$$\varepsilon(t) \simeq \varepsilon_o^2 - \varepsilon_o e^{\sum_{\ell=0}^5 x_\ell t^\ell}. \quad (47)$$

## 7. RESULTS AND DISCUSSION

The results obtained by applying the homotopy perturbation and differential transform methods to the analysis of the problem of temperature effects on relaxation of creep strain in polymeric biomaterials are presented in Table 1. In order to validate these results, the fourth order Runge-Kutta numerical method is applied to solve the same problem. The results are compared and shown in Table 1. This comparison is also shown in Figures 2a and b. For Figure 2a, the HPM solution is obtained by using four iterative terms ( $n = 4$ ) while for Figure 2b the number of iterative terms is increased to twelve ( $n = 12$ ). This shows that the higher the number of terms in the HPM model solution, the more accurate the solution will be. An error analysis shows that minimal error exists in the solutions obtained with the methods DTM and HPM.

The general description of how the material responds with an initial strain of 0.9 is also shown in Figure 2. The biomaterial does not exhibit an instant response to loading, but rather undergoes relaxation before it begins to respond to loading. In addition, as the temperature increases, the relaxation time increases, and the deformation increases proportionally at different temperatures.



Table 1. Comparison of HPM, DTM and numerical method results

Results obtained by the use of homotopy perturbation method if $\varepsilon_i = 0.9$ , $\varepsilon_0 = 1$ , $\alpha = 2$ , $\beta = 0.5$ , $\gamma = 0.9$ , $Q = 5000 J/mol$ , $R = 8.314 J/molK$ , $T = 300K$						
Time $t$	HPM <sub>1</sub> ( $n = 4$ ) Solution	HPM <sub>2</sub> ( $n = 12$ ) Solution	DTM Solution	Numerical Solution (RK4)	Error Difference DTM-RK4	Error Difference HPM <sub>2</sub> -RK4
	Strain $\varepsilon(t)$					
0.00	0.9000000	0.9000000	0.9000000	0.9000000	0.00000000	0.00000000
0.10	0.8995268	0.8995267	0.8995267	0.8995267	0.00000000	0.00000000
0.20	0.8984212	0.8984150	0.8984150	0.8984150	0.00000000	0.00000000
0.30	0.8970945	0.8970225	0.8970225	0.8970225	0.00000000	0.00000000
0.40	0.8961919	0.8957820	0.8957820	0.8957820	0.00000000	0.00000000
0.50	0.8970340	0.8954685	0.8954685	0.8954685	0.00000000	0.00000000
0.60	0.9019594	0.8974244	0.8974244	0.8974244	0.00000000	0.00000000
0.70	0.9139977	0.9035709	0.9035709	0.9035709	0.00000000	0.00000000
0.80	0.9348554	0.9158586	0.9158586	0.9158586	0.00000000	0.00000000
0.90	0.9612801	0.9348325	0.9348325	0.9348325	0.00000000	0.00000000
1.00	0.9842194	0.9578233	0.9578233	0.9578233	0.00000000	0.00000000
1.10	0.9963269	0.9789104	0.9789104	0.9789104	0.00000000	0.00000000
1.20	0.9996162	0.9926209	0.9926209	0.9926209	0.00000000	0.00000000
1.30	0.9999868	0.9984012	0.9984012	0.9984012	0.00000000	0.00000000
1.40	0.9999999	0.9998149	0.9998149	0.9998149	0.00000000	0.00000000
1.50	1.0000000	0.9999904	0.9999904	0.9999904	0.00000000	0.00000000
1.60	1.0000000	0.9999998	0.9999998	0.9999998	0.00000000	0.00000000
1.70	1.0000000	1.0000000	1.0000000	1.0000000	0.00000000	0.00000000
1.80	1.0000000	1.0000000	1.0000000	1.0000000	0.00000000	0.00000000
1.90	1.0000000	1.0000000	1.0000000	1.0000000	0.00000000	0.00000000
2.00	1.0000000	1.0000000	1.0000000	1.0000000	0.00000000	0.00000000

*Thermal coefficient at varying temperatures.* The response of the biomaterial to varying thermal coefficients is shown in Figure 2. It is observed that an increase in the thermal coefficient resulted in a decrease in the deformation and an increase in the rate of relaxation in the material. It is also observed that the material shows a high resistance to deformation at high thermal coefficient.

The effect of four thermal conductivity coefficients  $\gamma$  at different temperatures of the material model is shown in Figure 4. The differences among the responses at these different temperatures are minimal. Material exhibits longer relaxation before it begins to deform at lower thermal conductivity coefficients than at higher thermal conductivity coefficients. There is sharp increase in deformation at higher thermal conductivity coefficients.

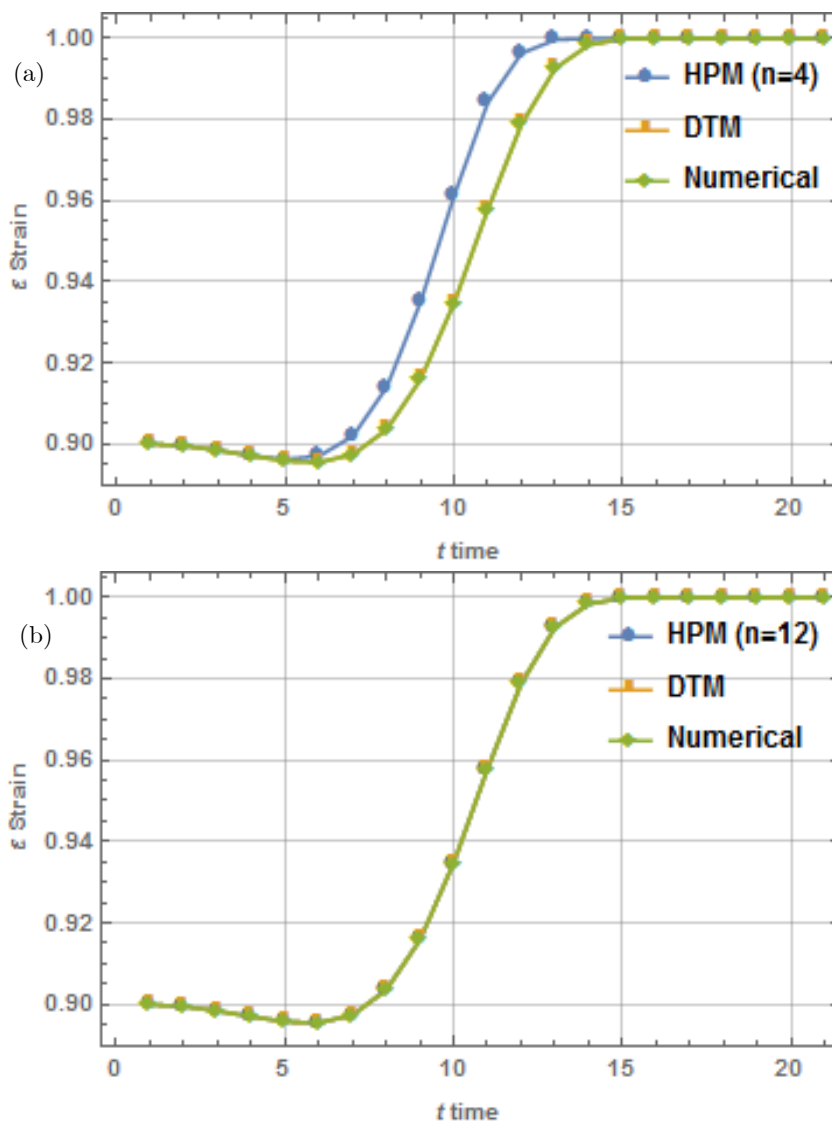


Figure 2. Comparison of the numerical results obtained by using the three methods; DTM, HPM and the fourth order Runge-Kutta method ( $\epsilon_i = 0.9$ ,  $\epsilon_0 = 1$ ,  $\alpha = 2$ ,  $\beta = 0.5$ ,  $\gamma = 0.9$ ,  $Q = 5000\text{J/mol}$ ,  $R = 8.314\text{J/mol K}$ ,  $T = 300\text{K}$ ); (a)  $n = 4$ , (b)  $n = 12$

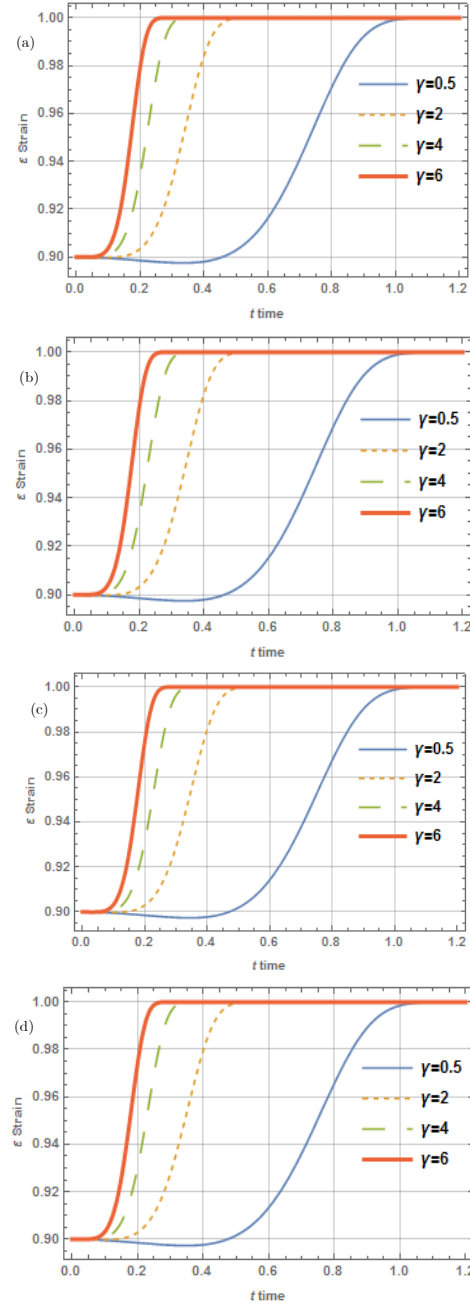


Figure 3. Variation of thermal coefficients at different temperatures ( $\epsilon_i=0.9$ ,  $\epsilon_0=1$ ,  $Q=50000\text{J/mol}$ ,  $R=8.314\text{J/mol K}$ ,  $\alpha=0.5$ ,  $\beta=0.5$ , (a)  $T=300\text{K}$ , (b)  $T=305\text{K}$ , (c)  $T=310\text{K}$ , (d)  $T=315\text{K}$ )

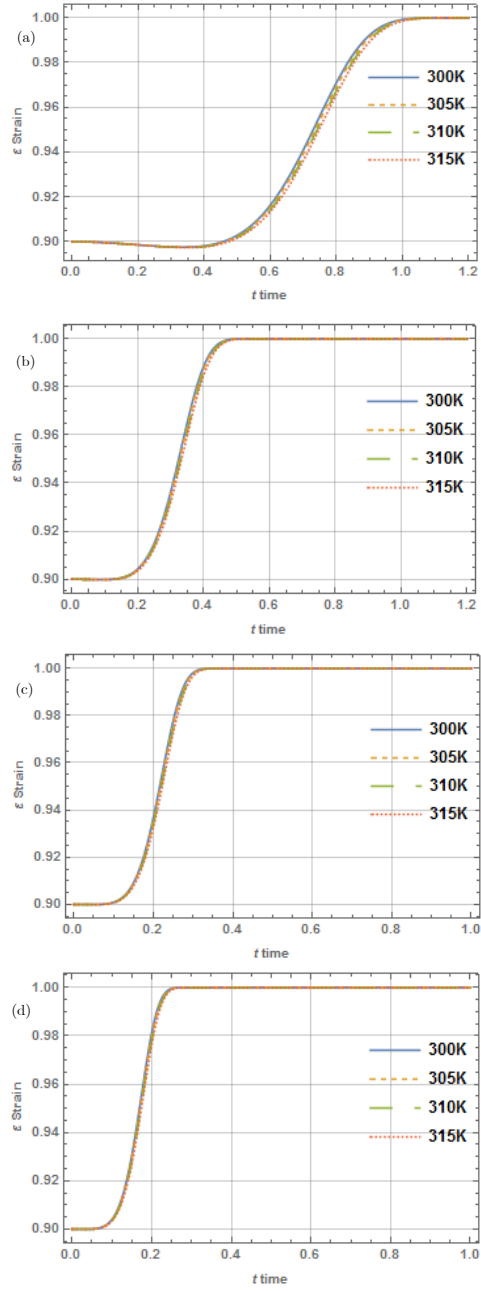


Figure 4. Temperature variation with thermal conductivity ( $\epsilon_i = 0.9$ ,  $\epsilon_0 = 1$ ,  $Q = 50000 \text{ J/mol}$ ,  $R = 8.314 \text{ J/mol K}$ ,  $\alpha = 2$ ,  $\beta = 0.5$ , (a)  $\gamma = 0.5$ , (b)  $\gamma = 2$ , (c)  $\gamma = 4$ , (d)  $\gamma = 6$ )

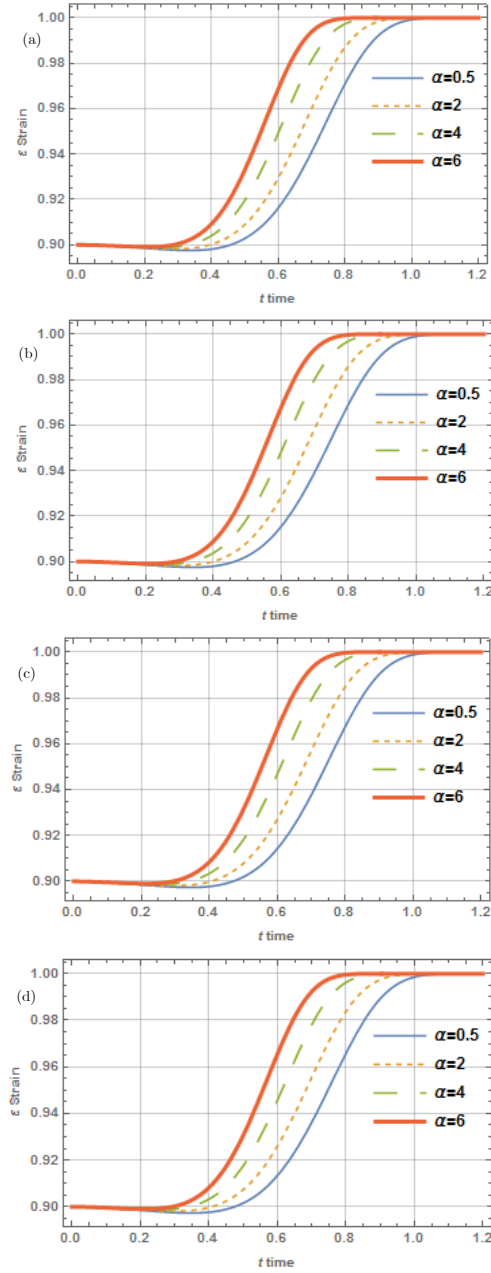


Figure 5. The effects of the viscosity coefficient on the developed model ( $\epsilon_i = 0.9$ ,  $\epsilon_0 = 1$ ,  $Q = 50000J/mol$ ,  $R = 8.314J/mol\ K$ ,  $\alpha = 2$ ,  $\beta = 0.5$ ,  $\gamma = 0.5$ , (a)  $T = 300K$ , (b)  $T = 305K$ , (c)  $T = 310K$ , (d)  $T = 315K$ )

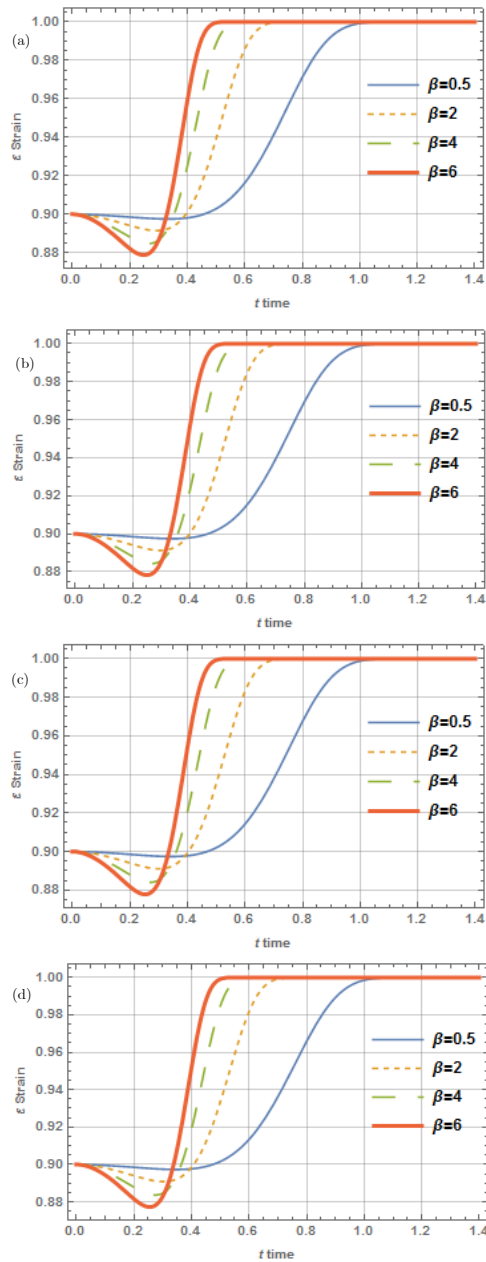


Figure 6. The effects of the stiffness coefficient on the developed model ( $\epsilon_i = 0.9$ ,  $\epsilon_0 = 1$ ,  $Q = 50000J/mol$ ,  $R = 8.314J/molK$ ,  $\alpha = 2$ ,  $\beta = 0.5$ ,  $\gamma = 0.5$ , (a)  $T = 300K$ , (b)  $T = 305K$ , (c)  $T = 310K$ , (d)  $T = 315K$ )

*Viscosity coefficient at varying temperatures.* Figure 5 show the response of a material at a varying viscosity coefficient  $\alpha$  of 0.5, 2, 4 and 6. As the viscosity coefficient increases, the difference in the deformation path between the high and low temperature decreases. It is also observed that at a relatively low viscosity, material tends to deform more compared to when it is high, i.e. there is an increase in resistance to deformation as the viscosity coefficient increases. Similarly, at low viscosity, the relaxation period takes a longer time before the material begins to deform.

*Stiffness coefficient at varying temperatures.* The response of the material to different stiffness coefficients  $\beta$  is shown in Figure 6. It is observed that the higher the stiffness coefficient, the shorter time the material takes to deform. The relaxation time was shorter for a material with higher stiffness and lower temperature, while materials with lower stiffness as shown in Figure 6a tend to show higher resistance to deformation than those with a lower stiffness coefficient.

## 8. CONCLUSION

In this study, the analytical solution of the effects of temperature on relaxation of creep strain in polymeric biomaterials governed by a developed nonlinear differential equation has been presented. The developed model was solved using two efficient methods; the homotopy perturbation method and differential transform method. The obtained results were validated with the fourth-order Runge-Kutta numerical method and the error analysis showed good agreement among the results. The effects of thermal conductivity, viscosity and material stiffness on the deformation of these biomaterials were investigated. As the thermal conductivity and viscosity of the material increase, its resistance to deformation increases, while an increase in the material stiffness resulted in an increase in the rate of deformation and relaxation. The analytical solution developed in this work provides a better understanding of the relationship between the physical quantities of the problem investigated. The results obtained in this theoretical investigation will assist in the analysis of the temperature effects on relaxation of creep strain in biomaterials and in the handling of various parameters in the developed model.

## REFERENCES

1. I. D. Ibrahim, E. R. Sadiku, T. Jamiru, A. Hamam, and W. K. Kupolati. "Applications of polymers in the biomedical field." *Current Trends Biomedical Engineering Bioscience*, **4**, (2017), pp. 9–11. DOI: 10.19080/CTBEB.2017.04.555650.
2. J. L. Drury, R. G. Dennis, and D. J. Mooney. "The tensile properties of alginate hydrogels." *Biomaterials*, **25**, (2004), 3187–3199. DOI: 10.1016/j.biomaterials.2003.10.002.
3. J. B. Park and R. S. Lakes. "Structure—Property Relationships of Biological Materials." *Biomaterials, An Introduction*, Springer, 1992. Chap. 9, pp. 185–222. DOI: 10.1007/978-1-4684-3423-1.
4. F. H. Silver, J. W. Freeman, and G. Bradica. "Orthopedic Biology and Medicine." *Repair and Regeneration of Ligaments, Tendons, and Joint Capsule*. Ed. by William R. Walsh. Springer, 1992. Chap. 1, pp. 15–47. DOI: 10.1385/1592599427.

5. M. D. Monsia. "A mathematical model for predicting the relaxation of creep strains in materials." *Physical Review & Research International*, **2**(3), (2012), pp. 107–124.
6. R. H. Ewoldt, A. E. Hosoi, and G. H. McKinley. "Nonlinear viscoelastic biomaterials: meaningful characterization and engineering inspiration." *Integrative and Comparative Biology*, **49**(1), (2009), pp. 40–50. DOI: 10.1093/icb/icp010.
7. B. K. Appelt. "Advanced Substrates: A Materials and Processing Perspective." *Materials for Advanced Packaging*, ed. by Lu D. and Wong C. Springer, Cham, 2017, pp. 287–330. DOI: 10.1007/978-3-319-45098-8\_7.
8. L. M. Lazaro and D. A. G. Aranda. "Process temperature profile and rheological properties of greases from vegetable oils." *Green and Sustainable Chemistry*, **04**(1), (2014), pp. 38–43. DOI: 10.4236/gsc.2014.41007.
9. A. Hernandez-Jimenez, J. Hernandez-Santiago, A. Macias-Carcia, and J. Sanchez-Gonzalez. "Relaxation modulus in PMMA and PTFE fitting by fractional Maxwell model." *Polymer Testing*, **21**(3), (2014), pp. 325–331. DOI: 10.1016/S0142-9418(01)00092-7.
10. M. Abu-Abdeen. "Single and double-step stress relaxation and constitutive modeling of viscoelastic behavior of swelled and un-swelled natural rubber loaded with carbon black." *Materials and Design*, **31**(4), (2010), 2078–2084. DOI: 10.1016/j.matdes.2009.10.006.
11. J. H. He. "Homotopy perturbation method: A new nonlinear analytical technique." *Applied Mathematics and Computation*, **135**(1), (2003), pp. 73–79. DOI: 10.1016/S0096-3003(01)00312-5.
12. T. Öziş and A. Yıldırım. "Homotopy perturbation method: A new nonlinear analytical technique." *Computers & Mathematics with Applications*, **56**(5), (2008), pp. 1216–1224. DOI: 10.1016/j.camwa.2008.02.023.
13. S. Saedodin and M. Shahbabaie. "Thermal analysis of natural convection in porous fins with homotopy perturbation method (HPM)." *Arabian Journal for Science and Engineering*, **38**(8), (2013), 2227–2231. DOI: 10.1007/s13369-013-0581-6.
14. H. A. Hoshyar, I. Rahimipetroudi, D. D. Ganji, and A. R. Majidian. "Thermal performance of porous fins with temperature-dependent heat generation via homotopy perturbation method and collocation method." *Journal of Applied Mathematics and Computational Mechanics*, **14**(4), (2015), pp. 53–65. DOI: 10.17512/jamcm.2015.4.06.
15. O. A. Adeleye and A. Yinusa. "Heat transfer analysis of non-newtonian natural convective fluid flow using homotopy perturbation and Daftardar-Gejji and Jafari methods." *Journal of Applied Mathematics and Computational Mechanics*, **18**(2), (2015), pp. 5–18. DOI: 10.17512/jamcm.2019.2.01.
16. J.K. Zhou. *Differential Transformation and its Applications for Electrical Circuits*. Huazhong University Press, 1986.
17. Xi Chen, Jie Xiang Lou, and Ying Dai. "Differential transform method for the brooks - Corey model." *Advances in Civil and Structural Engineering III*, vol. 501. Applied Mechanics and Materials. Trans Tech Publications Ltd., Apr. 2014, pp. 2520–2523. DOI: 10.4028/www.scientific.net/AMM.501-504.2520.



18. T. M. Elzaki and E. M. A. Hilal. "Solution of linear and nonlinear partial differential equations using mixture of Elzaki transform and the projected differential transform method." *Journal of Applied Mathematics and Computational Mechanics*, **2**(1), (2012), pp. 50–59.
19. M. Garg, P. Manohar, and S. L. Kalla. "Generalized differential transform method to space-time fractional telegraph equation." *International Journal of Differential Equations*, Article ID 548982, (2011), pp. 1–10. DOI: 10.1155/2011/548982.
20. O. O. Agboola, A. A. Opanuga, and J. A. Gbadeyan. "Solution of third order ordinary differential equations using differential transform method." *Global Journal of Pure and Applied Mathematics*, **11**(4), (2015), pp. 2511–2517.
21. S. Mukherjee, D. Goswami, and B. Roy. "Solution of higher-order Abel equations by differential transform method." *International Journal of Modern Physics C*, **23**(9), (2012), pp. 1250056–3. DOI: 10.1142/S0129183112500568.
22. C. Kuo, M. Fanton, L. Wu, and D. Camarillo. "Spinal constraint modulates head instantaneous center of rotation and dictates head angular motion." *Journal of Biomechanics*, **76**, (2018), pp. 220–228. DOI: 10.1016/j.jbiomech.2018.05.024.
23. M. Thongmoon and S. Pusjuso. "The numerical solution of differential transform method and Laplace transform method for a system of differential equations." *Nonlinear Analysis: Hybrid Systems*, **4**(3), (2018), pp. 425–431. DOI: 10.1016/j.nahs.2009.10.006.
24. O. Adeleye, O. Olawale, and G. Sobamowo. "Prediction of phagocyte transmigration for foreign body responses to subcutaneous biomaterial implantations using differential transform method." *Journal of Biomimetics, Biomaterials and Biomedical Engineering*, **32**(7), (2017), pp. 98–114. DOI: 10.4028/www.scientific.net/JBBBE.32.98.
25. O. Adeleye, A. Eloka, and G. Sobamowo. "Prediction of creep strain relaxations in biomaterials using differential transformation method." *Journal of Biomimetics, Biomaterials and Biomedical Engineering*, **38**(8), (2018), pp. 11–22. DOI: 10.4028/www.scientific.net/JBBBE.38.11.
26. R. D. Bauer. "Rheological approaches of arteries." *Journal of Biomimetics, Biomaterials and Biomedical Engineering*, **23**(1), (1984), pp. 159–167. DOI: 10.3233/bir-1984-23s129.
27. G. Z. Quan, Y. Shi, Y. X. Wang, Kang B. S., Ku T. W., and Song W. J. "Constitutive modelling for the dynamic recrystallization evolution of AZ80 magnesium alloy based on stress-strain data." *Journal of Biomimetics, Biomaterials and Biomedical Engineering*, **528**(28), (2011), pp. 8051–8059. DOI: 10.1016/j.msea.2011.07.064.
28. C. X. Yue, L. W. Zhang, S. L. Liao, J. B. Pei, H. J. Gao, Y. W. Jia, and X. Lian. "Research on the dynamic recrystallization behaviour of Gcr15 steel." *Materials Science and Engineering: A*, **499**(1-2), (2009), pp. 177–181. DOI: 10.1016/j.msea.2007.11.123.



## A THEORY FOR THE LONGITUDINAL VIBRATIONS OF ANISOTROPIC ELASTIC BARS BASED ON THE RAYLEIGH-BISHOP MODEL

ISTVÁN ECSEDI AND ATTILA BAKSA

Institute of Applied Mechanics, University of Miskolc

H-3515 Miskolc-Egyetemváros, Hungary

[mechecs@uni-miskolc.hu](mailto:mechecs@uni-miskolc.hu), [mechab@uni-miskolc.hu](mailto:mechab@uni-miskolc.hu)

[Received: February 11, 2019; Accepted: May 6, 2019]

**Abstract.** A Rayleigh-Bishop type theory of the longitudinal vibrations is developed for anisotropic bars. The equation of motion and the associated boundary conditions are derived by the use of Hamilton's principle. For an orthotropic bar the dependence of the eigenfrequencies from the position of the material coordinate system is analyzed. The numerical results obtained by the application of approximate analytical solution for the eigenfrequencies are compared with a FEM solution.

*Mathematical Subject Classification:* 74K10, 74H45, 74E10

*Keywords:* Longitudinal vibrations, bar, anisotropic, Rayleigh-Bishop theory.

### 1. INTRODUCTION

Modeling of vibration problems of elastic structural components is of great importance in engineering. The longitudinal vibration of thin isotropic elastic bar has been studied by many researchers over a long time owing to its wide applications in engineering [1–6]. The classical approximate theory of longitudinal vibration of isotropic bar was developed during the 18th century by J. D’Alembert, D. Bernoulli, L. Euler and J. Lagrange. This theory, which is called the simple theory of longitudinal vibration, is based on the analysis of the one-dimensional wave equation and is applicable for long and relatively thin bars vibrating at low frequency. The lateral effects and the corresponding lateral and axial shear modes are fully neglected in the frame of this simple theory of longitudinal vibration [1, 6]. J. Rayleigh [2] was the first who introduced the inertia of the lateral motions by which the cross sections are extended or contracted in their own planes. The lateral inertia effects are, however, important if the bar is thick. R. Bishop [7] further modified the Rayleigh theory in 1952 by taking into account the lateral shear effects. This theory is referred to as the Rayleigh-Bishop theory. From the point of view of the engineering applications this theory is slightly more complicated than the Rayleigh theory. The simple theory, the Rayleigh theory and Rayleigh-Bishop theory of longitudinal vibrations of isotropic bars are based on a fundamental assumption which says that the dynamics of the bar is described by a single unknown function and hence, a single partial differential equation containing the axial and time coordinates describes the longitudinal vibrations of isotropic

elastic bars. Another important assumption of the above mentioned three theories is that the axial displacements do not depend on the cross-sectional coordinates, they depend only on the axial and time coordinates. The stress boundary conditions on the cylindrical boundary surface of the bar are fully ignored in these theories.

In a paper by Shatalov *et al.* [8] the simple theory, the Rayleigh, Rayleigh-Bishop, Herrmann and multimode models of the longitudinal vibrations of isotropic bars are compared with the exact Pochhammer-Chree solutions of the axisymmetric vibration of an isotropic cylinder. Application of two kinds of eigenfunction orthogonality in the Rayleigh and Rayleigh-Bishop theories of longitudinal vibrations of thick isotropic elastic bars is presented by Fedotov *et al.* [9], which deals with the analytical solution of vibration problem based on Green's function. A paper by Shatalov *et al.* [10] presents the multimode theories of the longitudinal vibration of isotropic elastic bars. The multimode models formulated in [10] can be considered as generalizations of the classical Rayleigh and Rayleigh-Bishop theories.

In this paper an approximate theory of the longitudinal vibration of anisotropic bars is presented. Equations of motion and boundary conditions are derived from Hamilton's principle [6, 11]. In the derived model the inertia of the lateral motions by which the cross-sections are extended or contracted in their own planes is considered. The contribution of more than one stiffness coefficients (elastic moduli) of the general anisotropic material to the strain energy is introduced. From the assumed form of the displacement field a purely longitudinal (axial) vibration can be derived, so that the couplings between the longitudinal, torsional and flexural vibrations cannot be described in this approximate theory.

The connection between the position of material coordinate system, which is given by an angle coordinate, and the eigenfrequencies are analyzed for orthotropic bars. The numerical results obtained for the eigenfrequencies are checked by finite element computations.

## 2. MECHANICAL MODEL

The considered anisotropic elastic bar with uniform cross section is shown in Figure 1. The governing equations are formulated in the Cartesian coordinate system  $Oxyz$ . The position of the left end cross section is given by  $z = 0$ , and the position of the right-end cross section is determined by  $z = L$ , where  $L$  is the length of the bar. The  $z$  axis is the centerline of the bar while the  $x$  and  $y$  axes are the principal axes of the left-end cross section. Hence we have

$$\int_A x \, dA = \int_A y \, dA = 0, \quad \int_A xy \, dA = 0. \quad (2.1)$$

The material of the bar is a general anisotropic material referred to as triclinic material. In this case the generalized Hooke's law can be formulated as [12, 13]

$$\boldsymbol{\sigma} = \mathbf{C} \boldsymbol{\varepsilon}, \quad (2.2)$$

where

$$\boldsymbol{\sigma}^T = \begin{bmatrix} \sigma_x & \sigma_y & \sigma_z & \tau_{yz} & \tau_{xz} & \tau_{xy} \end{bmatrix}, \quad \boldsymbol{\varepsilon}^T = \begin{bmatrix} \varepsilon_x & \varepsilon_y & \varepsilon_z & \gamma_{yz} & \gamma_{xz} & \gamma_{xy} \end{bmatrix},$$

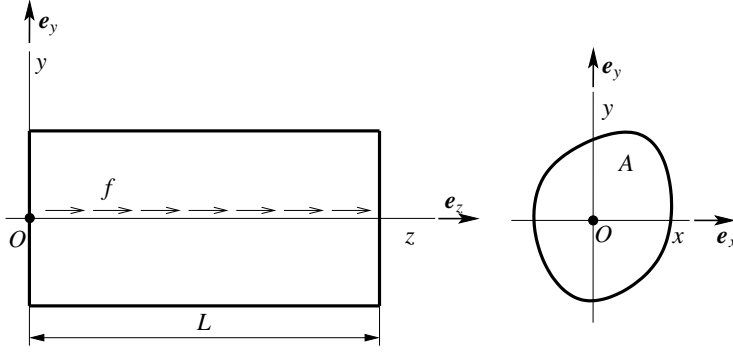


Figure 1. Anisotropic elastic bar with uniform cross section

$$C = \begin{bmatrix} c_{11} & c_{12} & c_{13} & c_{14} & c_{15} & c_{16} \\ c_{12} & c_{22} & c_{23} & c_{24} & c_{25} & c_{26} \\ c_{13} & c_{23} & c_{33} & c_{34} & c_{35} & c_{36} \\ c_{14} & c_{24} & c_{34} & c_{44} & c_{45} & c_{46} \\ c_{15} & c_{25} & c_{35} & c_{45} & c_{55} & c_{56} \\ c_{16} & c_{26} & c_{36} & c_{46} & c_{56} & c_{66} \end{bmatrix} = C^T$$

while  $\sigma_x$ ,  $\sigma_y$  and  $\sigma_z$  are the normal stresses,  $\tau_{yz}$ ,  $\tau_{xz}$  and  $\tau_{xy}$  are the shear stresses,  $\varepsilon_x$ ,  $\varepsilon_y$  and  $\varepsilon_z$  are the longitudinal strains,  $\gamma_{yz}$ ,  $\gamma_{xz}$  and  $\gamma_{xy}$  are the shear strains,  $c_{ij}$  ( $i, j = 1, \dots, 6$ ) are the elastic moduli of the considered anisotropic elastic material. The compliance matrix  $S$  is the inverse of stiffness matrix  $C$ :

$$\varepsilon = S\sigma, \quad S = C^{-1}, \quad (2.3)$$

where  $S = \{s_{ij}\}$  and  $s_{ij} = s_{ji}$  ( $i, j = 1, \dots, 6$ ).

Let the anisotropic bar be loaded at its end cross sections by uniform normal stresses, whose stress resultant is the axial force  $P$ . The displacement components associated with this axial force can be given in the following forms [12, 13]:

$$u = \frac{P}{A} \left( s_{13}x + \frac{1}{2}s_{36}y \right), \quad (2.4)$$

$$v = \frac{P}{A} \left( \frac{1}{2}s_{36}x + s_{23}y \right), \quad (2.5)$$

$$w = \frac{P}{A} (s_{35}x + s_{34}y + s_{33}z) \quad (2.6)$$

where  $u$ ,  $v$  and  $w$  are the displacement components parallel to the axes  $x$ ,  $y$  and  $z$ ;  $A$  is the area of the bar cross section;  $s_{13}$ ,  $s_{23}$ ,  $s_{33}$ ,  $s_{34}$ ,  $s_{35}$  and  $s_{36}$  are the flexibility coefficients. It can be seen by substituting  $P/A$  from the derivative of equation (2.6) with respect to  $z$  into equations (2.4) and (2.5) that

$$u = \left( \frac{s_{13}}{s_{33}}x + \frac{1}{2}\frac{s_{36}}{s_{33}}y \right) \frac{\partial w}{\partial z}, \quad (2.7)$$

$$v = \left( \frac{1}{2} \frac{s_{36}}{s_{33}} x + \frac{s_{23}}{s_{33}} y \right) \frac{\partial w}{\partial z}. \quad (2.8)$$

Equations (2.7) and (2.8) give the lateral displacements in the anisotropic bar in terms of axial displacement  $w$ . In the sequel we shall assume that for longitudinal vibrations the displacements in the directions  $x$  and  $y$  directions are given by equations (2.7) and (2.8) and the axial displacement  $w$  depends only on the axial coordinate  $z$  and the time coordinate  $t$ . All results of this paper are based on the above-mentioned assumptions. The equation of motion and the boundary conditions are derived from Hamilton's principle, which can be stated as

$$\delta \int_{t_1}^{t_2} (T - \Pi + W) dt = 0, \quad (2.9)$$

where  $T$  is the kinetic energy of the bar,  $\Pi$  is the strain energy and the work done by the external force  $f = f(z, t)$  is denoted by  $W$  (Figure 1). Of all of the possible varied paths only those are considered that coincide with the true path at the two instants  $t_1$  and  $t_2$  [4, 6, 11].

First we determine the kinetic energy starting from the following equation

$$\begin{aligned} T &= \frac{1}{2} \int_B \rho \left[ \left( \frac{\partial u}{\partial t} \right)^2 + \left( \frac{\partial v}{\partial t} \right)^2 + \left( \frac{\partial w}{\partial t} \right)^2 \right] dB \\ &= \frac{1}{2} \int_B \rho \left\{ \left[ \left( \frac{s_{13}}{s_{23}} x + \frac{1}{2} \frac{s_{36}}{s_{33}} y \right)^2 + \left( \frac{1}{2} \frac{s_{36}}{s_{33}} x + \frac{s_{23}}{s_{33}} y \right)^2 \right] \left( \frac{\partial^2 w}{\partial z \partial t} \right)^2 + \left( \frac{\partial w}{\partial t} \right)^2 \right\} dB. \end{aligned} \quad (2.10)$$

Here,  $B$  is the space domain occupied by the cylindrical bar,  $\rho$  is the mass density. A detailed computation, in which equation (2.1) has been used, yields

$$T = \frac{1}{2} \int_0^L \left[ A \rho \left( \frac{\partial w}{\partial t} \right)^2 + \rho I \left( \frac{\partial^2 w}{\partial z \partial t} \right)^2 \right] dz, \quad (2.11)$$

where

$$\begin{aligned} I &= \left[ \left( \frac{s_{13}}{s_{33}} \right)^2 + \frac{1}{4} \left( \frac{s_{36}}{s_{33}} \right)^2 \right] I_y + \left[ \frac{1}{4} \left( \frac{s_{36}}{s_{33}} \right)^2 + \left( \frac{s_{23}}{s_{33}} \right)^2 \right] I_x \\ &= \left\{ \left[ \left( \frac{s_{13}}{s_{33}} \right)^2 + \frac{1}{4} \left( \frac{s_{36}}{s_{33}} \right)^2 \right] i_y^2 + \left[ \frac{1}{4} \left( \frac{s_{36}}{s_{33}} \right)^2 + \left( \frac{s_{23}}{s_{33}} \right)^2 \right] i_x^2 \right\} A = i^2 A \end{aligned} \quad (2.12)$$

$$I_x = \int_A y^2 dA = i_x^2 A, \quad I_y = \int_A x^2 dA = i_y^2 A. \quad (2.13)$$

For an anisotropic linearly elastic material the strain energy density as a function of strain field is obtained as [12, 13]

$$\begin{aligned}
a(\varepsilon_x, \varepsilon_y, \varepsilon_z, \gamma_{yz}, \gamma_{xz}, \gamma_{xy}) = & \frac{1}{2} (c_{11}\varepsilon_x^2 + 2c_{12}\varepsilon_x\varepsilon_y + 2c_{13}\varepsilon_x\varepsilon_z + 2c_{14}\varepsilon_x\gamma_{yz} + \\
& 2c_{15}\varepsilon_x\gamma_{xz} + 2c_{16}\varepsilon_x\gamma_{xy} + c_{22}\varepsilon_y^2 + 2c_{23}\varepsilon_y\varepsilon_z + 2c_{24}\varepsilon_y\gamma_{yz} + 2c_{25}\varepsilon_y\gamma_{xz} + 2c_{26}\varepsilon_y\gamma_{xy} \\
& + c_{33}\varepsilon_z^2 + 2c_{34}\varepsilon_z\gamma_{yz} + 2c_{35}\varepsilon_z\gamma_{xz} + 2c_{36}\varepsilon_z\gamma_{xy} \\
& + c_{44}\gamma_{yz}^2 + 2c_{45}\gamma_{yz}\gamma_{xz} + 2c_{46}\gamma_{yz}\gamma_{xy} + 2c_{55}\gamma_{xz}^2 + 2c_{56}\gamma_{xz}\gamma_{xy} + c_{66}\gamma_{xy}^2), \quad (2.14)
\end{aligned}$$

in which

$$\begin{aligned}
\varepsilon_x &= \frac{s_{13}}{s_{33}} \frac{\partial w}{\partial z}, & \varepsilon_y &= \frac{s_{23}}{s_{33}} \frac{\partial w}{\partial z}, & \varepsilon_z &= \frac{\partial w}{\partial z}, \quad (2.15) \\
\gamma_{yz} &= \left( \frac{1}{2} \frac{s_{36}}{s_{33}} x + \frac{s_{23}}{s_{33}} y \right) \frac{\partial^2 w}{\partial z^2}, & \gamma_{xz} &= \left( \frac{s_{13}}{s_{33}} x + \frac{1}{2} \frac{s_{36}}{s_{33}} y \right) \frac{\partial^2 w}{\partial z^2}, & \gamma_{xy} &= \frac{s_{36}}{s_{33}} \frac{\partial w}{\partial z}. \quad (2.16)
\end{aligned}$$

The whole strain energy of the anisotropic cylindrical bar is calculated from the following equation

$$\Pi = \int_B a(\varepsilon_x, \varepsilon_y, \varepsilon_z, \gamma_{yz}, \gamma_{xz}, \gamma_{xy}) \, dB. \quad (2.17)$$

A detailed calculation in which equation (2.1) is also used leads to the result

$$\Pi = \frac{1}{2} \int_0^L \left[ C_1 \left( \frac{\partial w}{\partial z} \right)^2 + C_2 \left( \frac{\partial^2 w}{\partial z^2} \right)^2 \right] dz, \quad (2.18)$$

where

$$\begin{aligned}
C_1 &= \left[ c_{11} \left( \frac{s_{13}}{s_{33}} \right)^2 + c_{22} \left( \frac{s_{23}}{s_{33}} \right)^2 + c_{33} + c_{66} \left( \frac{s_{36}}{s_{33}} \right)^2 \right. \\
&\quad \left. + 2c_{12} \frac{s_{13}s_{23}}{s_{33}^2} + 2c_{13} \frac{s_{13}}{s_{33}} + 2c_{23} \frac{s_{23}}{s_{33}} + 2c_{16} \frac{s_{13}s_{36}}{s_{33}^2} + 2c_{26} \frac{s_{23}s_{36}}{s_{33}^2} + 2c_{36} \frac{s_{36}}{s_{33}} \right] A \\
&= \left[ \frac{c_{11}}{c_{33}} \left( \frac{s_{13}}{s_{33}} \right)^2 + \frac{c_{22}}{c_{33}} \left( \frac{s_{23}}{s_{33}} \right)^2 + 1 + \frac{c_{66}}{c_{33}} \left( \frac{s_{36}}{s_{33}} \right)^2 + 2 \frac{c_{12}}{c_{33}} \frac{s_{13}s_{23}}{s_{33}^2} + \right. \\
&\quad \left. 2 \frac{c_{13}}{c_{33}} \frac{s_{13}}{s_{33}} + 2 \frac{c_{23}}{c_{33}} \frac{s_{23}}{s_{33}} + 2 \frac{c_{16}}{c_{33}} \frac{s_{13}s_{36}}{s_{33}^2} + 2 \frac{c_{26}}{c_{33}} \frac{s_{23}s_{36}}{s_{33}^2} + 2 \frac{c_{36}}{c_{33}} \frac{s_{36}}{s_{33}} \right] c_{33} A = c_1 c_{33} A, \quad (2.19)
\end{aligned}$$

$$\begin{aligned}
C_2 &= \left[ \frac{1}{4} c_{44} \left( \frac{s_{36}}{s_{33}} \right)^2 + c_{45} \frac{s_{13}s_{36}}{s_{33}^2} + c_{55} \left( \frac{s_{13}}{s_{33}} \right)^2 \right] I_y \\
&\quad + \left[ c_{44} \left( \frac{s_{23}}{s_{33}} \right)^2 + c_{45} \frac{s_{23}s_{36}}{s_{33}^2} + c_{55} \frac{1}{4} \left( \frac{s_{36}}{s_{33}} \right)^2 \right] I_x \\
&= \left\{ \frac{1}{4} \frac{c_{44}}{c_{33}} \left( \frac{s_{36}}{s_{33}} \right)^2 + \frac{c_{45}}{c_{33}} \frac{s_{13}s_{36}}{s_{33}^2} + \frac{c_{55}}{c_{33}} \left( \frac{s_{13}}{s_{33}} \right)^2 \right\} i_y^2 \\
&\quad + \left\{ \frac{c_{44}}{c_{33}} \left( \frac{s_{23}}{s_{33}} \right)^2 + \frac{c_{45}}{c_{33}} \frac{s_{23}s_{36}}{s_{33}^2} + \frac{1}{4} \frac{c_{55}}{c_{33}} \left( \frac{s_{36}}{s_{33}} \right)^2 \right\} i_x^2 \Big\} c_{33} A = c_2 c_{33} A. \quad (2.20)
\end{aligned}$$

The work  $W$  done by the external force  $f = f(z, t)$  on the axial displacement  $w = w(z, t)$  is as follows

$$W = \int_0^L f(z, t) w(z, t) dz. \quad (2.21)$$

The substitution of equations (2.11), (2.18) and (2.21) into equation (2.9) yields the equation of motion and the associated boundary conditions:

$$C_2 \frac{\partial^4 w}{\partial z^4} - \rho I \frac{\partial^4 w}{\partial z^2 \partial t^2} - C_1 \frac{\partial^2 w}{\partial z^2} + \rho A \frac{\partial^2 w}{\partial t^2} = f, \quad (2.22)$$

$$\left[ C_1 \frac{\partial w}{\partial z} + \rho I \frac{\partial^3 w}{\partial z \partial t^2} - C_2 \frac{\partial^3 w}{\partial z^3} \right] \delta w \Big|_0^L + \left( C_2 \frac{\partial^2 w}{\partial z^2} \right) \delta \left( \frac{\partial w}{\partial z} \right) \Big|_0^L = 0. \quad (2.23)$$

It can be seen from equations (2.7) and (2.8) that

$$w = 0, \quad \frac{\partial w}{\partial z} = 0 \quad (2.24)$$

on an end cross section if it is rigidly fixed. Hence it holds there that

$$\delta w = 0, \quad \delta \left( \frac{\partial w}{\partial z} \right) = 0. \quad (2.25)$$

Since  $\delta w$ , and  $\delta \left( \frac{\partial w}{\partial z} \right)$  are arbitrary on free end cross sections it follows that the stress boundary conditions in terms of  $w = w(z, t)$  on these cross sections assume the form

$$C_1 \frac{\partial w}{\partial z} + \rho I \frac{\partial^3 w}{\partial z \partial t^2} - C_2 \frac{\partial^3 w}{\partial z^3} = 0, \quad (2.26)$$

$$C_2 \frac{\partial^2 w}{\partial z^2} = 0. \quad (2.27)$$

### 3. FREE VIBRATIONS

For free vibrations

$$w(z, t) = W(z) \cos \omega t, \quad f = 0 \quad (3.1)$$

is the solution of (2.22) in which  $W(z)$  is the amplitude of motion and  $\omega$  is the circular frequency of the vibrations. Substitution of solution (3.1) into equation (2.22) yields

$$C_2 \frac{d^4 W}{dz^4} + (\omega^2 \rho I - C_1) \frac{d^2 W}{dz^2} - \omega^2 \rho A W = 0. \quad (3.2)$$

The homogeneous boundary conditions equation (3.2) is associated with are

$$W = 0, \quad \frac{dW}{dz} = 0 \quad (3.3)$$

for fixed-end cross sections,

$$C_1 \frac{dW}{dz} - \omega^2 \rho I \frac{dW}{dz} - C_2 \frac{d^3 W}{dz^3} = 0, \quad \frac{d^2 W}{dz^2} = 0 \quad (3.4)$$

for free-end cross section and

$$W = 0, \quad \frac{d^2 W}{dz^2} = 0 \quad (3.5)$$



for loosely fixed end cross sections [6]

The general solution of equation (3.2), which contains four integration constants, can be written in the form [14, 15]

$$W(z) = K_1 \cosh qz + K_2 \sinh qz + K_3 \cos rz + K_4 \sin rz, \quad (3.6)$$

where the constants  $K_1, K_2, K_3$  and  $K_4$  to be determined from the boundary conditions of the anisotropic bar are such that one of them may have arbitrary value. As regards the parameters  $q$  and  $r$  we have

$$q = \sqrt{\frac{C_1 - \omega^2 \rho I + \sqrt{(C_1 - \omega^2 \rho I)^2 + 4\omega^2 C_2 \rho A}}{2C_2}}, \quad (3.7)$$

$$r = \sqrt{\frac{\sqrt{(C_1 - \omega^2 \rho I)^2 + 4\omega^2 C_2 \rho A} - C_1 + \omega^2 \rho I}{2C_2}}. \quad (3.8)$$

As regards the free bending vibrations of an isotropic Euler-Bernoulli-Rayleigh beam subjected to an axial force, the differential equation and the boundary conditions associated with it are similar to those which describe the longitudinal free vibrations of the anisotropic bar considered in this paper. The differential equation and associated boundary condition for the bending vibrations of an isotropic Euler-Bernoulli beam with constant axial force are as follows [16]:

- differential equation:

$$EI_x \frac{d^4 V}{dz^4} + (\omega^2 \rho J - P) \frac{d^2 V}{dz^2} - \omega^2 \rho A V = 0, \quad (3.9)$$

- boundary conditions for fixed-end cross sections:

$$V = 0, \quad \frac{dV}{dz} = 0, \quad (3.10)$$

- boundary conditions for free-end cross sections:

$$P \frac{dV}{dz} - EI_x \frac{d^3 V}{dz^3} - \rho \omega^2 J \frac{dV}{dz} = 0, \quad \frac{d^2 V}{dz^2} = 0, \quad (3.11)$$

- boundary conditions for simply supported end cross sections:

$$V = 0, \quad \frac{d^2 V}{dz^2} = 0. \quad (3.12)$$

In equations (3.9)-(3.12)  $V = V(z)$  is the amplitude of the displacement of center-line in the direction of axes  $y$ ,  $E$  is the Young modulus,  $J = I_x + I_y$ ,  $P > 0$  is the applied axial force. The form of equations (3.9)-(3.12) makes it possible to establish an analogy between the longitudinal vibration of anisotropic bar and the bending vibration of the isotropic Euler-Bernoulli-Rayleigh beam subjected to constant positive axial force. The analogy is shown in Table 1.

Table 1. Analogous quantities and boundary conditions.

Longitudinal vibrations of anisotropic bars	Bending vibrations of isotropic beams
$W = W(z)$ $C_2$ $C_1$ $I$	$V = V(z)$ $EI_x$ $P > 0$ $J$
Boundary conditions	Boundary conditions
fixed end: $W = 0, \frac{dW}{dz} = 0$ free end: $(C_1 - \omega^2 \rho I) \frac{dW}{dz} - C_2 \frac{d^3 W}{dz^3} = 0, \frac{d^2 W}{dz^2} = 0$ loosely fixed end: $W = 0, \frac{d^2 W}{dz^2} = 0$	fixed end: $V = 0, \frac{dV}{dz} = 0$ free end: $(P - \omega^2 \rho J) \frac{dV}{dz} - EI_x \frac{d^3 V}{dz^3} = 0, \frac{d^2 V}{dz^2} = 0$ simply supported end: $V = 0, \frac{d^2 V}{dz^2} = 0$

## 4. EXAMPLE

Assume that the anisotropic bar is fixed loosely at both ends. Then the axial displacement and shear strains will be zero at each end of the bar. Hence

$$W = 0, \quad \frac{d^2 W}{dz^2} = 0, \quad \text{at } z = 0 \quad \text{and} \quad z = L. \quad (4.1)$$

It is obvious from taking the analogy formulated in Table 1 into account that the boundary conditions related to the loosely fixed end condition of the anisotropic bar are similar to those valid for the simply supported end conditions of the vibrating Euler-Bernoulli-Rayleigh beam. On the basis of this similarity we shall assume

$$W_j(z) = W_j \sin j \frac{\pi}{L} z, \quad j = 1, 2, \dots \quad (4.2)$$

The function given by equation (4.2) satisfies the boundary conditions for any value of  $W_j$  ( $j = 1, 2, \dots$ )

$$W(0) = W(L) = 0, \quad \frac{d^2 W}{dz^2} \Big|_{z=0} = \frac{d^2 W}{dz^2} \Big|_{z=L} = 0. \quad (4.3)$$

From equation (3.2) it follows that the natural frequencies of the longitudinal vibration of anisotropic bar fixed loosely at both ends are expressed as

$$\omega_j^2 = \frac{C_2 \left(\frac{j\pi}{L}\right)^4 + C_1 \left(\frac{j\pi}{L}\right)^2}{\rho \left(\frac{j\pi}{L}\right)^2 I + A\rho} = \frac{c_2 \left(\frac{j\pi}{L}\right)^2 + c_1}{i^2 \left(\frac{j\pi}{L}\right)^2 + 1} \Omega_j^2, \quad \Omega_j = \sqrt{\frac{c_{33}}{\rho}} \frac{j\pi}{L} \quad j = 1, 2, \dots \quad (4.4)$$

In equation (4.4)  $\Omega_j$  ( $j = 1, 2, 3, \dots$ ) is the natural frequency of the longitudinal vibration of the considered bar with fixed ends, which can be derived by the application of the following assumptions (simple theory):

- The lateral displacement  $u$  and  $v$  are neglected and  $w = w(z, t)$ .
- The dominant element of the stiffness matrix  $\mathbf{C}$  is  $c_{33}$ , so the expression of axial force  $N$  can be written in the form

$$N = A c_{33} \frac{\partial w}{\partial z}. \quad (4.5)$$

This formulation does not introduce the effect of lateral motions of cross sections and the material anisotropy. The eigenfunction (mode shape) corresponding to the frequency  $\omega_j$  is given by equation (4.2).

##### 5. DEPENDENCE OF THE NATURAL FREQUENCIES ON THE POSITION OF THE PRINCIPAL MATERIAL COORDINATE SYSTEM

We consider an orthotropic material whose principal directions are  $x_1$ ,  $x_2$  and  $x_3 = z$  [12, 13, 17, 18]. The position of the material coordinate system  $Ox_1x_2x_3$  is given by angle  $\alpha$  as shown in Figure 2 [17, 18].

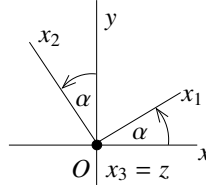


Figure 2. Definition of  $\alpha$

For orthotropic elastic material in terms of engineering constants  $E_1$ ,  $E_2$ ,  $E_3$ ,  $G_{23}$ ,  $G_{13}$ ,  $G_{12}$ ,  $\nu_{12}$ ,  $\nu_{21}$ ,  $\nu_{13}$ ,  $\nu_{31}$ ,  $\nu_{23}$ ,  $\nu_{32}$  the stiffness matrix  $\mathbf{C}(x_1, x_2, x_3)$  can be written in the form [17, 18]

$$\mathbf{C}(x_1, x_2, x_3) = \begin{bmatrix} C_{11} & C_{12} & C_{13} & 0 & 0 & 0 \\ C_{12} & C_{22} & C_{23} & 0 & 0 & 0 \\ C_{13} & C_{23} & C_{33} & 0 & 0 & 0 \\ 0 & 0 & 0 & C_{44} & 0 & 0 \\ 0 & 0 & 0 & 0 & C_{55} & 0 \\ 0 & 0 & 0 & 0 & 0 & C_{66} \end{bmatrix} = \begin{bmatrix} \frac{1-\nu_{23}\nu_{32}}{E_2 E_3 \Delta} & \frac{\nu_{21}+\nu_{23}\nu_{31}}{E_2 E_3 \Delta} & \frac{\nu_{31}+\nu_{21}\nu_{32}}{E_2 E_3 \Delta} & 0 & 0 & 0 \\ \frac{\nu_{21}+\nu_{23}\nu_{31}}{E_2 E_3 \Delta} & \frac{1-\nu_{13}\nu_{31}}{E_1 E_3 \Delta} & \frac{\nu_{32}+\nu_{12}\nu_{31}}{E_1 E_3 \Delta} & 0 & 0 & 0 \\ \frac{\nu_{31}+\nu_{21}\nu_{32}}{E_2 E_3 \Delta} & \frac{\nu_{32}+\nu_{12}\nu_{31}}{E_1 E_3 \Delta} & \frac{1-\nu_{12}\nu_{21}}{E_1 E_2 \Delta} & 0 & 0 & 0 \\ 0 & 0 & 0 & G_{23} & 0 & 0 \\ 0 & 0 & 0 & 0 & G_{13} & 0 \\ 0 & 0 & 0 & 0 & 0 & G_{12} \end{bmatrix}, \quad (5.1)$$

where

$$E_1 \nu_{21} = E_2 \nu_{12}, \quad E_2 \nu_{32} = E_3 \nu_{23}, \quad E_1 \nu_{31} = E_3 \nu_{13}, \quad (5.2)$$

and

$$\Delta = \frac{1 - \nu_{12}\nu_{21} - \nu_{23}\nu_{32} - \nu_{13}\nu_{31} - 2\nu_{21}\nu_{32}\nu_{13}}{E_1 E_2 E_3}. \quad (5.3)$$

The inverse of  $\mathbf{C}(x_1, x_2, x_3)$  gives the flexibility matrix  $\mathbf{S}(x_1, x_2, x_3)$  defined in the principal material coordinate system  $Ox_1x_2x_3$  [17, 18]:

$$\mathbf{S}(x_1, x_2, x_3) = \begin{bmatrix} S_{11} & S_{12} & S_{13} & 0 & 0 & 0 \\ S_{12} & S_{22} & S_{23} & 0 & 0 & 0 \\ S_{13} & S_{23} & S_{33} & 0 & 0 & 0 \\ 0 & 0 & 0 & S_{44} & 0 & 0 \\ 0 & 0 & 0 & 0 & S_{55} & 0 \\ 0 & 0 & 0 & 0 & 0 & S_{66} \end{bmatrix} = \begin{bmatrix} \frac{1}{E_1} & -\frac{\nu_{21}}{E_2} & -\frac{\nu_{31}}{E_3} & 0 & 0 & 0 \\ -\frac{\nu_{12}}{E_1} & \frac{1}{E_2} & -\frac{\nu_{32}}{E_3} & 0 & 0 & 0 \\ -\frac{\nu_{13}}{E_1} & -\frac{\nu_{23}}{E_2} & \frac{1}{E_3} & 0 & 0 & 0 \\ 0 & 0 & 0 & \frac{1}{G_{23}} & 0 & 0 \\ 0 & 0 & 0 & 0 & \frac{1}{G_{13}} & 0 \\ 0 & 0 & 0 & 0 & 0 & \frac{1}{G_{12}} \end{bmatrix}. \quad (5.4)$$

By the use of transformation stiffness and compliance matrices [17, 18] we can derive the formulas of  $c_{ij}$  in terms of  $C_{ij}$  and the formulas of  $s_{ij}$  in terms of  $S_{ij}$ :

$$c_{11} = m^4 C_{11} + 2m^2 n^2 (C_{12} + 2C_{66}) + n^4 C_{22}, \quad (5.5)$$

$$c_{12} = m^2 n^2 (C_{11} + C_{22} - 4C_{66}) + (m^4 + n^4) C_{12}, \quad (5.6)$$

$$c_{13} = m^2 C_{13} + n^2 C_{23}, \quad (5.7)$$

$$c_{16} = mn [m^2 (C_{11} - C_{12} - 2C_{66}) + n^2 (C_{12} - C_{22} + 2C_{66})], \quad (5.8)$$

$$c_{22} = n^4 C_{11} + 2m^2 n^2 (C_{12} + 2C_{66}) + m^4 C_{22}, \quad (5.9)$$

$$c_{23} = n^2 C_{13} + m^2 C_{23}, \quad (5.10)$$

$$c_{26} = mn [n^2 (C_{11} - C_{12} - 2C_{66}) + m^2 (C_{12} - C_{22} + 2C_{66})], \quad (5.11)$$

$$c_{33} = C_{33}, \quad (5.12)$$

$$c_{36} = mn (C_{13} - C_{23}), \quad (5.13)$$

$$c_{44} = m^2 C_{44} + n^2 C_{55}, \quad (5.14)$$

$$c_{45} = mn (C_{55} - C_{44}), \quad (5.15)$$

$$c_{55} = n^2 C_{44} + m^2 C_{55}, \quad (5.16)$$

$$c_{66} = m^2 n^2 (C_{11} - 2C_{12} + C_{22}) + (n^2 - m^2)^2 C_{66} \quad (5.17)$$

$$c_{14} = c_{15} = c_{24} = c_{25} = c_{34} = c_{35} = c_{46} = c_{56} = 0, \quad (5.18)$$

$$s_{11} = m^4 S_{11} + m^2 n^2 (2S_{12} + S_{66}) + n^2 S_{22}, \quad (5.19)$$

$$s_{12} = m^2 n^2 (S_{11} + S_{22} - S_{66}) + (m^4 + n^4) S_{12}, \quad (5.20)$$

$$s_{13} = m^2 S_{13} + n^2 S_{23}, \quad (5.21)$$

$$s_{16} = mn [m^2 (2S_{11} - 2S_{12} - S_{66}) + n^2 (2S_{12} - 2S_{22} + S_{66})], \quad (5.22)$$

$$s_{22} = n^4 S_{11} + m^2 n^2 (2S_{12} + S_{66}) + m^4 S_{22}, \quad (5.23)$$

$$s_{23} = n^2 S_{13} + m^2 S_{23}, \quad (5.24)$$

$$s_{26} = mn [n^2 (2S_{11} - 2S_{12} - S_{66}) + m^2 (2S_{12} - 2S_{22} + S_{66})], \quad (5.25)$$

$$s_{33} = S_{33}, \quad (5.26)$$

$$s_{36} = 2mn (S_{13} - S_{23}), \quad (5.27)$$

$$s_{44} = m^2 S_{44} + n^2 S_{55}, \quad (5.28)$$

$$s_{45} = mn (S_{55} - S_{44}), \quad (5.29)$$

$$s_{55} = n^2 S_{44} + m^2 S_{55}, \quad (5.30)$$

$$s_{66} = 4m^2 n^2 (S_{11} - 2S_{12} + S_{22}) + (n^2 - m^2) S_{66}, \quad (5.31)$$

$$s_{14} = s_{15} = s_{24} = s_{25} = s_{34} = s_{35} = s_{46} = s_{56} = 0, \quad (5.32)$$

$$m = \cos \alpha, \quad n = \sin \alpha. \quad (5.33)$$

The dependence of the natural frequencies on  $\alpha$  given by equation (4.4) for an orthotropic bar of rectangular cross section is analyzed by using the following data (Figure 3):

$$b_1 = 0.03 \text{ m}, \quad b_2 = 0.05 \text{ m}, \quad L = 1 \text{ m}, \quad \rho = 550 \frac{\text{kg}}{\text{m}^3},$$

$$E_1 = 11 \cdot 10^8 \text{ Pa}, \quad E_2 = 5.7 \cdot 10^8 \text{ Pa}, \quad E_3 = 163 \cdot 10^8 \text{ Pa},$$

$$G_{23} = 11.06 \cdot 10^8 \text{ Pa}, \quad G_{13} = 6.8 \cdot 10^8 \text{ Pa}, \quad G_{12} = 0.66 \text{ Pa},$$

$$\nu_{12} = 0.68, \quad \nu_{13} = 0.038, \quad \nu_{23} = 0.015.$$

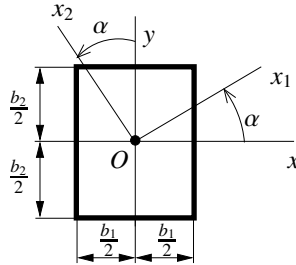
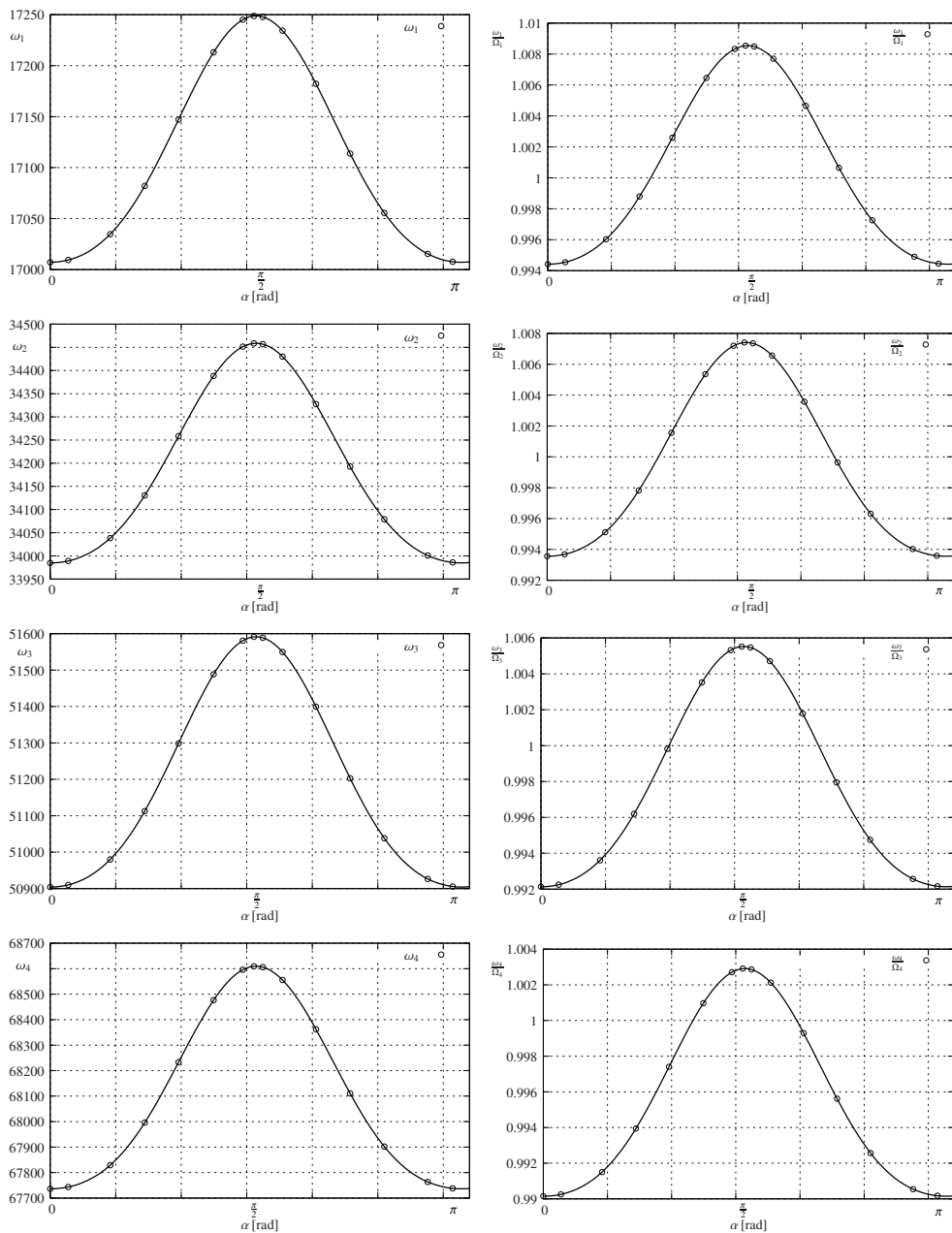


Figure 3. Solid rectangular cross section

In the present problem  $\Omega_1 = 17\,102.6\,1/\text{s}$ ,  $\Omega_2 = 34\,205.2\,1/\text{s}$ ,  $\Omega_3 = 51\,307.8\,1/\text{s}$ ,  $\Omega_4 = 68\,410.4\,1/\text{s}$ , which do not depend on the size or the shape of the cross section. The graphs of  $\omega_j(\alpha)$  and  $\omega_j(\alpha)/\Omega_j$  for  $j = 1, 2, 3, 4$  and  $0 \leq \alpha \leq \pi$  are shown in Figure 4.

Figure 4.  $\alpha$  dependence of the natural frequencies for  $j = 1, 2, 3, 4$

In Table 2 the  $\alpha$  dependence of the fundamental frequency obtained from equation (4.4) is compared to the results of FEM computations for  $\alpha = 0, \frac{\pi}{8}, \frac{\pi}{6}, \frac{\pi}{4}, \frac{\pi}{3}, \frac{\pi}{2}$ .

Table 2. Comparison of analytical and FEM (Abaqus) solutions

$\omega_1(\alpha) \left[ \frac{\text{rad}}{\text{s}} \right]$		
$\alpha$	Analytical Solution	FEM Computation
0	17 007.13	17 094
$\pi/8$	17 026.93	17 094
$\pi/6$	17 044.19	17 094
$\pi/4$	17 096.92	17 093
$\pi/3$	17 165.18	17 093
$\pi/2$	17 248.79	17 092

The results of analytical solution and FEM computations for the first four natural frequencies for  $\alpha = 0$  are listed in Table 3.

Table 3. Comparison of analytical and FEM (Abaqus) solutions for  $\alpha = 0$

$\omega_j(0) \left[ \frac{\text{rad}}{\text{s}} \right]$		
$j$	Analytical Solution	FEM Computation
1	17 007.13	17 094
2	33 988.48	34 130
3	50 904.12	50 912
4	67 736.28	68 191

The results obtained from FEM computations support the validity of the presented approximate analytical method.

## 6. CONCLUSIONS

In this paper an approximate theory of the longitudinal vibration of anisotropic elastic bars is presented. The equation of motion and the associated boundary conditions are derived by the application of Hamilton's principle. The developed theory is a Rayleigh-Bishop type model of the longitudinal vibration. An analogy is formulated between the longitudinal vibration of an anisotropic bar and the bending vibration of an isotropic Euler-Bernoulli-Rayleigh beam subjected to constant axial force.

For an orthotropic elastic bar the connection between the position of material coordinate system, which is given by an angle coordinate, and the eigenfrequencies is

analyzed. Obtained numerical results for some values of eigenfrequencies by the application of the approximate analytical method are checked by FEM (Abaqus) computations. Presented numerical results show that the eigenfrequencies of the longitudinal free vibrations slightly depend on the position of principal axes of orthotropy.

**Acknowledgement.** The described study was carried out as part of the EFOP-3.6.1-16-2016-00011 "Younger and Renewing University – Innovative Knowledge City – institutional development of the University of Miskolc aiming at intelligent specialisation" project implemented in the framework of the Szechenyi 2020 program. The realization of this project is supported by the European Union, co-financed by the European Social Fund and supported by the National Research, Development and Innovation Office – NKFIH, K115701.

#### REFERENCES

1. A. E. H. Love. *A Treatise on the Mathematical Theory of Elasticity*. 4th ed. Dover, New York, 1944. URL: <https://hal.archives-ouvertes.fr/hal-01307751/document>.
2. J. W. Rayleigh. *Theory of Sound*. Dover, New York, 1945.
3. S. P. Timoshenko, D. H. Young, and W. Weaver. *Vibration Problems in Engineering*. 4th. ed. Wiley, New York, 1974.
4. J. S. Rao. *Advanced Theory of Vibration*. Wiley Eastern Limited, New Delhi, 1992. URL: <https://books.google.hu/books?id=ComyQgAACAAJ>.
5. S. S. Rao. *Mechanical Vibrations*. 4th. ed. Prentice Hall, Upper Saddle River, NJ., 2004.
6. S. S. Rao. *Vibration of Continuous System*. New Jersey, John Wiley, 2007.
7. R. E. D. Bishop. "Longitudinal waves in beams." *Aeronautical Quarterly*, **3**(2), (1952), pp. 280–293. DOI: 10.1017/S0001925900000706.
8. M. Shatalov, I. Fedotov, H. M. Tenkam, and J. Marais. "Comparison of classical and modern theories of longitudinal wave propagation in elastic rods." *The Sixteenth International Congress on Sound and Vibration*. Krakow. 2009. URL: <http://hdl.handle.net/10204/3629>.
9. I. Fedotov, T. Fedotova, M. Shatalov, and H. M. Tenkam. "Application of eigenfunction orthogonalities to vibration problems." *Proceedings of the World Congress on Engineering*. London UK., 2009.
10. M. Shatalov, J. Marais, I. Fedotov, and H. M. Tenkam. "Longitudinal vibration of isotropic solid rods: From classical to modern theories." *Advances in Computer Science and Engineering*, Ch.10 (2011), pp. 1–28. URL: <http://hdl.handle.net/10204/5739>.
11. L. Meirovitch. *Fundamentals of Vibrations*. McGraw-Hill, New York, 2001. URL: <https://www.amazon.com/Fundamentals-Vibrations-Leonard-Meirovitch/dp/1577666917>.
12. S. G. Lekhnitskii. *Theory of Elasticity of an Anisotropic Body*. Mir Publishers, 1981. DOI: 10.1137/1009023.
13. J. D. Renton. *Elastic Beams and Frames*. Camford Books, Norfolk, 2000.
14. L. Elsgolts. *Differential Equations and Calculus of Variations*. University Press of the Pacific, 2003. URL: <https://books.google.hu/books?id=ZwIyAAAACAAJ>.



15. E. J. R. Charles. *Ordinary Differential Equations. Applications, Models and Computing*. CRC Press, Boca Ranton, 2010. URL: <https://www.crcpress.com/Ordinary-Differential-Equations-Applications-Models-and-Computing/Roberts/p/book/9781138118218>.
16. L. Meirovitch. *Principle and Techniques of Vibrations*. Prentice Hall, New Jersey, 1997. URL: <https://www.pearson.com/us/higher-education/program/Meirovitch-Principles-and-Techniques-of-Vibrations/PGM272917.html>.
17. C. T. Herakovich. *Mechanics of Fibrous Composites*. John Wiley & Sons, Inc., 1998. DOI: 10.1007/978-94-011-3670-9.
18. H. Altenbach, J. Altenbach, and W. Kissing. *Mechanics of Composite Structural Elements*. Springer-Verlag Berlin, 2004. DOI: 10.1007/978-3-662-08589-9.



## ANALYSIS OF A CURVED BIMETALLIC BEAM

DÁVID GÖNCZI

Institute of Applied Mechanics, University of Miskolc

H-3515 Miskolc-Egyetemváros, Hungary

[mechgoda@uni-miskolc.hu](mailto:mechgoda@uni-miskolc.hu)

[Received: December 12, 2018; Accepted: April 26, 2019]

**Abstract.** This paper deals with the determination of stresses and displacements in a curved bimetallic beam which has uniform curvature. The two curved beam components of different materials have common displacements at their interface. The thermal load is derived from uniform temperature change. Two models are considered. The first one is based on the theory of the generalized plane stress state of elasticity and the second one uses a strength of materials approach. The results obtained by these models are verified by a comparison with finite element analysis.

*Mathematical Subject Classification:* 74B05, 34B05

*Keywords:* Bimetallic, curved beam, uniform temperature change, stresses, displacement, FEM

### 1. INTRODUCTION

When two metal strips, strip 1 and strip 2, are bounded along the length of a beam, strip 1 is partly prevented from expanding by strip 2 when they are subjected to uniform temperature change. A considerable force is thereby developed which causes the bonded strip to bend. If there are no applied external forces, the bimetallic strip will take the shape of a circular arc. Timoshenko [1] was the first who studied stresses in bimetallic beams. He used the expressions of curvature and stresses assuming that the temperature change is uniform [1–3]. Several works have dealt with the analysis of bimetallic strips which consist of two different beam components [4–10]. In the above-mentioned papers curved bimetallic beams were not considered. In papers [11, 12] curved beams are investigated but the loading is pure mechanical loading. In this paper the curved bimetallic beam under the action of uniform temperature change is studied. The considered bimetallic beam has uniform curvature. To determine the deformations and stresses in curved bimetallic beams two methods will be considered. The first one is an elasticity solution based on the theory of generalized plane stress state. The second approach uses a strength of materials formulation. The results obtained by these models are verified by comparison with a finite element solution (Abaqus CAE).

## 2. SOLUTION AS A GENERALIZED PLANE STRESS PROBLEM

Figure 1 shows the curved bimetallic beam of uniform curvature, which consists of two different elastic materials.

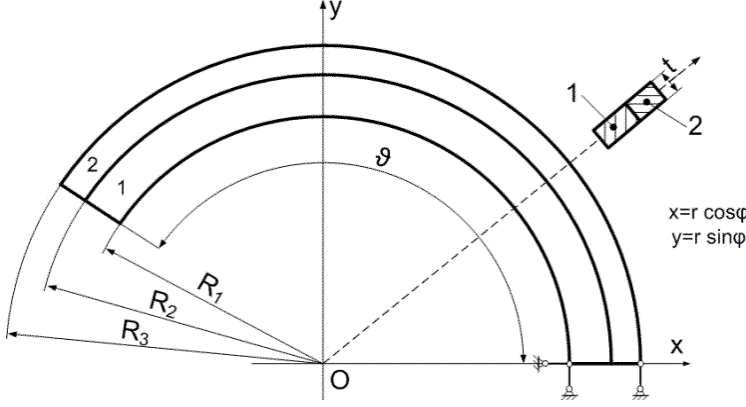


Figure 1. Bimetallic curved beam with rectangular cross section

The governing equations and boundary conditions are formulated in the cylindrical coordinate system  $Or\varphi z$ , and the plane  $z = 0$  is the symmetry plane of the two-layered curved beam for its geometrical properties. The connection between beam component 1 and beam component 2 at the common cylindrical boundary surface  $r = R_2$  is perfect, hence neither the displacements nor the tractions have a jump at  $r = R_2$ . For example, technically the rigid connection between the beams 1 and 2 is created by welded bonds. There are no present body forces and the whole boundary of the bimetallic curved beam is stress free. This means that

$$\sigma_r(R_1, \varphi) = \sigma_r(R_3, \varphi) = \tau_{r\varphi}(R_1, \varphi) = \tau_{r\varphi}(R_3, \varphi) = 0, \quad 0 \leq \varphi \leq \vartheta, \quad (1)$$

$$\sigma_\varphi(r, \vartheta) = \sigma_\varphi(r, 0) = \tau_{r\varphi}(r, \vartheta) = \tau_{r\varphi}(r, 0) = 0, \quad R_1 \leq r \leq R_3. \quad (2)$$

In the framework of generalized plane stress model the boundary condition

$$\sigma_\varphi(r, \vartheta) = \sigma_\varphi(r, 0) = 0, \quad R_1 \leq r \leq R_3, \quad (3)$$

will be satisfied only in weak form such as

$$N = \int_{R_1}^{R_3} \sigma_\varphi(r, \vartheta) dr = \int_{R_1}^{R_3} \sigma_\varphi(r, 0) dr = 0, \quad (4)$$

$$M = \int_{R_1}^{R_3} r \sigma_\varphi(r, \vartheta) dr = \int_{R_1}^{R_3} r \sigma_\varphi(r, 0) dr = 0. \quad (5)$$

That is, the stress resultants and the moment resultant of the stresses vanish only at the end cross sections  $\varphi = 0$  and  $\varphi = \vartheta$ . The temperature of the two-layer composite beam initially is the reference temperature. Its temperature is slowly raised to a

constant uniform temperature, where the temperature change is  $T$ . The deformations and stresses are caused by only the uniform change of temperature. The solution of this problem is derived from the following displacement field

$$u_i(r, \varphi) = U_i(r) + f_1 \cos \varphi + f_2 \sin \varphi, \quad (i = 1, 2), \quad (6)$$

$$v_i(r, \varphi) = Cr\varphi + f_1 \sin \varphi - f_2 \cos \varphi + f_3 r, \quad (i = 1, 2), \quad (7)$$

where the displacement components are denoted by  $u_i$  in the radial direction and by  $v_i$  in the circumferential direction and the lower index  $i$  refers to curved beam component ( $i = 1, 2$ ). In equations (6), (7)  $f_1$ ,  $f_2$  and  $f_3$  are integration constants whose values can be obtained from the displacement boundary conditions (Figure 1):

$$u_1(R_1, 0) = 0, \quad v_1(R_1, 0) = 0, \quad v_2(R_3, 0) = 0. \quad (8)$$

The constant  $C$  can be determined from the stress boundary conditions (1), (4), (5) and the continuity conditions the displacements and the normal stress field should satisfy on the common cylindrical boundary of the beam components 1 and 2. It follows from equations (6) and (7) that the strains can be given in terms of  $U_i$  and  $C$  as

$$\varepsilon_{\varphi i} = \frac{U_i}{r} + C, \quad \varepsilon_{ri} = \frac{dU_i}{dr}, \quad (i = 1, 2). \quad (9)$$

Combining equations (9)<sub>1</sub> and (9)<sub>2</sub> yields the compatibility condition the strains should meet:

$$r \frac{d\varepsilon_{\varphi i}}{dr} + \varepsilon_{\varphi i} - \varepsilon_{ri} - C = 0, \quad (i = 1, 2). \quad (10)$$

For the present problem the constitutive law of linear thermoelasticity has the following form [9, 10]:

$$E_i \varepsilon_{ri} = \sigma_{ri} - \nu_i \sigma_{\varphi i} + E_i \alpha_i T, \quad (i = 1, 2), \quad (11)$$

$$E_i \varepsilon_{\varphi i} = \sigma_{\varphi i} - \nu_i \sigma_{ri} + E_i \alpha_i T, \quad (i = 1, 2), \quad (12)$$

where  $E_i$  is the modulus of elasticity,  $\nu_i$  is the Poisson ratio and  $\alpha_i$  is the coefficient of linear thermal expansion while the radial and circumferential normal stresses are denoted by  $\sigma_{ri}$  and  $\sigma_{\varphi i}$  ( $i = 1, 2$ ). Substituting equations (11) and (12) into (10) yields

$$r \frac{d}{dr} (-\nu_i \sigma_{ri} + \sigma_{\varphi i} + E_i \alpha_i T) - (1 + \nu_i) \sigma_{ri} + (1 + \nu_i) \sigma_{\varphi i} - E_i C = 0, \quad (i = 1, 2). \quad (13)$$

In our case the equation of mechanical equilibrium is as follows:

$$\frac{d\sigma_{ri}}{dr} + \frac{\sigma_{ri} - \sigma_{\varphi i}}{r} = 0, \quad (i = 1, 2). \quad (14)$$

The general solution of equation (14) can be given in terms of the stress functions  $F_i = F_i(r)$  as

$$\sigma_{ri} = \frac{F_i(r)}{r}, \quad \sigma_{\varphi i} = \frac{dF_i}{dr}, \quad (i = 1, 2). \quad (15)$$

Combination of equation (13) with the formulas derived for the normal stresses leads to the following differential equations

$$r^2 \frac{d^2 F_i}{dr^2} + r \frac{dF_i}{dr} - F_i - E_i C r = 0, \quad (i = 1, 2), \quad (16)$$

the solution of which are given by

$$F_1(r) = c_1 r + \frac{c_2}{r} + \frac{E_1 C}{2} r \ln r, \quad R_1 \leq r < R_2, \quad (17)$$

and

$$F_2(r) = c_3 r + \frac{c_4}{r} + \frac{E_2 C}{2} r \ln r, \quad R_2 < r \leq R_3, \quad (18)$$

where  $c_1$ ,  $c_2$ ,  $c_3$  and  $c_4$  are undetermined integration constants. Note that the stress and strain fields are independent of the polar angle  $\varphi$ . A simple calculation shows that

$$\begin{aligned} N &= \int_{R_1}^{R_3} \sigma_\varphi(r) dr = \int_{R_1}^{R_3} \frac{d}{dr} (r \sigma_r) dr = \\ &= R_2 \sigma_{r1}(R_2) - R_1 \sigma_{r1}(R_1) + R_3 \sigma_{r2}(R_3) - R_2 \sigma_{r2}(R_2) = 0 \end{aligned} \quad (19)$$

if the stress boundary conditions

$$\sigma_{r1}(R_1) = \sigma_{r2}(R_3) = 0 \quad (20)$$

and the continuity conditions

$$\sigma_{r1}(R_2) = \sigma_{r2}(R_2) \quad (21)$$

are satisfied. To obtain the stress field we should determine the five undetermined integration constants  $c_1$ ,  $c_2$ ,  $c_3$ ,  $c_4$  and  $C$ . The following equations will be used for determining the values of the unknown integration constants:

$$\sigma_{r1}(R_1) = 0, \quad \sigma_{r2}(R_3) = 0, \quad \sigma_{r1}(R_2) = \sigma_{r2}(R_2), \quad (22)$$

$$U_1(R_2) = U_2(R_2), \quad \int_{R_1}^{R_2} r \sigma_{\varphi 1} dr + \int_{R_2}^{R_3} r \sigma_{\varphi 2} dr = 0. \quad (23)$$

By the use of (9)<sub>1</sub> equation (23)<sub>1</sub> can be manipulated into the following form:

$$\varepsilon_{\varphi 1}(R_2) = \varepsilon_{\varphi 2}(R_2). \quad (24)$$

This equation can be expressed in terms of stresses as

$$\frac{1}{E_1} [\sigma_{\varphi 1}(R_2) - \nu_1 \sigma_{r1}(R_2)] + \alpha_1 T = \frac{1}{E_2} [\sigma_{\varphi 2}(R_2) - \nu_2 \sigma_{r2}(R_2)] + \alpha_2 T. \quad (25)$$

By utilizing equations (22), (23) and (25) the following system of linear equations can be set up for  $\mathbf{x}^T = [c_1 \mid c_2 \mid c_3 \mid c_4 \mid C]$ :

$$\mathbf{M} \mathbf{x} = \mathbf{h} \quad (26)$$

where

$$\mathbf{M}_{(5 \times 5)} = [m_{ij}]; \quad \mathbf{h}^T = [0 \mid 0 \mid 0 \mid h \mid 0] \quad (27)$$

and

$$\left. \begin{aligned}
m_{11} = R_1, \quad m_{12} = \frac{1}{R_1}, \quad m_{13} = m_{14} = m_{21} = m_{22} = 0, \quad m_{15} = \frac{E_1}{2} R_1 \ln R_1 \\
m_{23} = R_3, \quad m_{24} = \frac{1}{R_3}, \quad m_{25} = \frac{E_2}{2} R_3 \ln R_3, \\
m_{31} = R_2, \quad m_{32} = \frac{1}{R_2}, \quad m_{33} = -R_2, \quad m_{34} = -\frac{1}{R_2}, \quad m_{35} = \frac{E_1 - E_2}{2} R_2 \ln R_2, \\
m_{41} = \frac{1 - \nu_1}{E_1}, \quad m_{42} = -\frac{1 + \nu_1}{E_1 R_2^2}, \quad m_{43} = -\frac{1 - \nu_2}{E_2}, \\
m_{44} = \frac{1 + \nu_2}{E_2 R_2^2}, \quad m_{45} = \frac{\nu_2 - \nu_1}{2} \ln R_2, \\
m_{51} = \frac{1}{2} (R_2^2 - R_1^2), \quad m_{52} = -\ln \frac{R_2}{R_1}, \quad m_{53} = \frac{1}{2} (R_3^2 - R_2^2), \\
m_{54} = -\ln \frac{R_3}{R_2}, \quad h = (\alpha_2 - \alpha_1) T, \\
m_{55} = \frac{E_1}{4} \left[ R_2^2 \ln R_2 - R_1^2 \ln R_1 + \frac{1}{2} (R_2^2 - R_1^2) \right] + \\
+ \frac{E_2}{4} \left[ R_3^2 \ln R_3 - R_2^2 \ln R_2 + \frac{1}{2} (R_3^2 - R_2^2) \right].
\end{aligned} \right\} \quad (28)$$

After solving the linear equation system (26) the following formulas can be used for computing the stresses and displacements:

$$\sigma_{r1}(r) = c_1 + \frac{c_2}{r^2} + \frac{E_1 C}{2} \ln r, \quad \sigma_{\varphi 1}(r) = c_1 - \frac{c_2}{r^2} + \frac{E_1 C}{2} (\ln r + 1), \quad (29)$$

$$\sigma_{r2}(r) = c_2 + \frac{c_3}{r^2} + \frac{E_2 C}{2} \ln r, \quad \sigma_{\varphi 2}(r) = c_3 - \frac{c_4}{r^2} + \frac{E_2 C}{2} (\ln r + 1), \quad (30)$$

$$U_1(r) = \frac{1 - \nu_1}{E_1} c_1 r - \frac{1 + \nu_1}{r E_1} c_2 + \frac{C r}{2} [(1 - \nu_1) \ln r - 1] + \alpha_1 T r, \quad (31)$$

$$U_2(r) = \frac{1 - \nu_2}{E_2} c_3 r - \frac{1 + \nu_2}{r E_2} c_4 + \frac{C r}{2} [(1 - \nu_2) \ln r - 1] + \alpha_2 T r, \quad (32)$$

$$\begin{aligned}
f_1 = -U_1(R_1) = -\frac{1 - \nu_1}{E_1} c_1 R_1 + \frac{1 + \nu_1}{R_1 E_1} c_2 - \\
- \frac{C R_1}{2} [(1 - \nu_1) \ln R_1 - 1] + \alpha_1 T R_1
\end{aligned} \quad (33a)$$

$$f_2 = f_3 = 0, \quad (33b)$$

$$u_i(r) = U_i(r) - U_1(R_1) \cos \varphi, \quad (i = 1, 2), \quad (34)$$

$$v_i(r) = C r \varphi + U_1(R_1) \sin \varphi, \quad (i = 1, 2). \quad (35)$$

### 3. SOLUTION IN THE FRAMEWORK OF STRENGTH OF MATERIALS

On the basis of paper [13] by Ecsedi and Dluli it will be assumed that

$$u = U(\varphi) \quad \text{and} \quad v = r\phi(\varphi) + \frac{dU}{d\varphi} \quad (36)$$

are the two displacement components for the whole two-layer composite curved beam. The strain-displacement relationships of the linearized theory of elasticity yield

$$\varepsilon_r = \varepsilon_z = \gamma_{r\varphi} = \gamma_{\varphi z} = \gamma_{rz} = 0, \quad (37)$$

$$\varepsilon_\varphi = \frac{1}{r} \left( U + \frac{d^2U}{d\varphi^2} \right) + \frac{d\phi}{d\varphi} \quad (38)$$

which means that only one strain component is different from zero. Equations (37) and (38) show that the displacements given by (36) satisfy the requirements of Euler-Bernoulli beam theory. The constitutive relation is the simple Hook's law applied here by taking into account the thermal effect:

$$\sigma_{\varphi i} = E_i \varepsilon_\varphi - E_i \alpha_i T = \frac{E_i}{r} \left( U + \frac{d^2U}{d\varphi^2} \right) + E_i \frac{d\phi}{d\varphi} - E_i \alpha_i T, \quad (i = 1, 2). \quad (39)$$

The stress resultant and the moment resultant of the stresses (the axial force and the bending moment) vanish since there is no mechanical load on the structure (Figure 2). Hence

$$N = \int_{R_1}^{R_3} \sigma_\varphi dr = k_1 \left( U + \frac{d^2U}{d\varphi^2} \right) + k_2 \frac{d\phi}{d\varphi} - \beta T = 0, \quad (40)$$

$$M = \int_{R_1}^{R_3} r \sigma_\varphi dr = k_2 \left( U + \frac{d^2U}{d\varphi^2} \right) + k_3 \frac{d\phi}{d\varphi} - \gamma T = 0. \quad (41)$$

where

$$\left. \begin{aligned} k_1 &= E_1 \ln \frac{R_2}{R_1} + E_2 \ln \frac{R_3}{R_2}, & k_2 &= E_1 (R_2 - R_1) + E_2 (R_3 - R_2), \\ k_3 &= \frac{E_1}{2} (R_2^2 - R_1^2) + \frac{E_2}{2} (R_3^2 - R_2^2), \end{aligned} \right\} \quad (42)$$

$$\left. \begin{aligned} \beta &= \alpha_1 E_1 (R_2 - R_1) + \alpha_2 E_2 (R_3 - R_2), \\ \gamma &= \frac{\alpha_1 E_1}{2} (R_2^2 - R_1^2) + \frac{\alpha_2 E_2}{2} (R_3^2 - R_1^2) \end{aligned} \right\} \quad (43)$$

It follows from equations (40) and (42) that

$$U + \frac{d^2U}{d\varphi^2} = \frac{\beta k_3 - \gamma k_2}{k_1 k_3 - k_2^2} T, \quad \frac{d\phi}{d\varphi} = \frac{\gamma k_1 - \beta k_2}{k_1 k_3 - k_2^2} T. \quad (44)$$

Combining equation (39) and (44) leads to the following expression for the circumferential normal stresses

$$\sigma_{\varphi i} = E_i \left\{ \frac{1}{k_1 k_3 - k_2^2} \left( \frac{\beta k_3 - \gamma k_2}{r} + \gamma k_1 - \beta k_2 \right) - \alpha_i \right\} T, \quad (i = 1, 2). \quad (45)$$



With  $\sigma_{\varphi i}$  the normal stress  $\sigma_{ri}$  can be determined by utilizing the equilibrium equation

$$\frac{d}{dr}(r\sigma_{ri}) = \sigma_{\varphi i} \quad (i = 1, 2). \quad (46)$$

Substituting  $\sigma_{\varphi i}$  and solving the resulting equation for  $\sigma_{ri}$  yields

$$\begin{aligned} \sigma_{r1}(r) = E_1 \left\{ \frac{1}{(k_1 k_3 - k_2^2) r} (\beta k_3 - \gamma k_2) \ln \frac{r}{R_1} + \right. \\ \left. + (\gamma k_1 - \beta k_2) (r - R_1) - \alpha_1 \frac{r - R_1}{r} \right\} T, \quad R_1 \leq r \leq R_2, \end{aligned} \quad (47)$$

$$\begin{aligned} \sigma_{r2}(r) = \frac{R_2}{r} \sigma_{r1}(R_2) + E_2 \left\{ \frac{1}{(k_1 k_3 - k_2^2) r} (\beta k_3 - \gamma k_2) \ln \frac{r}{R_2} + \right. \\ \left. + (\gamma k_1 - \beta k_2) (r - R_2) - \alpha_2 \frac{r - R_2}{r} \right\} T, \quad R_2 \leq r \leq R_3. \end{aligned} \quad (48)$$

Integration of equation (44) by taking boundary condition (8) into account leads to the following expressions for the radial and circumferential displacements:

$$U(\varphi) = \frac{\beta k_3 - \gamma k_2}{k_1 k_3 - k_2^2} (1 - \cos \varphi) T, \quad (49)$$

$$v(\varphi, r) = \frac{(\gamma k_1 - \beta k_2) r \varphi - (\beta k_3 - \gamma k_2) \sin \varphi}{k_1 k_3 - k_2^2} T. \quad (50)$$

#### 4. NUMERICAL EXAMPLE

The following data are used in the numerical example:

$$R_1 = 0.35 \text{ m}, \quad R_2 = 0.4 \text{ m}, \quad R_3 = 0.45 \text{ m},$$

$$E_1 = 200 \text{ GPa}, \quad E_2 = 70 \text{ GPa},$$

$$\nu_1 = 0.27, \quad \nu_2 = 0.33,$$

$$\alpha_1 = 11 \cdot 10^{-6} \frac{1}{\text{K}}, \quad \alpha_2 = 23 \cdot 10^{-6} \frac{1}{\text{K}},$$

$$T = 200 \text{ K}, \quad \vartheta = \frac{3}{2} \pi.$$

Beam component 1 is made of steel. The material of beam component 2 is aluminum. The graphs in Figures 2 and 3 show the normal stresses  $\sigma_r$  and  $\sigma_\varphi$  in a comparison with finite element solutions. The latter was carried out by using the commercial Abaqus CAE software (coupled temperature-displacement solver).

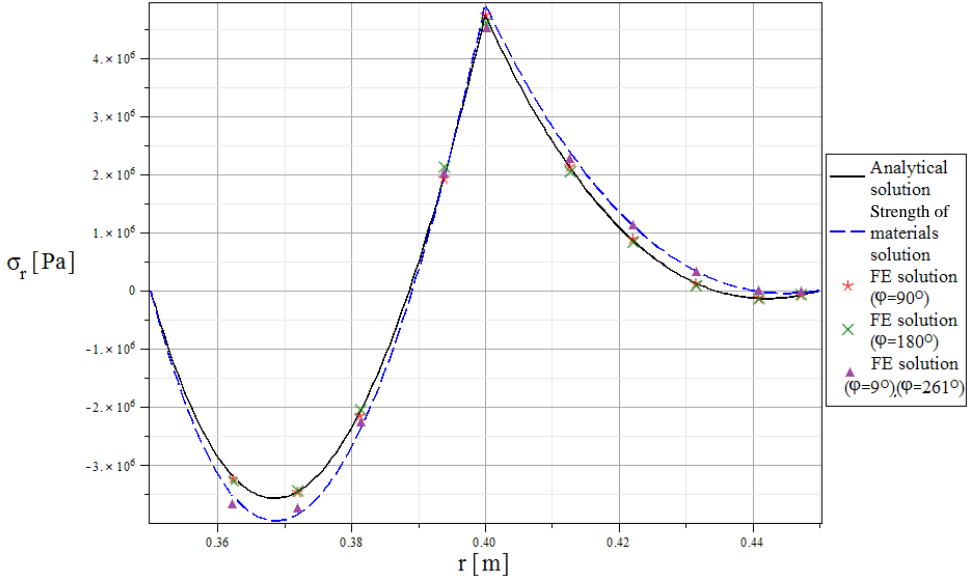


Figure 2. Plots of the radial normal stresses

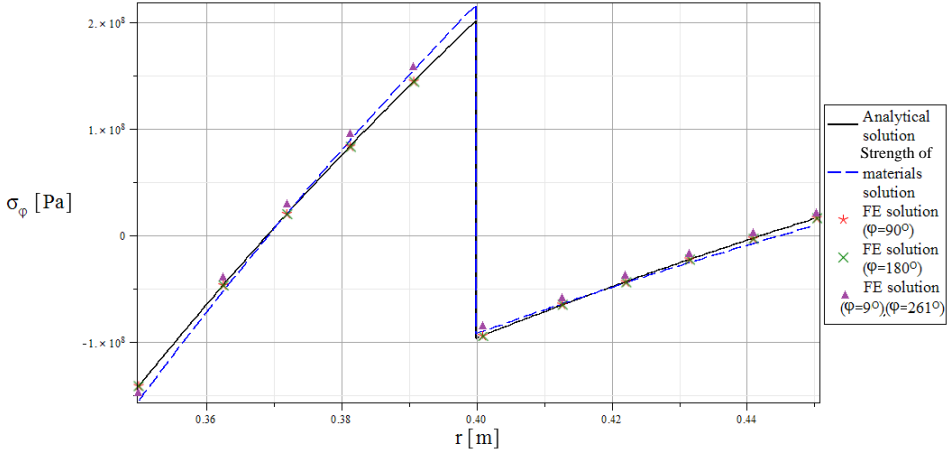


Figure 3. Plots of the circumferential stresses

In Figure 4 the finite element model of the bimetallic curved beam and von Mises equivalent stress field are presented, in which we can see that the stresses do not depend on the polar angle  $\varphi$  aside from the narrow neighborhood of the end cross sections.

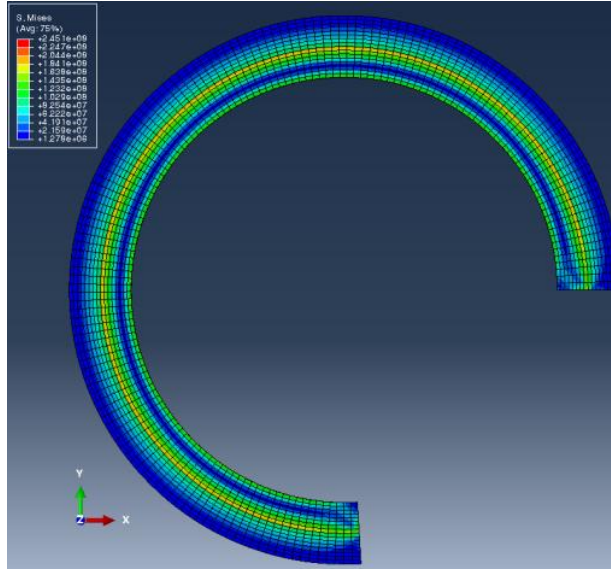


Figure 4. The finite element model with the equivalent stress field

Figures 5 and 6 show the 3D graphs of displacements  $U(r, \varphi)$  and  $v(r, \varphi)$  obtained by the previously presented elasticity solution when  $R_1 \leq r \leq R_3$  and  $0 \leq \varphi \leq \pi$ .

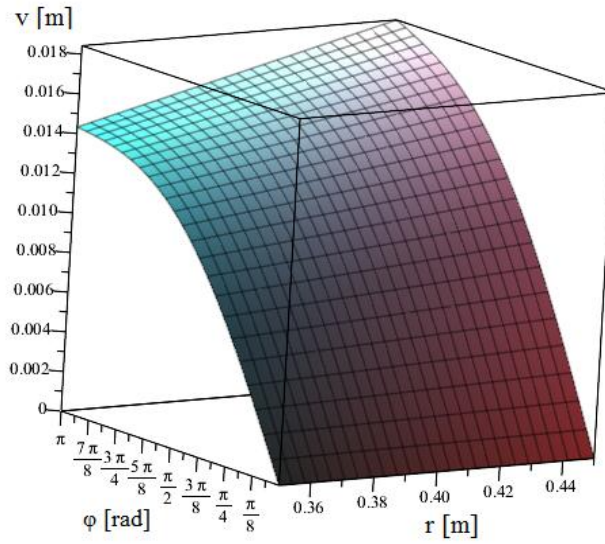


Figure 5. The circumferential displacement field

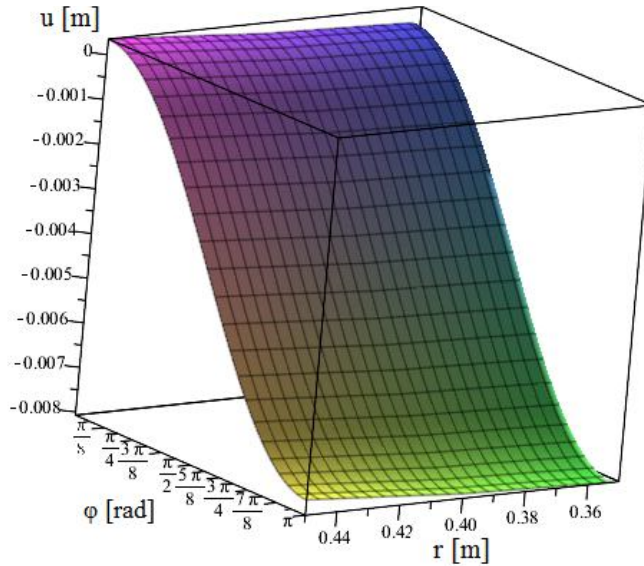


Figure 6. The radial displacement field

## 5. CONCLUSIONS

This paper presents two models to analyze the curved bimetallic beams. Presented elasticity and strength of materials approaches are checked by finite element simulations (using Abaqus FE software). The stresses obtained by the analytical method and FEM solution are in good agreement except for the end cross sections of the curved bimetallic beam. The presented analytical methods can be used to design a two-layered curved composite members which are in a high temperature environment.

## REFERENCES

1. S. P. Timoshenko. "Analysis of bi-metal thermostats." *Journal of the Optical Society of America*, **11**(3), (1925), pp. 233–255.
2. S. P. Timoshenko. *The Collected Papers*. McGraw Hill, New York, 1953. DOI: 10.1126/science.120.3113.339-a.
3. W. C. Young and Budynas R. G. *Roark's Formulas of Stress and Strain*. 7th ed. McGraw Hill, New York, 2002.
4. M. Aignatoaie. "FEA study on the elastic deformation process of a simple bimetal beam." *Applied Mechanics and Materials*, **371**(8), (2013), pp. 448–452. DOI: 10.4028/www.scientific.net/AMM.371.448.
5. E. Suhir. "Interfacial stresses in bimetal thermostats." *Journal of Applied Mechanics*, **56**(3), (2013), pp. 595–600. DOI: 10.1115/1.3176133.
6. D. Ramos, I. Mertens, M. Callega, and I. Tamayo. "Study on the origin of bending induced by bimetallic effect on microcantilever." *Sensors*, **7**(9), (2007), pp. 1757–1765. DOI: 10.3390/s7091757.

7. A. V. Rao, K. S. V. Prasad, M. Avinash, K. Nagababu, V. Manohar, P. S. R. Raju, and G. R. Chandra. "A study on deflection of a bimetallic beam under thermal loading using finite element analysis." *International Journal of Engineering and Advanced Technology*, **2**(1), (2012), pp. 81–82.
8. W. H. Chu, M. Mehregany, and R. L. Mullen. "Analysis of tip deflection and force of a bimetallic cantilever microactuator." *Journal of Micromechanics and Microengineering*, **3**(1), (1993), pp. 4–7. DOI: 10.1088/0960-1317/3/1/002.
9. B. A. Boley and I. H. Weiner. *Theory of Thermal Stresses*. Dover Publication, New York, 1997.
10. R.B. Hetnarski and Eslami M.R. *Thermal Stresses – Advanced Theory and Application*. Springer, Berlin, 2010. DOI: 10.1007/978-1-4020-9247-3.
11. Á. Lengyel and Ecsedi I. "Curved composite beam with interlayer slip loaded by radial load." *Curved and Layered Structures*, **2**(1), (2015), pp. 50–58. DOI: 10.1515/c1s-2015-0004.
12. L.P. Kiss and G. Szeidl. "Nonlinear in-plane stability of heterogeneous circular beams subjected to a radial force at the crown point." *Technische Mechanik*, **35**(1), (2015), pp. 1–30.
13. I. Ecsedi and K. Dluhi. "A linear model for the static and dynamic analysis of non-homogeneous curved beams." *Applied Mathematical Modelling*, **29**(12), (2015), pp. 1211–1231. DOI: 10.1016/j.apm.2005.03.006.



## FLUID-STRUCTURE INTERACTION OF FOUR RIGIDLY-CONNECTED SQUARE CYLINDERS IN STEADY FLOW

GUOQIANG TANG, MINGYIN DUAN, LIN LU  
State Key Laboratory of Coastal and Offshore Engineering  
Dalian University of Technology, Dalian 116024, China  
[LuLin@dlut.edu.cn](mailto:LuLin@dlut.edu.cn)

MING ZHAO  
School of Computing, Engineering and Mathematics,  
Western Sydney University, Penrith, NSW 2751, Australia

[Received: November 5, 2018; Accepted: March 19, 2019]

**Abstract.** Dynamic responses of four rigidly-connected square cylinders in a square configuration subjected to two-dimensional steady flow of a constant property Newtonian fluid were investigated numerically. The focus of the present study is to investigate the effects of the angle of attack  $\alpha$  on the dynamic responses by varying  $\alpha$  from  $0^\circ$  to  $15^\circ$  in intervals of  $2.5^\circ$  at a fixed  $L = 4$  ( $L$  is the non-dimensional center-to-center distance between two adjacent square cylinders, normalized by the side length of the square cylinder  $B$ ). For each  $\alpha$ , the reduced velocity ( $V_r$ ) ranges from 1 to 40. The Reynolds number  $Re$ , mass ratio  $m^*$  and structural damping ratio  $\zeta$  maintain constants of 180, 10 and 0, respectively. Numerical results show that the angle of attack  $\alpha$  has a significant influence on the dynamic response. When  $\alpha \leq 5^\circ$ , galloping occurs in addition to vortex-induced vibration (VIV), while it weakens for  $\alpha = 7.5^\circ$  and  $10^\circ$ , and finally disappears as  $\alpha = 12.5^\circ$  and  $15^\circ$ , leaving only VIV response. The effects of  $L$  on the responses of the four-square-cylinder oscillating system were also examined for  $Re = 180$ ,  $V_r = 40$ , and  $\alpha = 2.5^\circ$ . Numerical results show that  $L$  affects not only the response displacement but also the vortex shedding mode. Galloping with large response amplitude can happen at either large  $L = 4$  or small  $L = 1.5$  and 2. The response amplitude is relatively small as  $2.5 \leq L \leq 3.5$  due to the influence of the flow in the gap between the square cylinders. For the particular case of  $L = 3.5$ , a combined vortex shedding mode is identified, where the vortex shedding from the top row square cylinders behaves as that from an elongated single body while the vortex shedding from the bottom row cylinders presents a co-shedding mode.

*Mathematical Subject Classification:* 34F05, 35R99

*Keywords:* Vortex-induced vibration, galloping, arbitrary Lagrangian-Eulerian method, Petrov-Galerkin Finite Element Method, square cylinder

### 1. INTRODUCTION

The interaction between multi-body structures and fluid flows has received increasing attention due to its significance in both academic research and practical engineering. It has motivated many investigations to understand flow-induced vibrations. Fluid flow past an elastically-mounted circular cylinder has served as the primary VIV

problem and has been investigated extensively both numerically and experimentally. Comprehensive reviews on VIV of circular cylinders can be found in [1–5].

Compared with the VIV of circular cylinders, however, fluid flows past square cylinders have attracted less attention. Previous studies generally focused on fluid flows over fixed square cylinders. The effects of angle of attack on the fluid force, and vortex shedding mode were examined [6–8]. As for an elastically-mounted square cylinder placed in a fluid flow, in addition to VIV, galloping is another physical mechanism which occurs when a structure has a non-axisymmetric cross-section [9–11].

A number of experimental investigations have been carried out to understand the physics involved in the dynamic response of a square cylinder. Bokaian and Geoola [12] studied the galloping instability of square cylinders and the corresponding synchronized vortex shedding patterns. The dynamic response of square cylinders was investigated experimentally in a wind tunnel [11]. They reported a galloping response of 1:3 synchronization, where the vortex shedding frequency is three times that of the vibration frequency of the square cylinder. A similar 1:3 synchronization phenomenon was also reported by Wang and Zhou [13], who investigated the effect of attack angle on the dynamic response of a square cylinder. Nemes et al. [14] investigated the effect of angle of attack on the dynamic response experimentally, and found a higher branch of response amplitude at angles of attack of  $\alpha \in [10^\circ, 22.5^\circ]$ . The attack angle of  $\alpha = 0^\circ$  corresponds to the situation in which the flow direction is perpendicular to two side faces of the cylinder. In the higher branch, the maximum amplitude was found to be significantly larger than that in the upper branch of VIV of a circular cylinder, and the vibration frequency synchronized with half of the Strouhal frequency. Zhao et al. [15] conducted a refined experimental study on the dynamic responses of a square cylinder at three different angles of attack, namely  $\alpha = 0^\circ$ ,  $20^\circ$  and  $45^\circ$ . For  $\alpha = 0^\circ$ , a typical galloping response is observed which is characterized by a gradual buildup of the amplitude with the reduced velocity. For  $\alpha = 45^\circ$ , the dynamic response is dominated by VIV. Similar to the findings of Nemes et al. [14], Zhao et al. [15] also observed a higher branch at  $\alpha = 20^\circ$ , which is confirmed to be a sub-harmonic mode. In the higher branch, the spatial-temporal symmetry of the vortex shedding is broken, leading to a non-zero mean lift force and the high-amplitude branch.

A number of numerical studies have also been conducted to investigate the dynamic response of a square cylinder. Sen and Mittal [16] conducted numerical simulations of fluid flow past a square cylinder at  $\alpha = 0^\circ$ . They found that the response amplitude with the reduced velocity can be divided into the primary lock-in, desynchronization and galloping regimes. It was observed that the vortex shedding mode is the 2S mode in the primary lock-in regime, and 2S or 2P modes in the galloping regime. The 2S mode means that two single vortices are shed from the square cylinder during one vibration period, while the 2P mode means that two pairs of vortices are formed and shed every vibration cycle, according to the definition of Williamson and Roshko [17]. Later on, Sen and Mittal [18] examined the effects of the mass ratio on the dynamic response of a square cylinder at low Reynolds numbers. The mass ratios of  $m^* = 1$ ,



5, 10 and 20 were considered in the numerical simulations. The results indicate that only VIV response appears as  $m^* = 1$ . For  $m^* \geq 5$ , galloping branch is observed in addition to VIV. Joly et al. [19] numerically studied the influence of  $\alpha$  and  $m^*$  on the dynamic response of a square cylinder, and developed a sinusoidal quasi-steady model to predict the galloping response. Zhao et al. [20] examined the effects of  $\alpha$  on the VIV response of a square cylinder with  $\alpha = 0^\circ$ ,  $22.5^\circ$  and  $45^\circ$ . The numerical results suggested that the angle of attack affects not only the response amplitudes but also the vortex shedding modes. The dynamic responses of square and rectangular cylinders were numerically studied by Zhao [21] and Cui et al. [22]. Different response regimes and vortex shedding modes were reported according to the aspect ratio, which is defined as the cylinder dimension in the cross-flow direction to that in the inline direction.

Compared with the studies of the dynamic responses of an elastically-mounted square cylinder, investigations on fluid multiple square cylinders are fewer and less documented in the literature. The very common configuration of multiple square cylinders is the square arrangement of four square cylinders such as the legs of the tension leg platform in offshore oil and gas engineering. Liu et al. [23] carried out laboratory tests to study the fluid dynamic characteristics around four stationary square-cross-section cylinders in a square arrangement at high Reynolds numbers. The effects of the angle of attack  $\alpha$  and the center-to-center distance  $L$  between the cylinders on the fluid forces as well as the vortex shedding frequency were investigated. So far, inadequate attention has been paid to the dynamic response of four rigidly-connected square cylinders. In the present study, the dynamic responses of the four rigidly-connected square cylinders in two-dimensional steady flow of a constant property Newtonian fluid were investigated numerically. The aim of this study is to investigate the effects of  $\alpha$  on the dynamic responses. The two-dimensional incompressible Navier-Stokes (N-S) equations are solved by a Petrov-Galerkin Finite Element Method (PG-FEM) to predict the fluid flow. An arbitrary Lagrangian-Eulerian (ALE) method is employed to deal with the moving boundaries of the square cylinders. The non-dimensional center-to-center distance between two adjacent square cylinders is fixed as  $L = 4$  initially. Numerical simulations were performed with a constant Reynolds number  $Re = 180$ . The Reynolds number is defined as  $Re = UB/v$ , where  $v$  is the kinematic viscosity of the fluid,  $B$  is the side length of the square cylinder and  $U$  is the free-stream velocity. The angle of attack  $\alpha$  ranges from  $0^\circ$  to  $15^\circ$  with an interval of  $2.5^\circ$ , and the reduced velocity  $V_r$  varies from 1 to 40 with an increment of 1.

The remainder of this article is organized as follows. The numerical method employed in this study is introduced in Section 2. The necessary mesh dependent tests are presented in Section 3. The numerical results are shown and discussed in Section 4, and conclusions are drawn in Section 5.

## 2. NUMERICAL METHOD

Figure 1 shows a sketch of the computational domain for simulating the dynamic responses of the four rigidly-connected square cylinders in a square configuration in

steady flow. A coordinate system is defined with its origin fixed at the center of the four-cylinder system with the  $x$ -coordinate pointing to the flow direction. The set of four rigidly-connected square cylinders is allowed to oscillate in both the cross-flow and in-line directions. The natural frequencies in the  $x$ - and  $y$ -directions are the same. The Reynolds number is set as  $Re = 180$  throughout the numerical simulations, hence the flow is within the laminar regime so that two-dimensional numerical simulation is appropriate to reveal the potential physical mechanism.

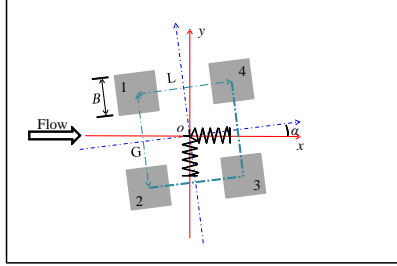


Figure 1. Numerical setup for fluid flow past four elastically supported rigidly connected square cylinders

In this study, the non-dimensional variables of velocity  $(u, v)$ , the time  $t$ , the coordinate  $(x, y)$  and the pressure  $p$  are normalized as  $(u, v) = (u', v')/U$ ,  $t = t'U/B$ ,  $(x, y) = (x', y')/B$ , and  $p = p'/(\rho U^2)$ , respectively, where the prime symbol represents the dimensional variables,  $B$  is the side length of the square cylinder,  $\rho$  is the fluid density and  $U$  is the free-stream velocity. The ALE method is introduced to deal with the moving boundaries induced by the oscillations of the rigidly-connected square cylinders. The non-dimensional governing equations in the ALE scheme are expressed as

$$\frac{\partial u_i}{\partial x_i} = 0, \quad (1)$$

$$\frac{\partial u_i}{\partial t} + (u_j - u_{j,\text{mesh}}) \frac{\partial u_i}{\partial x_j} = -\frac{\partial p}{\partial x_i} + \frac{1}{Re} \frac{\partial^2 u_i}{\partial x_i \partial x_j}. \quad (2)$$

where  $x_i$  is the Cartesian coordinate with  $x_1 = x$  and  $x_2 = y$ ,  $u_i$  is the velocity component in the  $x_i$  direction and  $u_{j,\text{mesh}}$  is the velocity of the moving computational mesh. The N-S equations are solved by the PG-FEM, which was same as in Zhao et al. [24]. The details of the PG-FEM and the computational procedure are well documented in [24] and will not be repeated in this article.

The motion of the four rigidly connected square cylinders is predicted by solving the following linear oscillator equation

$$\frac{\partial^2 X_i}{\partial t^2} + 4\pi\zeta F_n \frac{\partial X_i}{\partial t} + (2\pi F_n)^2 X_i = \frac{C_i}{2m^*}, \quad (3)$$

where  $X_i$  is the non-dimensional displacement of the square cylinders, normalized by the side length of the square cylinder, in the  $x_i$ -direction.  $m^* = m/m_s$  is the mass ratio with  $m$  being the total mass of the square cylinders and  $m_s$  representing the displaced mass of the fluid. In the present study, the mass ratio is set as  $m^* = 10$ ,

and  $\zeta = c/(4km)^{1/2}$  is the damping ratio, where  $c$  and  $k$  are the structural damping coefficient and the spring stiffness, respectively. To investigate possible large amplitude response,  $\zeta = 0$  is adopted in the numerical simulations. In equation (3),  $F_n = f_n B/U$  is the dimensionless structural natural frequency with  $f_n$  being the structural natural frequency,  $C_i$  is the total hydrodynamic coefficient on the square cylinders in the  $x_i$ -direction, which is defined as  $C_i = 2F_i/(\rho BU^2)$  with  $F_i$  being the total hydrodynamic force in the  $x_i$ -direction. In the following discussions, the hydrodynamic coefficients in the in-line and cross-flow directions  $C_1$  and  $C_2$  are replaced by the drag and lift coefficients  $C_D$  and  $C_L$ , respectively. In equation (3),  $X_1$  and  $X_2$  indicate the displacements in  $x$  and  $y$  directions, namely  $X$  and  $Y$ , respectively, and they are given as

$$\frac{\partial^2 X}{\partial t^2} + 4\pi\zeta F_n \frac{\partial X}{\partial t} + (2\pi F_n)^2 X = \frac{C_D}{2m^*}, \quad (4)$$

$$\frac{\partial^2 Y}{\partial t^2} + 4\pi\zeta F_n \frac{\partial Y}{\partial t} + (2\pi F_n)^2 Y = \frac{C_L}{2m^*}. \quad (5)$$

Under the ALE description, the nodal coordinates inside the computational domain should be moved according to the motion of the square cylinders. After each computational time step, the mesh is updated by solving the following governing equation [25–27]:

$$\Delta \cdot (\gamma S_i) = 0, \quad (6)$$

where  $S_i$  denotes the displacement of the mesh modal point in the  $x_i$ -direction. To avoid severe mesh deformation around the square cylinders, a parameter  $\gamma = 1/A$  is introduced to control mesh deformation, where  $A$  is the area of the computational mesh [25–27]. The displacements of the computational nodes on the cylinder surface are the same as that of the oscillating square cylinders, while the displacements of the mesh maintain zero for the rest of the boundaries. By assigning the displacements for all the boundaries, equation (6) is solved by a Galerkin FEM.

A rectangular computational domain with a height of  $40B$  in cross-flow direction and a length of  $60B$  in flow direction is adopted, as shown in Figure 1. The values of upstream and downstream lengths are  $20B$  and  $40B$ , respectively. The computational domain is discretized into four-node quadrilateral bi-linear elements. The total number of FEM nodes and elements are 55057 and 54400, respectively. The boundary of each square cylinder is divided into 160 uniformly distributed nodes, resulting in a minimum mesh size along the square cylinder of 0.025. The radial length of the elements next to the square cylinder surface is 0.01.

The boundary conditions are specified as follows. On the inlet boundary, the horizontal velocity is set to be  $u = 1$  and the vertical velocity component is zero. No-slip boundary condition is specified on the surfaces of the square cylinders, i.e. the flow velocity is the same as the vibration velocity of the square cylinders. At the outlet, the pressure is set to be zero, and the gradient of the velocity in the flow direction is zero. On the two lateral boundaries, the gradient of the pressure and the velocity in the transverse direction of the flow are zero. The numerical simulations start from an initial condition that the pressure and the velocity are zero in the whole fluid domain.

## 3. MESH DEPENDENCE STUDY

The PG-FEM numerical model and computational code developed by Zhao et al.[24] has been used to simulate the dynamic responses of four square cylinders. It has been demonstrated that this numerical model is capable of simulating the VIV of a square cylinder [20], the galloping response of rectangular cylinders [21, 22], the wake-induced vibrations of two tandem cylinders [28], and the VIV of four rigidly connected circular cylinders [29, 30]. The capability of the numerical model has been validated in [16, 31–33] and will not be repeated here.

A mesh dependent study was performed to demonstrate that the mesh used in this study is fine enough to obtain accurate results. Numerical simulations were performed for a fluid flow over four rigidly connected square cylinders at  $Re = 180$ ,  $V_r = 40$  and angles of attack  $\alpha = 0^\circ$ ,  $5^\circ$  and  $10^\circ$ , covering both the VIV and the galloping responses. The corresponding numerical results were compared based on the two different mesh densities, defined as normal mesh and dense mesh, respectively. The total numbers of the nodes and elements are 55057 and 54400 for the normal mesh, while they are 66777 and 66000 for the dense mesh. Each side of the square cylinders is divided into 40 nodes in the normal mesh and 50 nodes for the dense mesh. Table 1 shows the comparisons of the root mean square displacements  $X_{rms}$  and  $Y_{rms}$ , the mean total drag coefficients  $C_{D,mean}$ , and the root mean square total drag and lift coefficients of  $C_{D,rms}$  and  $C_{L,rms}$ . The total drag and lift coefficients are the sum of the drag and lift coefficients of the four square cylinders, respectively. The results in Table 1 demonstrate that the differences between the numerical results in terms of the two meshes are very small. The maximum difference is less than 4.4%. Hence, the normal mesh was used for the numerical simulations in this study. In addition, numerical simulations of VIV of four separately mounted circular cylinders in an in-line square configuration were conducted in our previous study [30], adopting the same numerical model as used in this study. The sizes of the computational domain, upstream, downstream distances and the time step in the present study are similar to those used in [30] for the case of the center-to-center distance  $L/D = 4$ , where  $D$  is the diameter of the circular cylinder. At the same time, the total numbers of the nodes and elements in the present study are larger than those used in [30]. Hence, it is believed that the numerical results in the present study will not be sensitive to the computational mesh.

Table 1. Root mean square displacements and hydrodynamic forces based on normal mesh and dense mesh

Case	Mesh	$X_{rms}$	$Y_{rms}$	$C_{D,mean}$	$C_{D,rms}$	$C_{L,rms}$
$\alpha = 0^\circ$ , $V_r = 40$	Normal mesh	0.1371	0.8581	6.4580	0.6057	1.0084
$\alpha = 5^\circ$ , $V_r = 40$	Normal mesh	0.2341	0.6679	5.8013	0.5882	0.8545
$\alpha = 10^\circ$ , $V_r = 40$	Normal mesh	0.0367	0.0989	5.1219	0.3543	2.0183
$\alpha = 0^\circ$ , $V_r = 40$	Dense mesh	0.1392	0.8501	6.4591	0.6250	1.0261
$\alpha = 5^\circ$ , $V_r = 40$	Dense mesh	0.2272	0.6661	5.8355	0.5896	0.8200
$\alpha = 10^\circ$ , $V_r = 40$	Dense mesh	0.0383	0.0972	5.1300	0.3555	2.0214

#### 4. NUMERICAL RESULTS AND DISCUSSION

**4.1. Vibration amplitude and frequency for  $L = 4$ .** Figure 2 shows the variations of the vibration amplitudes in the  $x$ - and  $y$ -directions with the reduced velocity for  $\alpha$  ranging from  $0^\circ$  to  $15^\circ$ . The vibration amplitudes in the  $x$ - and  $y$ -direction are defined as  $A_x = (X_{\max} - X_{\min})/2$  and  $A_y = (Y_{\max} - Y_{\min})/2$ , respectively, where the subscripts ‘max’ and ‘min’ stand for the maximum and minimum displacements, respectively. Figure 3 shows the variations of the non-dimensional response frequency with the reduced velocity under these angles of attack. In the present study, the non-dimensional response frequency is defined as the ratio of dimensional response frequency of the cross-flow displacement to the structural natural frequency, where the dimensional response frequency is obtained by performing Fast Fourier Transform (FFT) analysis on the time history of the cross-flow displacement. The results shown in Figure 2 demonstrate that for some cases, for example when  $\alpha = 5^\circ$  and  $22 \leq V_r \leq 25$ , the response amplitude has dual values in Figure 2 and so does the frequency in Figure 3.

For these cases, the vibration amplitudes (empty circles in Figure 2) are found to be very small if the simulation is initiated with the zero initial condition with the pressure and fluid velocity being zero. The response amplitude increases with the increasing reduced velocity as  $V_r \geq 13$  and  $\alpha = 5^\circ$ , except  $22 \leq V_r \leq 25$ , where the amplitudes are nearly zero. The increase of the response amplitude with increasing  $V_r$  is a typical characteristic of galloping. However, it is clear that the response amplitudes and frequencies are out of this trend when  $\alpha = 5^\circ$  and  $22 \leq V_r \leq 25$ . It is likely that the response in the reduced velocity range of  $22 \leq V_r \leq 25$  depends on the initial condition. To justify this, simulations were carried out for  $22 \leq V_r \leq 25$  by using the fully developed flows of neighboring reduced velocities as initial conditions where galloping occurs. Specifically, the last step results of  $V_r = 21$  were used as the initial condition for  $V_r = 22$  and 23, and the last step results of  $V_r = 26$  were employed as the initial condition for  $V_r = 24$  and 25. The results using the solution of galloping as the initial conditions are plotted as the solid circles in Figure 2. It is found that the response amplitude and frequency are indeed different from their corresponding values when the zero initial condition is used.

Nemes et al. [14] reported a galloping response of a square cylinder when  $\alpha = 0^\circ$ , and VIV response when  $\alpha = 45^\circ$ . Sen and Mittal [16] simulated the dynamic response of a square cylinder with  $m^* = 10$  at low Reynolds numbers, and found a primary lock-in regime and a secondary lock-in regime. The response in the primary lock-in regime is very similar to that of a circular cylinder. In the secondary lock-in regime, the response amplitude increases continuously with the increase of the reduced velocity. The vibration in the secondary lock-in regime is essentially galloping. Zhao [21] also reported one VIV regime and one galloping regime for the dynamic responses of square and rectangular cylinders. The VIV regime includes an initial branch and a lower branch. In this study, VIV regime is observed to occur at about  $6 \leq V_r \leq 9$  for all the simulated angles of attack. However, it is interesting to find that two VIV lock-in regimes are identified when the angle of attack is large enough. For example

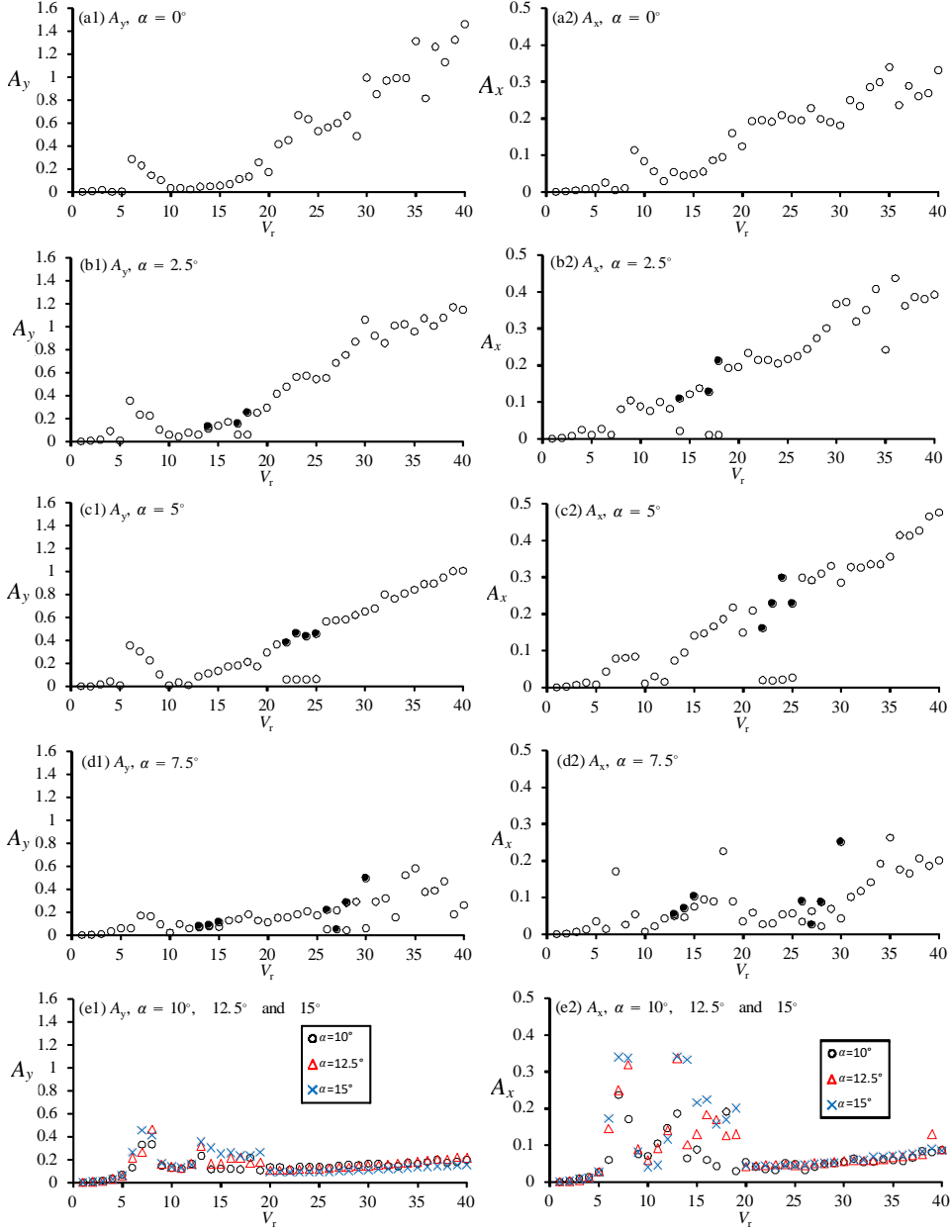


Figure 2. Variations of the vibration amplitudes in the in-line and cross-flow directions with the reduced velocity for different angle of attack values. Empty symbols, still fluid is the initial condition; filled symbols, galloping solution is used as the initial condition

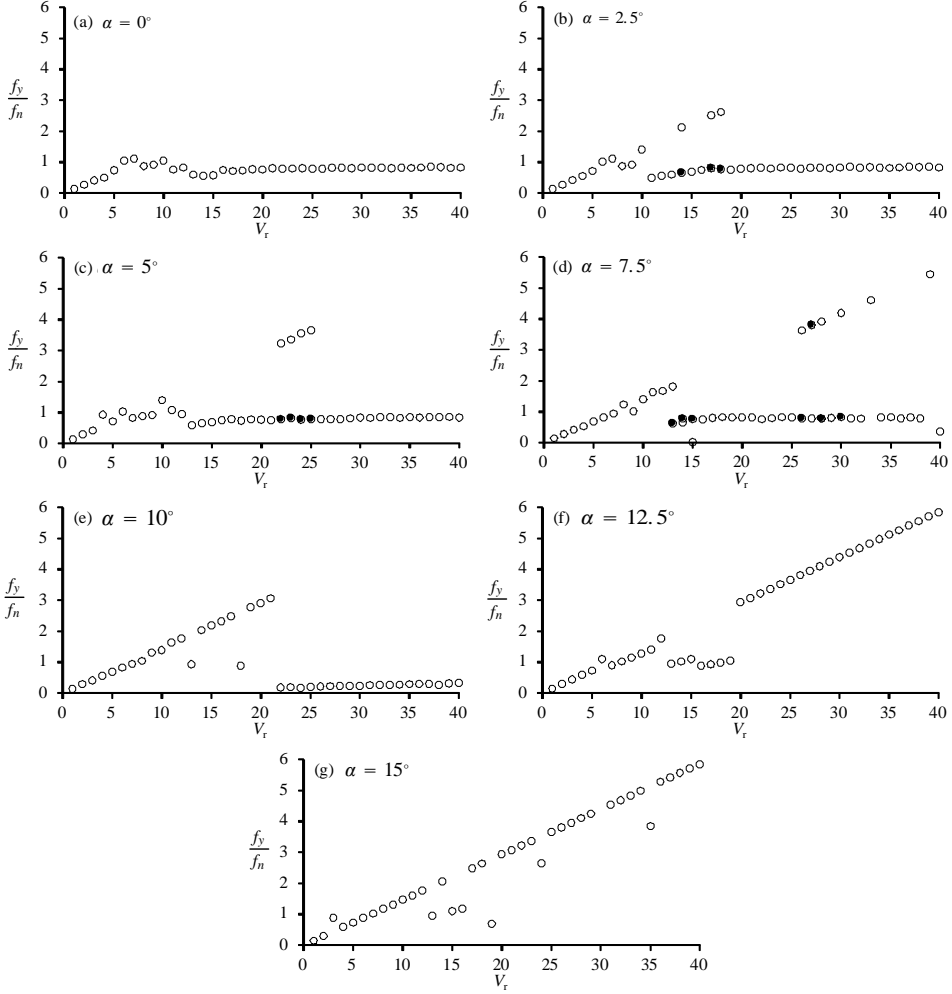


Figure 3. Variation of the vibration amplitudes in the in-line and cross-flow directions with the reduced velocity for different angle of attack values. Empty circles, still fluid is the initial condition; filled circles, galloping solution is used as the initial condition

at  $\alpha = 12.5^\circ$ , it is observed that the non-dimensional response frequency is close to but slightly smaller than 1 for  $V_r = 4$  as shown in Figure 3(f). It increases gradually to a value slightly greater than 1 as the reduced velocity increases to  $V_r = 9$ . This trend is broken at  $10 \leq V_r \leq 12$ . However, as the reduced velocity increases to  $V_r = 13$ , lock-in occurs again in the reduced velocity range of  $13 \leq V_r \leq 19$ . As reduced velocity exceeds  $V_r = 20$ , the response frequency increases linearly with the increasing reduced velocity. The galloping regimes are clearly observed at  $\alpha = 0^\circ$ ,

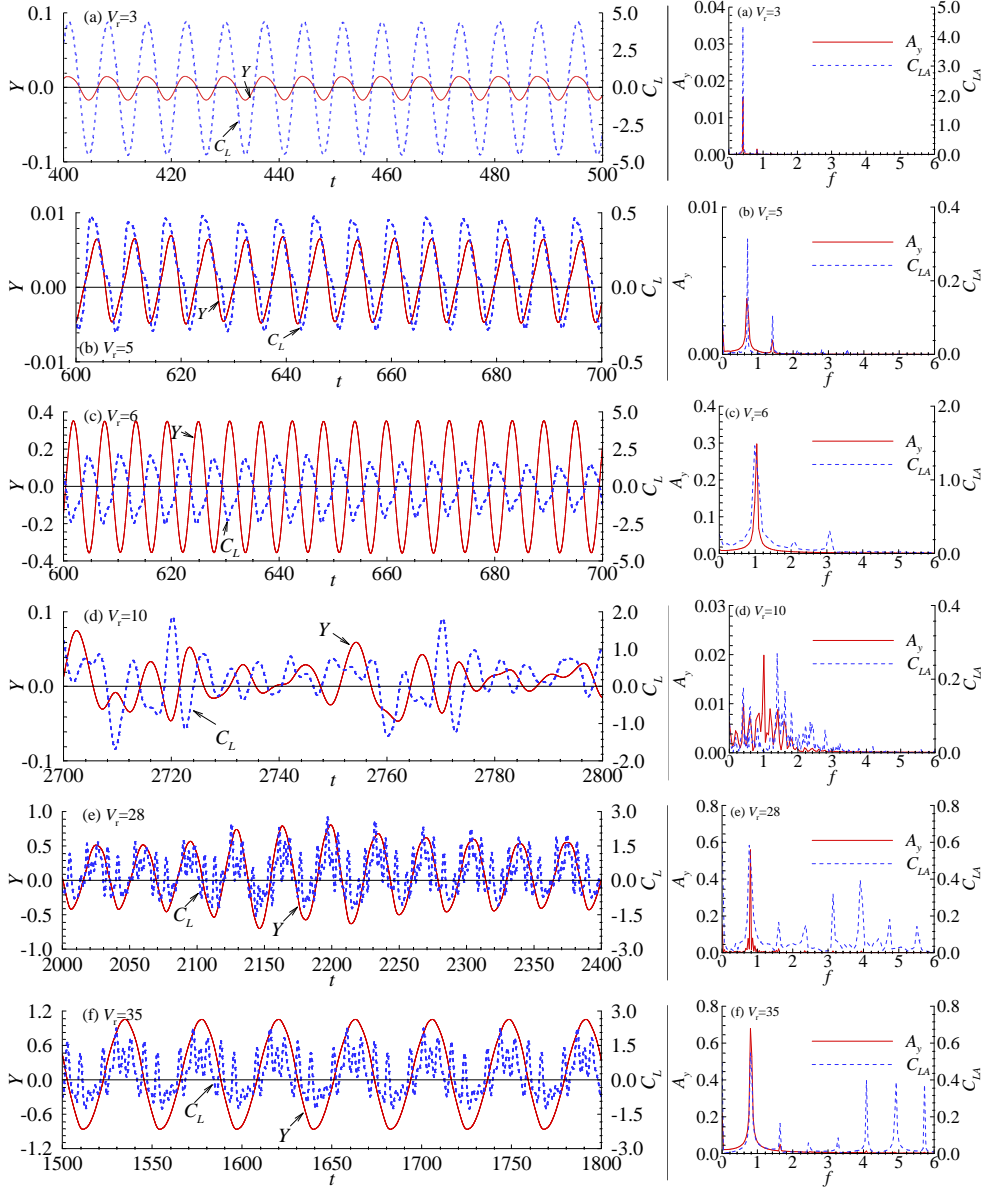


Figure 4. Time histories of cross-flow displacement and lift coefficients (left column) for  $\alpha = 2.5^\circ$  and FFT spectra (right column) for different reduced velocity values

$\alpha = 2.5^\circ$  and  $\alpha = 5^\circ$  which are characterized by the response frequencies that are slightly lower than 1 at high reduced velocities as shown in Figures 3(a)-(c); such a trend is not clear at  $\alpha = 7.5^\circ$  and disappears at  $\alpha = 10^\circ$ . If galloping occurs, the



vibration amplitudes at high reduced velocities are much larger than the maximum vibration amplitudes in the VIV regime. As  $\alpha = 0^\circ$ ,  $\alpha = 2.5^\circ$  and  $\alpha = 5^\circ$ , the response amplitude increases with the increase of reduced velocity at  $V_r \geq 15$ , which are in the galloping regime. However, it can be seen that the occurrence of galloping depends on the initial condition for some reduced velocities for  $\alpha = 2.5^\circ$  and  $\alpha = 5^\circ$ . As  $\alpha \geq 10^\circ$ , the response amplitude remains consistently small as the reduced velocity exceeds the upper boundary of the VIV lock-in regime.

The results shown in Figure 3 demonstrate that the response frequency of the cylinder in the cross-flow direction is close to the natural frequency in both the VIV and the galloping regimes. However, the correlation between the displacement of the cylinder and the lift coefficient in the VIV regime is different from that in the galloping regime. The time histories and Fast Fourier Transform (FFT) spectra of the vibration displacement and the lift coefficient for  $\alpha = 2.5^\circ$  are shown in Figure 4 as an example to identify the difference between VIV and galloping, where results for  $A_y$  are shown in red solid lines and those for  $C_L$  are shown in blue dashed lines. The non-dimensional frequency  $f$  is defined as  $f = f^*B/U$  with  $f^*$  being the dimensional frequency. The frequencies of the vibration and the lift coefficient of the cylinder are the same in the VIV regime (Figures 4(a), (b) and (c)). In the galloping regime (Figures 4(e) and (f)), a strong high frequency component is observed in the lift fluctuations. However, it does not contribute to the vibration because the vibration amplitude corresponding to this peak frequency is extremely small. By observing the vortex shedding, it was found that the high frequency component in the lift coefficient is actually the vortex shedding frequency. It does not excite VIV because the reduced velocity is outside the lock-in regime for VIV. At  $V_r = 10$  (Figure 4(d)), the vibration changes from the non-galloping regime to the galloping regime. The VIV and galloping regimes cannot be separated from each other at high Reynolds numbers, because the galloping starts from a very small reduced velocity, resulting in an overlap between VIV and galloping regimes [14]. The VIV and galloping regimes can be distinctly identified in this study because the Reynolds number is small ( $Re = 180$ ). The VIV and galloping regimes can be separated from each other at low Reynolds numbers because the starting reduced velocity of the galloping regime is higher than the upper boundary of the VIV lock-in regime [16, 21].

It is interesting to see in Figure 3(e) that the response frequency is extremely small and does not vary with the reduced velocity when  $\alpha = 10^\circ$  and  $V_r \geq 22$ . To understand why the frequency is very low, the time histories of the displacements in the  $x$ - and  $y$ -directions for  $\alpha = 10^\circ$  and reduced velocities of  $V_r = 9, 17, 20$  and 35 are shown in Figure 5. The red lines represent the displacements in the in-line direction while the cross-flow displacements are indicated by the black lines. Regular long-period beating can be seen in Figure 5(a), while the vibration is still dominated by the frequency of the vortex shedding. It can be seen in Figure 5 that the vibration becomes asymmetric and the asymmetry becomes stronger with the increasing reduced velocity. When the reduced velocity increases to 35 (Figure 5(d)), the beating still exists, while the cylinders vibrate at a high frequency in the cross-flow direction. Its mean position also changes periodically in time with an amplitude

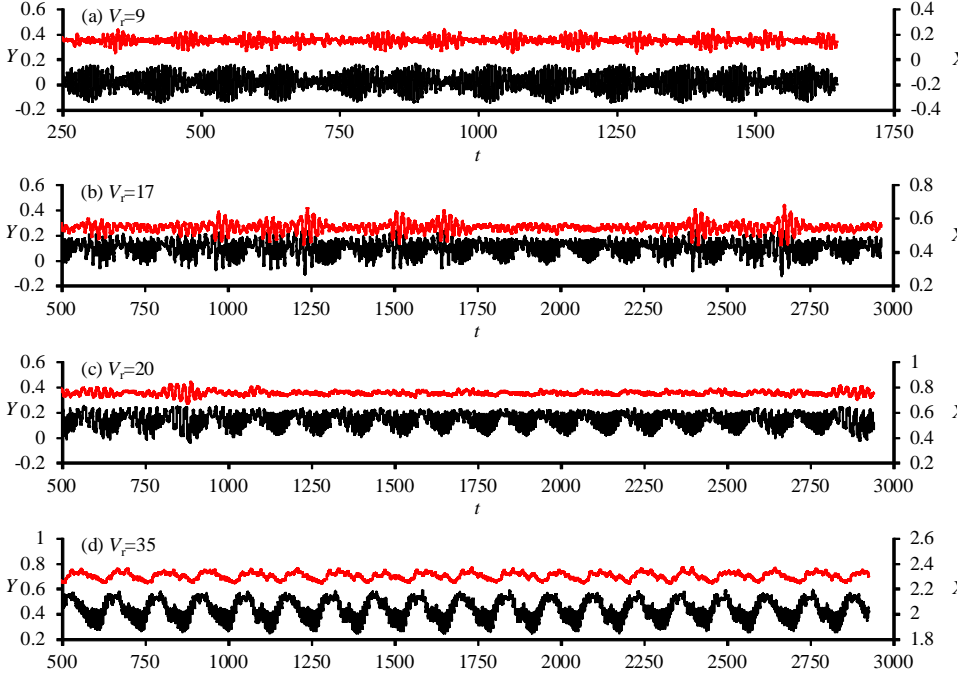


Figure 5. Time histories of the displacements of the cylinder in  $x$ - and  $y$ -directions for  $\alpha = 10^\circ$  for different reduced velocity values. Upper line, displacement in the in-line direction; Lower line, displacement in the cross-flow direction

greater than the high-frequency vibration amplitude. Both the vibration amplitude and frequency for  $\alpha = 10^\circ$  and  $V_r = 35$  are smaller than their counterparts for  $\alpha = 0^\circ$  at the same reduced velocity. The vibration for  $V_r = 9$  in Figure 5(a) is essentially a modulation between a high frequency component and a low frequency component. In Figure 5(d), the vibration is a combination of the modulation of two frequencies and a galloping. Because the galloping amplitude is much smaller than that at  $\alpha = 0^\circ$  and not significantly greater than the VIV amplitude, the vortex-induced vibration can be clearly identified in the time histories.

Figure 6 shows the FFT spectra of the  $Y$ -displacement and lift coefficient for  $\alpha = 10^\circ$  and two reduced velocities of  $V_r = 9$  and 35. In Figure 6,  $Y$ -displacement, lift coefficients  $C_L$  and structural natural frequency  $f_n$  are shown by the black dashed line, red solid line and blue dot-and-dash line, respectively. The modulation between the two signals with distinct frequencies can be identified in Figure 6. The modulation frequencies ( $f_m$ ) of the  $Y$ -displacement and the lift coefficient are found to be the same. When  $V_r = 9$ , the modulation frequency ( $f_m$ ) is much smaller than the vortex shedding frequency ( $f_s$ ). At  $V_r = 35$ , in addition to the modulation, a very small frequency exists, which is the frequency of the galloping response ( $f_g$ ). The vibration is hence a combination of a modulation and a galloping. When galloping occurs, the modulation frequency is the same as the galloping frequency.

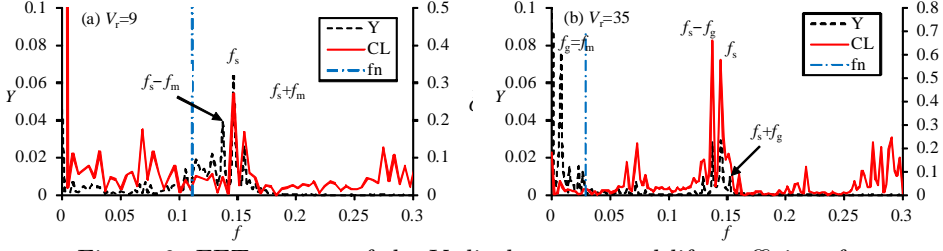


Figure 6. FFT spectra of the  $Y$ -displacement and lift coefficient for  $\alpha = 10^\circ$  and two typical reduced velocities of  $V_r = 9$  and  $35$

Based on the above analysis of the vibration amplitude and frequency, we can divide the response into three types according to the angle of attack, namely, galloping ( $\alpha = 0^\circ$  to  $\alpha = 5^\circ$ ), non-galloping or VIV ( $\alpha \geq 12.5^\circ$ ), and a combined state between them ( $\alpha = 7.5^\circ$  and  $\alpha = 10^\circ$ ). The  $Y$ -amplitude in the galloping regime increases with the increase of  $\alpha$  as shown in Figure 2(a) while the non-galloping vibration, which is outside the VIV lock-in regime, has very small amplitudes. In the combined state, the dynamic responses of the square cylinders are a combination of the weak galloping and the vortex-induced vibration.

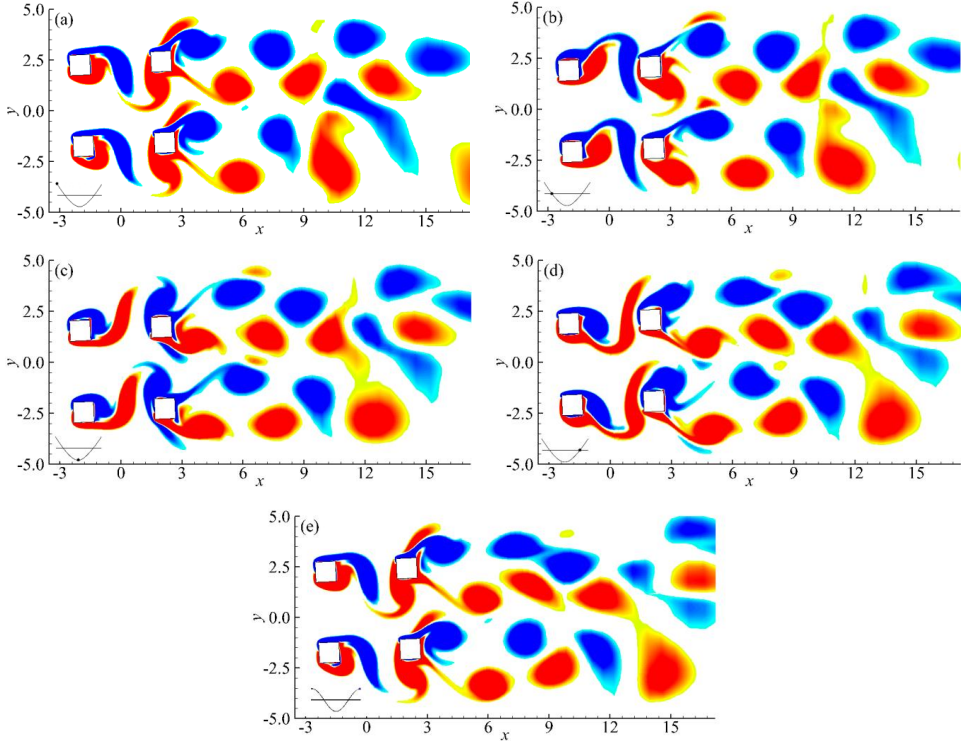


Figure 7. Vorticity contours over one period of oscillation for  $\alpha = 2.5^\circ$  and  $V_r = 6$ . (a),  $Y = Y_{\max}$ ; (b),  $Y = 0$ , moving down; (c),  $Y = Y_{\min}$ ; (d),  $Y = 0$ , moving up; (e),  $Y = Y_{\max}$

Figure 7 shows the vorticity contours over one period of oscillation for  $\alpha = 2.5^\circ$  and  $V_r = 6$ , which is in the lower branch of the VIV lock-in regime. The instantaneous position of the four-cylinder system on the  $Y$ -displacement is shown in each diagram in Figure 7. The first time instant is obtained at  $Y = Y_{\max}$  and is followed by  $1/4$  period of the oscillation of the square cylinders. A pair of vortices is shed from each of the upstream cylinders in one cycle of vibration. The vortices that are shed from the upstream cylinders attack the downstream cylinder and combine with the vortices generated from the downstream cylinders. The combination of the vortices makes the vortex shedding from the two downstream cylinders easy to identify; they are also stronger than the vortices from the upstream cylinders. The number of vortices that are shed from each of the downstream cylinders is a pair. The interaction between the vortices from the top row cylinders and those from the bottom row cylinders appears to be weak. The two rows of vortex street can be clearly seen downstream the cylinders regime.

The instantaneous  $Y$ -displacement of the four-cylinder system is marked in Figure 8 which shows the vorticity contours over one period of oscillation for  $\alpha = 2.5^\circ$  and  $V_r = 35$  in the galloping regime. The first time instant is obtained at  $Y = Y_{\max}$

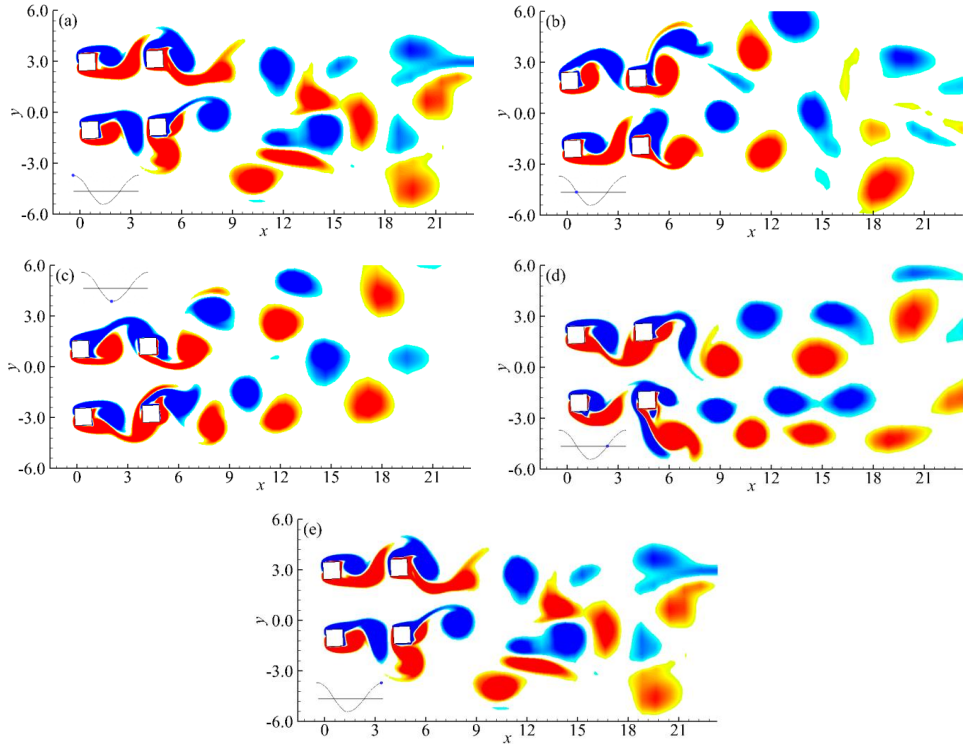


Figure 8. Vorticity contours over one period of oscillation for  $\alpha = 2.5^\circ$  and  $V_r = 35$ . (a),  $Y = Y_{\max}$ ; (b),  $Y = 0$ , moving down; (c),  $Y = Y_{\min}$ ; (d),  $Y = 0$ , moving up; (e),  $Y = Y_{\max}$

(Figure 8(a)) and is followed by each  $1/4$  period of the oscillation of the square cylinders. The number of the vortices that are shed from each of the cylinders in one period of the galloping presents also as a pair. However, there are some differences between the vortices in the VIV lock-in regime (Figure 7) and those in the galloping regime (Figure 8). In the VIV lock-in regime, the shear layers from the two sides of each upstream cylinder form vortices at a further downstream location of the cylinder than those in the galloping regime. Each of the vortices from the upstream cylinders in the VIV lock-in regime is elongated and split into two by the downstream cylinder. The elongation of the vortices delays the vortex shedding and detunes the vortex shedding frequency to the natural frequency. In the galloping regime, the vortices generated from different vortex shedding periods behave differently, because the position of the cylinders at different vortex shedding periods is different. In the galloping regime and while the cylinders moving downwards or upwards, a number of different vortex shedding periods are involved, resulting in a slightly tilted vortex street, as shown in Figures 8(c) and (e).

**4.2. Effect of center-to-center distance on galloping for  $\alpha = 2.5^\circ$ .** It has been found that the center-to-center distance ( $L$ ) has a significant effect on the VIV response of four circular cylinders in an inline square arrangement [30]. This section mainly focuses on the effect of  $L$  on the dynamic response. Simulations were performed by varying  $L$  from 1.5 to 4 with an increment of 0.5 for a angle of attack with  $\alpha = 2.5^\circ$  and a reduced velocity of  $V_r = 40$ . The center-to-center distance  $L$  is found to have significant effects on the vibration of the square cylinders. Figure 9 shows the time histories and FFT spectra of the  $Y$ -displacement and the lift fluctuation for different values of  $L$ , where the results for the  $Y$ -displacement are shown in red solid lines and those for lift fluctuation are shown in blue dashed lines.

Figures 10 and 11 show the vorticity contours for  $L = 1.5$  and 2, respectively. The position of the cylinder is marked on the  $XY$ -trajectory in each diagram of Figures 10 and 11. Based on the time histories and the vortex shedding patterns, it can be seen that the vibrations are typical of the galloping responses for  $L = 1.5$  and 2. At  $L = 1.5$ , six vortices (labeled by A–E in Figure 10) are shed from the cylinders in one cycle of vibration. The jet flowing from the gap between the top and bottom rows of the cylinders is very weak and merges into the shear layers from two sides of the cylinder system. The vortex street in the wake of the four square cylinders is very similar to that behind a single structure. As  $L = 2$ , the vibration is a typical galloping response, characterized by a number of vortex shedding periods in one cycle of vibration as shown in Figure 9(b). Because the shear layers generated from the horizontal gap form vortices that are shed from the cylinders, the number of the vortices that are shed from the cylinders in one cycle of vibration for  $L = 2$  is greater than that for  $L = 1.5$ . The combination of the vortices from the bottom row cylinders with those from the top row cylinders occurs continuously. Each of the vortices A–I in Figure 11 is the combined vortex. For example, the vortices A1 and A2 in Figure 11(a) combine to form a single vortex A, as shown in Figure 11(b). The galloping at  $L = 1.5$  and 2 results in high amplitude vibrations, as shown in Figure 9. Due to

the effects of the jet flow from the horizontal gap between the cylinders, the vibration amplitude at  $L = 2$  is lower than that at  $L = 1.5$ .

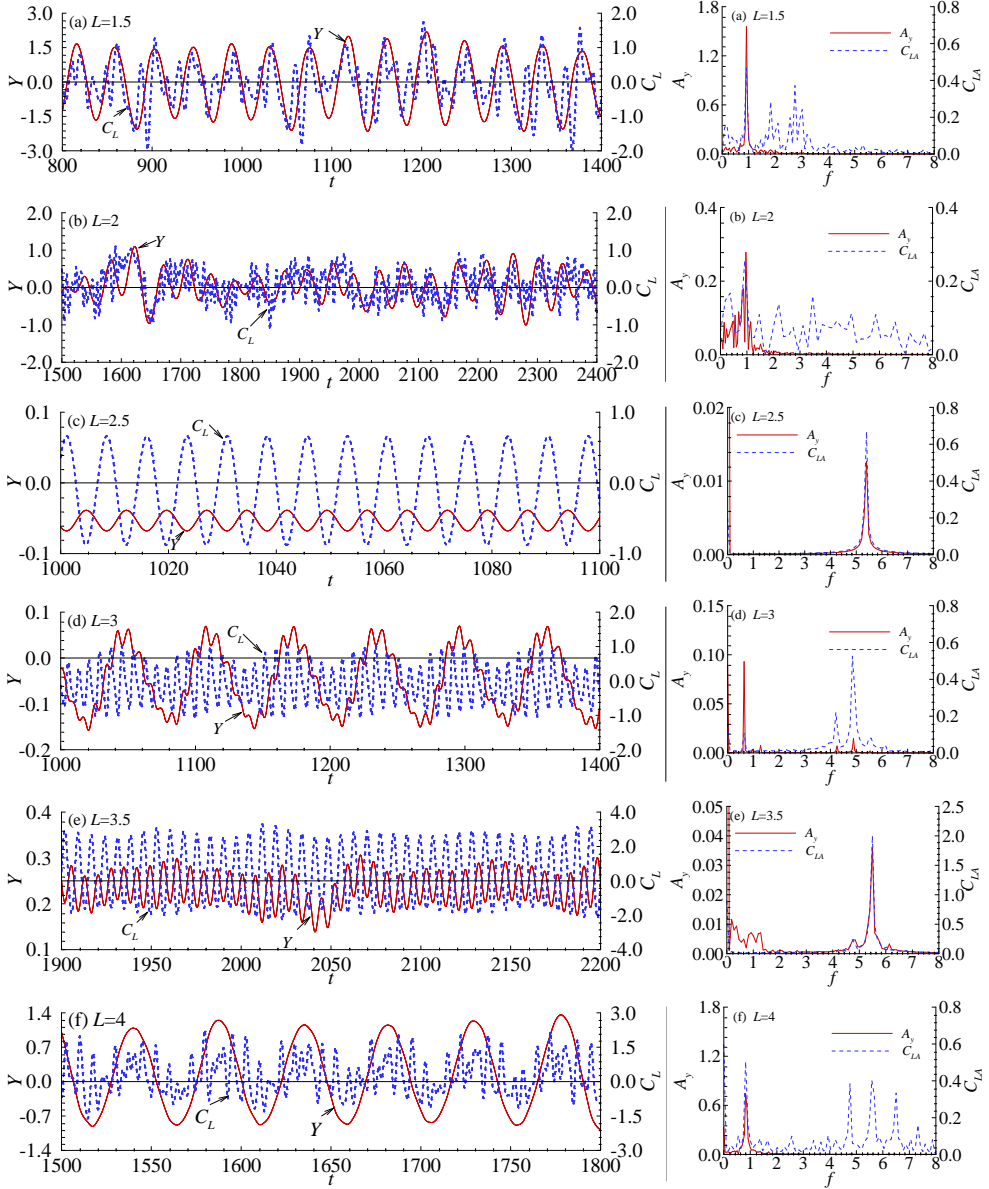


Figure 9. Time histories (left column) and FFT spectra (right column) of the cross-flow displacement and the lift force coefficient for different center-to-center distances  $L$  at fixed  $\alpha = 2.5^\circ$  and  $V_r = 40$ . Solid line,  $Y$ -displacement; Dashed line, lift coefficient

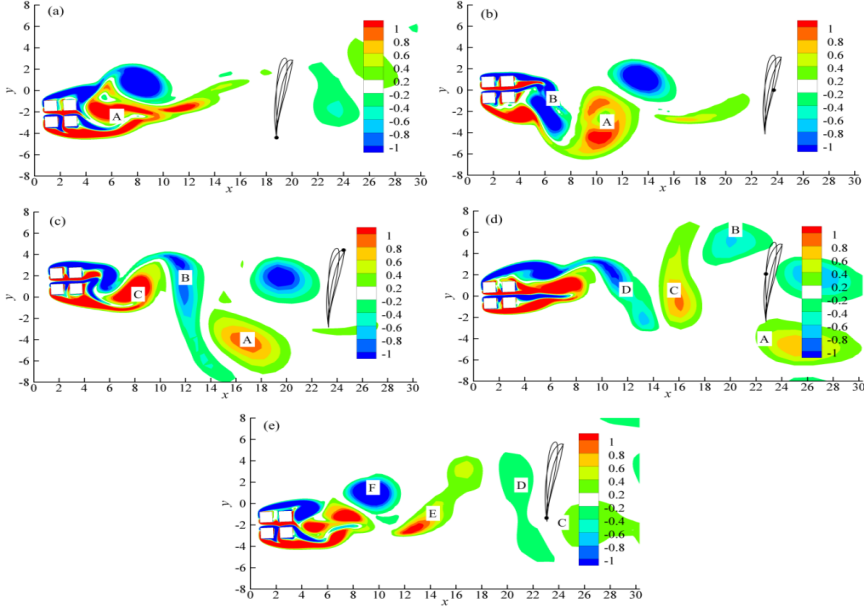


Figure 10. Vorticity contours for  $\alpha = 2.5^\circ$ ,  $V_r = 40$  and  $L = 1.5$ . The position of the cylinder is marked on the  $XY$ -trajectory in each diagram

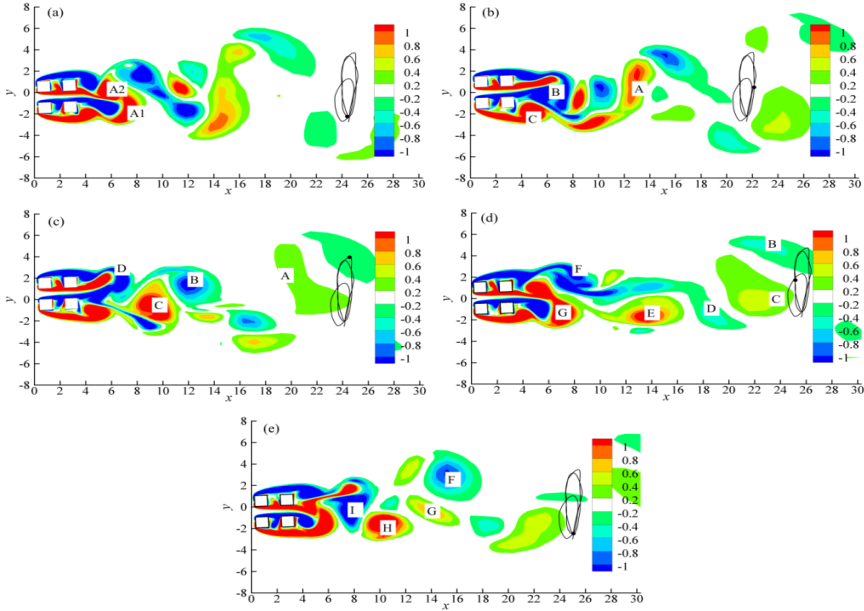


Figure 11. Vorticity contours for  $\alpha = 2.5^\circ$ ,  $V_r = 40$  and  $L = 2$ . The position of the cylinder is marked on the  $XY$ -trajectory in each diagram.

Figure 12 shows the vorticity contours for  $L = 2.5$ . The difference between the flows for  $L = 2$  and 2.5 is that at  $L = 2.5$ , a complete vortex shedding process occurs from each of the downstream cylinders. The combination of the vortices also occurs, which is similar to that for  $L = 2$ . The combination only occurs after the vortices are totally separated from the cylinders. The vibration amplitude is very small and no galloping is observed for  $L = 2.5$ , because the vortex shedding occurs from the two upstream cylinders. Each horizontal row of cylinders behaves as a single body that conforms better than a single cylinder. The vortex shedding processes from the two downstream cylinders synchronize perfectly at  $L = 2.5$ , resulting in the very periodic vibration shown in Figure 9(c).

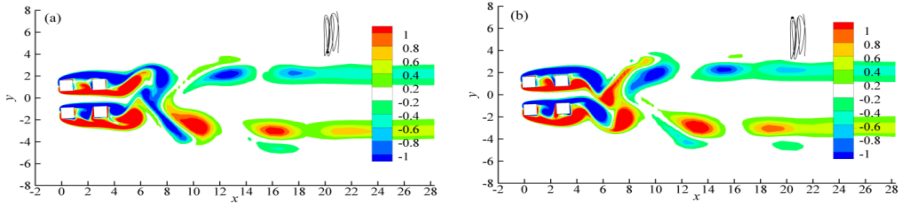


Figure 12. Vorticity contours for  $\alpha = 2.5^\circ$ ,  $V_r = 40$  and  $L = 2.5$ . The position of the cylinder is marked on the  $XY$ -trajectory in each diagram.

Figures 13 and 14 show the vorticity contours for  $L = 3$  and 3.5, respectively. When  $L$  increases to 3, the vortices generated from the horizontal gap of the cylinders are strong. This stops the combinations of the vortices. In Figure 13, the vortices A1 and A2 are shed from the gap almost at the same time and coexist as they are convected downstream. There are a number of vortex shedding periods in one cycle of vibration. When two cylinders are placed in a flow in a tandem arrangement, vortex shedding only occurs from the downstream cylinder, as the two cylinders are very close to each other, leading to a single body vortex shedding flow mode. When the gap between the two cylinders is large enough, vortex shedding occurs from both cylinders and the flow is in a co-shedding mode (Zdravkovich [34]; Zhou and Yiu [35]). It is interesting to see that at  $L = 3.5$ , the vortex shedding from the top row cylinders is in an elongated single body mode, while that from the bottom row cylinders is in a co-shedding mode. When four circular cylinders are in an inline square arrangement ( $\alpha = 0^\circ$ ), the combination of single body and co-shedding modes does not occur (Zhao et al. [30]). This is a distinct feature for flow past four cylinders at a small angle of attack. Although the vortices shed from the cylinders are in different modes, the vortex shedding period of the four cylinders synchronizes. This is evidenced by the FFT spectrum shown in Figure 9(e), where the total lift coefficient only has one predominant frequency component. The lift coefficient would have had multiple frequencies if the vortices shedding from the top row cylinders were different from those from the bottom row cylinders. As  $L$  is increased to 4, vortex shedding occurs from all four square cylinders, and the vibration is in a high amplitude galloping mode. The flow patterns for  $L = 4$  and  $V_r = 40$  are not presented since they are similar to that for  $V_r = 35$  shown in Figure 8.



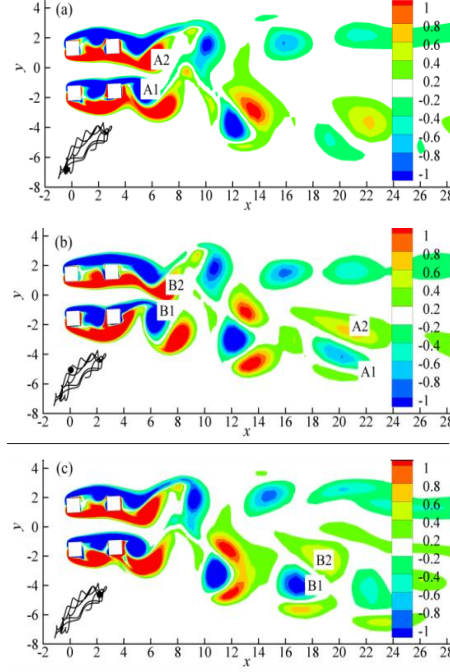


Figure 13. Vorticity contours for  $\alpha = 2.5^\circ$ ,  $V_r = 40$  and  $L = 3$ . The position of the cylinder is marked on the  $XY$ -trajectory in each diagram.

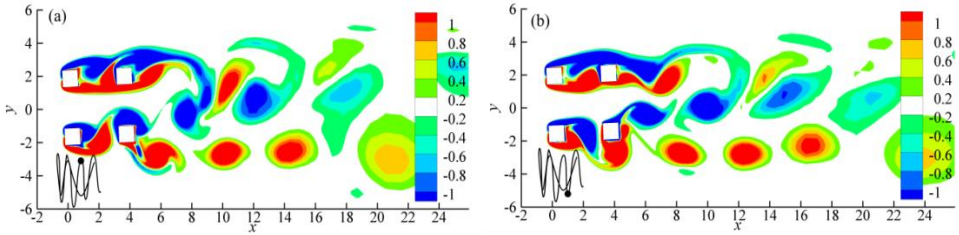


Figure 14. Vorticity contours for  $\alpha = 2.5^\circ$ ,  $V_r = 40$  and  $L = 3.5$ . The position of the cylinder is marked on the  $XY$ -trajectory in each diagram.

The above numerical results suggest that the distance  $L$  has a significant effect on the vibration amplitude and the response frequency through changing the flow mode. If  $L$  is either sufficiently large enough ( $L = 4$ ) or sufficiently small ( $L = 1.5$  and  $2$ ), galloping occurs and the vibration amplitude is large. The vibration for very large  $L$  comprises galloping responses of four cylinders while the vibration for very small  $L$  resembles the response of a single cylinder. The vibration amplitude is reduced significantly for  $2.5 \leq L \leq 3.5$  because of the influence from the horizontal gaps of the cylinders.

## 5. CONCLUSIONS

Numerical simulations were conducted to study the flow-induced vibrations of four rigidly-connected cylinders in a square arrangement in two-dimensional steady flow of a constant property Newtonian fluid with low Reynolds number. The conclusions are summarized as follows:

- (1) The effect of angle of attack ( $\alpha$ )

VIV response is observed for all the simulated angles of attack with  $L = 4$ . The galloping occurs when the angle of attack is smaller than  $\alpha = 5^\circ$ . VIV and galloping responses can be separated from each other because the galloping happens at critical reduced velocities, which are greater than the upper boundary of the VIV lock-in regime. When the angle of attack is large enough (for example,  $\alpha = 12.5^\circ$  and  $15^\circ$ ), only VIV responses are observed. As for  $\alpha = 7.5^\circ$  and  $10^\circ$ , the modulation between the vortex shedding frequency and a very low frequency was observed. With the increase of reduced velocity, the low frequency component become more significant, and the dynamic response amplitude increases and finally evolves into galloping.

- (2) The effect of center-to-center distance ( $L$ )

The effects of the center-to-center distance on the dynamic response were examined by simulating the dynamic response at typical  $V_r = 40$  and  $\alpha = 2.5^\circ$ . Galloping occurs when  $L$  is either large or small. When  $L$  is an intermediate value (from 2.5 to 3.5), galloping is not observed because the vortex shedding flow is strongly affected by the jet flow from the gap of the cylinders. At  $L = 3.5$  a combination of the single body vortex shedding mode from the top row cylinders and the co-shedding mode from the bottom row cylinders is observed. This combined vortex shedding mode is believed to be a distinct feature for small angles of attack.

## 6. NOMENCLATURE

$\alpha$	angle of attack,
$L$	non-dimensional center-to-center distance between two adjacent square cylinders,
$B$	side length of the square cylinder,
$f_n$	structural natural frequency,
$U$	free-stream velocity,
$V_r$	reduced velocity, $U/f_n B$ ,
$\nu$	kinematic viscosity coefficient,
$Re$	Reynolds number, $UB/\nu$ ,
$m$	total mass of the square cylinders,
$m_s$	displaced mass of the fluid,
$m^*$	mass ratio, $m/m_s$ ,
$c$	structural damping coefficient,
$k$	structural spring stiffness,
$\zeta$	structural damping ratio, $c/(4km)^{1/2}$ ,
$u, v$	non-dimensional variables of velocity,

$t$	time,
$p$	pressure,
$\rho$	fluid density,
$x_i$	Cartesian coordinate with $x_1 = x$ and $x_2 = y$ ,
$u_i$	velocity component in the $x_i$ direction,
$u_j$ mesh	velocity of the moving computational mesh,
$X_i$	non-dimensional displacement,
$F_n$	dimensionless structural natural frequency, $f_n B/U$ ,
$F_i$	total hydrodynamic force in the $x_i$ -direction,
$C_i$	total hydrodynamic coefficient on the square cylinders in the $x_i$ -direction, $2F_i/(\rho B U^2)$ ,
$C_D$	drag coefficient,
$C_L$	lift coefficient,
$S_i$	displacement of the mesh modal point in the $x_i$ -direction,
$A$	area of the computational mesh,
$\gamma$	introduced to control mesh deformation, $1/A$ ,
$X_{rms}, Y_{rms}$	root mean square displacement,
$C_{D,mean}$	mean total drag coefficient,
$C_{D,rms}, C_{L,rms}$	root mean square total drag and lift coefficients,
$A_x$	vibration amplitudes in the $x$ -direction, $(X_{\max} - X_{\min})/2$ ,
$A_y$	vibration amplitudes in the $y$ -direction, $(Y_{\max} - Y_{\min})/2$ ,
$X_{\max}, X_{\min}, Y_{\max}, Y_{\min}$	maximum and minimum displacements,
$X$	displacements of the cylinder in $x$ -direction,
$Y$	displacements of the cylinder in $y$ -direction,
$f_m$	modulation frequency,
$f_s$	vortex shedding frequency,
$f_g$	frequency of the galloping response,
$f^*$	dimensional frequency,
$f$	non-dimensional frequency, $f = f^* B/U$ .

**Acknowledgement.** The authors would like to acknowledge supports from the National Key R&D Program of China (Project ID: 2017YFC1404202) and the National Natural Science Foundation of China (Grant No. 51979031, 51779040 and 51490673).

## REFERENCES

1. P. W. Bearman. "Vortex shedding from oscillating bluff bodies." *Annual Review of Fluid Mechanics*, **16**, (1984), pp. 195–222. DOI: 10.1146/annurev.fl.16.010184.001211.
2. T. Sarpkaya. "A critical review of the intrinsic nature of vortex-induced vibration." *Journal of Fluids and Structures*, **19**(4), (2004), pp. 389–447. DOI: 10.1016/j.jfluidstructs.2004.02.005.
3. C. H. K. Williamson and R. Govardhan. "Vortex-induced vibrations." *Annual Review of Fluid Mechanics*, **36**, (2004), pp. 413–455. DOI: 10.1146/annurev.fluid.36.050802.122128.

4. R. D. Gabbai and H. Benaroya. "An overview of modeling and experiments of vortex-induced vibration of circular cylinders." *Journal of Sound and Vibration*, **282**(3-5), (2005), pp. 575–616. DOI: 10.1016/j.jsv.2004.04.017.
5. C. H. K. Williamson and R. Govardhan. "A brief review of recent results in vortex-induced vibrations." *Journal of Wind Engineering and Industrial Aerodynamics*, **96**(6-7), (2008), pp. 713–735. DOI: 10.1016/j.jweia.2007.06.019.
6. S. C. Luo, X. H. Tong, and B. C. Khoo. "Transition phenomena in the wake of a square cylinder." *Journal of Fluids and Structures*, **23**(2), (2007), pp. 227–248. DOI: 10.1016/j.jfluidstructs.2006.08.012.
7. G. J. Sheard, M. J. Fitzgerald, and K. Ryan. "Cylinders with square cross-section: wake instabilities with incident angle variation." *Journal of Fluid Mechanics*, **630**(2), (2007), pp. 43–69. DOI: 10.1017/S0022112009006879.
8. D. H. Yoon, K. S. Kang, and C. B. Choi. "Flow past a square cylinder with an angle of incidence." *Physics of Fluids*, **22**(4), 043603, (2010). DOI: 10.1063/1.3388857.
9. G. V. Parkinson and N. P. H. Brooks. "On the aeroelastic instability of bluff cylinders." *Journal of Applied Mechanics-Transactions of the ASME*, **28**(2), (1961), pp. 252–258. DOI: 10.1115/1.3641663.
10. G. V. Parkinson and J. D. Smith. "The square prism as an aeroelastic non-linear oscillator." *Quarterly Journal of Mechanics and Applied Mathematics*, **17**(2), (1964), 225–239. DOI: 10.1093/qjmam/17.2.125.
11. P. W. Bearman, I. S. Gartshore, D. J. Maull, and G. V. Parkinson. "Experiments on flow-induced vibration of a square-section cylinder." *Journal of Fluids and Structures*, **1**(1), (1987), pp. 19–34. DOI: 10.1016/S0889-9746(87)90158-7.
12. A. R. Bokaian and F. Geoola. "Hydroelastic instabilities of square cylinders." *Journal of Sound and Vibration*, **92**(1), (1984), pp. 117–141. DOI: 10.1016/0022-460X(84)90378-X.
13. Z. J. Wang and Y. Zhou. "Vortex-induced vibration characteristics of an elastic square cylinder on fixed supports." *Journal of Fluids Engineering*, **127**(2), (2004), pp. 241–249. DOI: 10.1115/1.1881693.
14. A. Nemes, J. S. Zhao, D. L. Jacono, and J. Sheridan. "The interaction between flow-induced vibration mechanisms of a square cylinder with varying angles of attack." *Journal of Fluids Engineering*, **710**(11), (2004), pp. 102–130. DOI: 10.1017/jfm.2012.353.
15. J. S. Zhao, J. S. Leontini, D. L. Jacono, and J. Sheridan. "Fluid-structure interaction of a square cylinder at different angles of attack." *Journal of Fluid Mechanics*, **747** (2014), pp. 688–721. DOI: 10.1017/jfm.2014.167.
16. S. Sen and S. Mittal. "Free vibration of a square cylinder at low Reynolds numbers." *Journal of Fluids and Structures*, **27**(5-6), (2011), pp. 875–884. DOI: 10.1016/j.jfluidstructs.2011.03.006.
17. C. H. K. Williamson and A. Roshko. "Vortex formation in the wake of an oscillating cylinder." *Journal of Fluids and Structures*, **2**(4), (1988), pp. 355–381. DOI: 10.1016/S0889-9746(88)90058-8.

18. S. Sen and S. Mittal. "Vortex formation in the wake of an oscillating cylinder." *Journal of Fluids and Structures*, **54**(4), (2015), pp. 661–678. DOI: 10.1016/j.jfluidstructs.2015.01.006.
19. A. Joly, S. Etienne, and D. Pelletier. "Galloping of square cylinders in cross-flow at low Reynolds numbers." *Journal of Fluids and Structures*, **28**(1), (2012), pp. 232–243. DOI: 10.1016/j.jfluidstructs.2011.12.004.
20. M. Zhao, L. Cheng, and T. M. Tong. "Numerical simulation of vortex-induced vibration of a square cylinder at a low Reynolds number." *Physics of Fluids*, **25**(2), 023603 (2013). DOI: 10.1063/1.4792351.
21. M. Zhao. "Flow-induced vibrations of square and rectangular cylinders at low Reynolds number." *Fluid Dynamics Research*, **47**(2), (2015). DOI: 10.1088/0169-5983/47/2/025502.
22. Z. D. Cui, M. Zhao, B. Teng, and L. Cheng. "Two-dimensional numerical study of vortex-induced vibration and galloping of square and rectangular cylinders in steady flow." *Ocean Engineering*, **106**(9) (2015), pp. 189–206. DOI: 10.1016/j.oceaneng.2015.07.004.
23. M. Y. Liu, L. F. Xiao, and L. J. Yang. "Experimental investigation of flow characteristics around four square-cylinder arrays at subcritical Reynolds numbers." *International Journal of Naval Architecture and Ocean Engineering*, **7**(5) (2015), pp. 906–919. DOI: 10.1515/ijnaoe-2015-0063.
24. M. Zhao, L. Cheng, B. Teng, and G. H. Dong. "Hydrodynamic forces on dual cylinders of different diameters in steady currents." *Journal of Fluids and Structures*, **23**(1) (2007), pp. 59–83. DOI: 10.1016/j.jfluidstructs.2006.07.003.
25. M. Zhao and L. Cheng. "Numerical simulation of two-degree-of-freedom vortex-induced vibration of a circular cylinder close to a plane boundary." *Journal of Fluids and Structures*, **27**(7) (2011), pp. 1097–1110. DOI: 10.1016/j.jfluidstructs.2011.07.001.
26. M. Zhao, L. Cheng, and L. Lu. "Vortex induced vibrations of a rotating circular cylinder at low Reynolds number." *Physics of Fluids*, **26**, 073602, (2014). DOI: 10.1063/1.4886196.
27. M. Liu, L. Lu, B. Teng, M. Zhao, and G. Q. Tang. "Numerical modeling of local scour and forces for submarine pipeline under surface waves." *Coastal Engineering*, **116**(10) (2016), pp. 275–288. DOI: 10.1016/j.coastaleng.2016.05.003.
28. M. Zhao, Z. D. Cui, K. Kwok, and Y. Zhang. "Wake-induced vibration of a small cylinder in the wake of a large cylinder." *Ocean Engineering*, **113**(1) (2016), pp. 75–89. DOI: 10.1016/j.oceaneng.2015.12.032.
29. M. Zhao and L. Cheng. "Numerical simulation of vortex-induced vibration of four circular cylinders in a square configuration." *Journal of Fluids and Structures*, **31**(5) (2012), pp. 125–140. DOI: 10.1016/j.jfluidstructs.2012.04.002.
30. M. Zhao, K. Kaja, Y. Xiang, and L. Cheng. "Vortex-induced vibration of four cylinders in an in-line square configuration." *Physics of Fluids*, **28**(2), 023602 (2012). DOI: 10.1063/1.4941774.
31. K. Lam, W. Q. Gong, and R. M. C. So. "Numerical simulation of cross-flow around four cylinders in an in-line square configuration." *Journal of Fluids and*

- Structures*, **24**(1) (2008), pp. 34–57. DOI: 10.1016/j.jfluidstructs.2007.06.003.
32. S. P. Singh and S. Mittal. “Vortex-induced oscillations at low Reynolds numbers: Hysteresis and vortex shedding modes.” *Journal of Fluids and Structures*, **20**(8) (2005), pp. 1085–1104. DOI: 10.1016/j.jfluidstructs.2005.05.011.
33. M. Zhao, K. Kaja, Y. Xiang, and L. Cheng. “Flow induced vibration of two rigidly coupled circular cylinders in tandem and side-by-side arrangements at a low Reynolds number of 150.” *Physics of Fluids*, **25**(12), 123601 (2013). DOI: 10.1063/1.4832956.
34. M. M. Zdravkovich. “The effects of interference between circular cylinders in cross flow.” *Journal of Fluids and Structures*, **1**(2) (1987), pp. 239–261. DOI: 10.1016/S0889-9746(87)90355-0.
35. Y. Zhou and M. W. Yiu. “Flow structure, momentum and heat transport in a two-tandem-cylinder wake.” *Journal of Fluid Mechanics*, **548**(2) (1987), pp. 17–48. DOI: 10.1017/S002211200500738X.

## Notes for Contributors

### to the Journal of Computational and Applied Mechanics

**Aims and scope.** The aim of the journal is to publish research papers on theoretical and applied mechanics. Special emphasis is given to articles on computational mechanics, continuum mechanics (mechanics of solid bodies, fluid mechanics, heat and mass transfer) and dynamics. Review papers on a research field and materials effective for teaching can also be accepted and are published as review papers or classroom notes. Papers devoted to mathematical problems relevant to mechanics will also be considered.

**Frequency of the journal.** Two issues a year (approximately 80 pages per issue).

**Submission of Manuscripts.** Submission of a manuscript implies that the paper has not been published, nor is being considered for publication elsewhere. Papers should be written in standard grammatical English. The manuscript is to be submitted in electronic, preferably in pdf, format. The text is to be 130 mm wide and 190 mm long and the main text should be typeset in 10pt CMR fonts. Though the length of a paper is not prescribed, authors are encouraged to write concisely. However, short communications or discussions on papers published in the journal must not be longer than 2 pages. Each manuscript should be provided with an English Abstract of about 50–70 words, reporting concisely on the objective and results of the paper. The Abstract is followed by the Mathematical Subject Classification – in case the author (or authors) give the classification codes – then the keywords (no more than five). References should be grouped at the end of the paper in numerical order of appearance. Author's name(s) and initials, paper titles, journal name, volume, issue, year and page numbers should be given for all journals referenced.

The journal prefers the submission of manuscripts in L<sup>A</sup>T<sub>E</sub>X. Authors should select the  $\mathcal{A}\mathcal{M}\mathcal{S}$ -L<sup>A</sup>T<sub>E</sub>X article class and are not recommended to define their own L<sup>A</sup>T<sub>E</sub>X commands. Visit our home page for further details concerning how to edit your paper.

For the purpose of refereeing the manuscripts should be sent either to Balázs Tóth (Balazs.TOTH@uni-miskolc.hu) or György SZEIDL (Gyorgy.SZEIDL@uni-miskolc.hu).

The eventual supply of an accepted for publication paper in its final camera-ready form will ensure more rapid publication. Format requirements are provided by the home page of the journal from which sample L<sup>A</sup>T<sub>E</sub>X files can be downloaded:

<http://www.mech.uni-miskolc.hu/jcam>

These sample files can also be obtained directly (via e-mail) from Balázs TÓTH (Balazs.TOTH@uni-miskolc.hu), upon request.

One issue of the journal and ten offprints will be provided free of charge and mailed to the correspondent author. Since JCAM is an open access journal each paper can be downloaded freely from the homepage of the journal.

The Journal of Computational and Applied Mechanics is abstracted in Zentralblatt für Mathematik and in the Russian Referativnij Zhurnal.

Secretariat of the Vice-Rector for Research and International Relations, University of Miskolc  
Responsible for publication: Prof. Dr. Tamás Kékesi  
Published by the Miskolc University Press under the leadership of Attila Szendi  
Responsible for duplication: Works manager Erzsébet Pásztor  
Number of copies printed: 75  
Put to the Press on December 12, 2019  
Number of permission: TNRT.2020-20.ME.

**HU ISSN 1586–2070**



## **A Short History of the Publications of the University of Miskolc**

The University of Miskolc (Hungary) is an important center of research in Central Europe. Its parent university was founded by the Empress Maria Teresia in Selmezbánya (today Banská Štiavnica, Slovakia) in 1735. After the first World War the legal predecessor of the University of Miskolc moved to Sopron (Hungary) where, in 1929, it started the series of university publications with the title *Publications of the Mining and Metallurgical Division of the Hungarian Academy of Mining and Forestry Engineering* (Volumes I.-VI.). From 1934 to 1947 the Institution had the name Faculty of Mining, Metallurgical and Forestry Engineering of the József Nádor University of Technology and Economic Sciences at Sopron. Accordingly, the publications were given the title *Publications of the Mining and Metallurgical Engineering Division* (Volumes VII.-XVI.). For the last volume before 1950 – due to a further change in the name of the Institution – *Technical University, Faculties of Mining, Metallurgical and Forestry Engineering, Publications of the Mining and Metallurgical Divisions* was the title.

For some years after 1950 the Publications were temporarily suspended.

After the foundation of the Mechanical Engineering Faculty in Miskolc in 1949 and the movement of the Sopron Mining and Metallurgical Faculties to Miskolc, the Publications restarted with the general title *Publications of the Technical University of Heavy Industry* in 1955. Four new series - Series A (Mining), Series B (Metallurgy), Series C (Machinery) and Series D (Natural Sciences) - were founded in 1976. These came out both in foreign languages (English, German and Russian) and in Hungarian.

In 1990, right after the foundation of some new faculties, the university was renamed to University of Miskolc. At the same time the structure of the Publications was reorganized so that it could follow the faculty structure. Accordingly three new series were established: Series E (Legal Sciences), Series F (Economic Sciences) and Series G (Humanities and Social Sciences). The latest series, i.e., the series H (European Integration Studies) was founded in 2001. The eight series are formed by some periodicals and such publications which come out with various frequencies.

Papers on computational and applied mechanics were published in the

### **Publications of the University of Miskolc, Series D, Natural Sciences.**

This series was given the name Natural Sciences, Mathematics in 1995. The name change reflects the fact that most of the papers published in the journal are of mathematical nature though papers on mechanics also come out.

The series

### **Publications of the University of Miskolc, Series C, Fundamental Engineering Sciences**

founded in 1995 also published papers on mechanical issues. The present journal, which is published with the support of the Faculty of Mechanical Engineering and Informatics as a member of the Series C (Machinery), is the legal successor of the above journal.



# **Journal of Computational and Applied Mechanics**

Volume 14, Number 1-2 (2019)

---

## **Contents**

### **Contributed Papers**

- O. ADELEYE, O. ABDULKAREEM, A. YINUSA and G. SOBAMOWO:  
Analytical investigations of temperature effects on creep strain relaxation of biomaterials using homotopy perturbation and differential transform methods 5–23
- István ECSEDI and Attila BAKSA: A theory for the longitudinal vibrations of anisotropic elastic bars based on the Rayleigh-Bishop model 25–39
- Dávid GÖNCZI: Analysis of a curved bimetallic beam 41–51
- Guoqiang TANG, Mingyin DUAN, Lin LU and Ming ZHAO: Fluid-structure interaction of four rigidly-connected square cylinders in steady flow 53–76